POLITECNICO DI TORINO

Corso di Laurea Magistrale

In Ingegneria Meccanica

Tesi di Laurea magistrale

Innovative design of a Twin Disc tribometer for wheel-rail contact analysis.

Relatore

Prof. Nicolò Zampieri

Candidato

Rosario Pagano

Anno Accademico

2023/2024

Abstract

The tribological properties of steels used to realize railway wheels play a fundamental role in the performances of both vehicle and infrastructure. In particular, the wear process, caused by the wheel-rail interaction, modifies the shape of wheel and rail profiles, changing the performances of the vehicle. For this reason, research institutes and vehicle manufacturers have worked hard to develop predictive tools able to estimate the evolution of the wheel and rail profiles. The efficiency of these tools is strongly influenced by the tribological properties of the materials, i.e. the wear coefficients, which are used as input data. The characterization of these properties requires specific tools and long-lasting experimental campaigns, that are usually performed under controlled operating conditions, using twin disc test benches. These devices usually do not consider the real contact conditions in terms of normal load, contact geometry, and slip velocity, since they are equipped with small size rollers. The paper proposes an innovative 1:5 scaled twin disc, which allows to reproduce the real wheel-rail contact conditions, thanks to the Pascal's scaling technique. The testing device allows to reproduce a wide range of typical operating conditions of railway vehicles, thanks to high power independent brushless motors, used to actuate the rollers, and an innovative loading system.

Table of contents

List of figures:

List of tables:

1.Introduction

Investigating and managing the wear in wheel-rail interactions is crucial for enhancing safety, reliability, and efficiency in railway systems while also reducing maintenance costs. The ramifications of wear on wheels can have catastrophic consequences on the dynamics and stability of a wagon: material being removed from the wheel causes vibrations and stresses which, in turn, will worsen the working conditions of other mechanical components such as suspensions and brakes. Depending on the speed and load applied, the profiles of wheel and rail will be modified, compromising safety, and increasing the likelihood of derailment.

Predicting how wear behaves during wheel-rail contact allows to estimate how much material is removed due to wear, thus facilitating maintenance operations. For this reason, research institutes and vehicle manufacturers have worked hard to develop predictive tools able to estimate the evolution of the wheel and rail profiles. The efficiency of these tools is strongly influenced by the tribological properties of materials, namely wear coefficients, which are used as input data. To obtain said wear coefficients long-lasting experimental campaigns and specific test benches are required. These experiments may be conducted in the field [1-4] or through simulated experiments. These can be carried out on different scales, ranging from full-scale laboratory experiments [4-7] to small-scale tests. As most test rigs differ in the material of the contacting bodies, size and strategy adopted to produce wear, comparison of results across these studies is often very difficult.

Field tests, on one hand represent the operating conditions the closes as they involve actual wheel and rails, on the other hand are also complex, time-consuming and have low repeatability. Likewise, tests conducted using full-scale rigs are onerous and expensive, and they are not suitable for small laboratory facilities. Consequently, to study the tribology of materials in the railway industry, tribometers are often preferred due to their practicality and enhanced control over the test parameters, such as load, materials and sliding speeds.

The most common tribometers used to test standard materials in the railway industry are “pin-on-disc” [8-11], “ball on disc” [12-14], and “twin disc” tribometers. In pin-on-disc tribometers, the pin is stationary and is pressed against a rotating disc, hence sliding speed is easily obtained. Similarly, in ball on disc tribometers, a small rotating sphere is pressed against the rotating disc made of the material the properties of which are under study. While ball on disc tribometers incorporate a rolling motion, unlike pin-on-disc which only replicate a sliding motion, both tribometers can only provide fragmentary insights into the complex contact of a wheel-rail system.

Twin disc tribometers consist in two discs, referred to as rollers, which are pressed against each other. By rotating each disc, it’s possible to achieve both a rolling and sliding contact; for this reason, they lend themselves well to test a multitude of parameters of steels commonly used in wheel and rail systems. However, in the literature, twin disc setups commonly share a limitation: the contact geometry between the discs is oversimplified and not representative of actual contact conditions. In many cases, the discs utilized are essentially two cylinders, which

deviates significantly from the actual wheel-rail contact geometry. Even in instances where the wheel-simulating disc mirrors an actual wheel's profile, the rail-representing disc still has a cylindrical shape [15]. This discrepancy presents a challenge in accurately replicating the interactions involved in real wheel-rail systems.

The development of reliable test benches is of paramount importance to get further insights into the adhesion and wear phenomena, thus leading the path towards an improvement of the wheel-rail interaction [16-19]. This thesis introduces a novel design concept for a twin disc tribometer constructed using readily available components refurbished from pre-existing test benches. The main novelty of the newly designed twin disc is that both the rail and wheel discs are machined to the actual scaled profile shapes. The twin disc relies on Pascal's similitude model, which ensures a unitary scaling factor for the contact pressure but does not ensure the similarity of the contact patch area, because of the nonlinearities in the hertzian contact. Therefore, a major novelty of the designed twin disc is that the rail profile curvature is slightly modified to keep a coherent scaling of the contact area, and normal load. As an upgrade of common twin disc benches, the adoption of a scaling technique allows to obtain results that can be directly related to typical operating conditions of different types of railway vehicles, thus overcoming the main limitation of twin discs, that are used in most cases as basic tribometers.

Chapter 2 in this document describes how wear can be quantified and in particular how it influences and is studied in the contact of wheel-railway systems, illustrating the most common wear models.

Chapter 3 describes the state-of-the-art test benches used in the field of railway systems, focusing on twin disc tribometers and the scaling strategies used.

In chapter 4 the design of the novel twin disc will be described, as well as the type of tests that it can perform.

Chapter 5 includes the description of a multibody model of the test bench, implemented in the Simpack commercial multibody code, and the results of preliminary wear simulations.

Chapter 6 contains future developments regarding the designed twin disc machine.

Finally, the conclusion section summarizes the main outcomes of the activity described in the thesis, highlighting the benefits of the new design.

2.The study of wear in railway systems

Depending on the speed and load applied, the profiles of wheel and rail will be modified, compromising safety, and increasing the likelihood of derailment. Being able to predict said wear is of crucial importance: precise knowledge regarding the timing of maintenance interventions on both rail and wheel, allows for enhanced safety standards, passenger comfort, and cost reduction.

Consequently, for the development of railway systems it's crucial to understand and apply the insights that can be gained from the field of tribology, the scientific study dedicated to quantifying and comprehending phenomena such as friction, lubrication, and wear of surfaces in relative motion. Unlike systems like ball bearings, characterized by lubricated environments devoid of contaminants, the wheel-rail system is exposed to external particles such as dirt, leaves and rain, and the fluctuations in humidity and temperature further influence the contact dynamics, the forces transmitted, and consequent material removed due to wear.

Wear is a multifaceted phenomenon, influenced by an array of parameters, including the materials in contact, environmental conditions, contact pressure, contact geometry, and sliding velocity [20]. In the context of the railway industry, wear ensues when two surfaces under load engage in relative motion, in this case this type of motion is referred to as motion with slippage. Between wheel and rail there can be simultaneously different wear mechanisms at the same time. Some of the most frequent wear mechanisms are as follows:

- Wear due to adhesion occurs when adhesion or a high local plastic deformation causes the material to transfer from a surface to another. This type of wear is typical for similar materials in contact, such as in the case of wheel and rail steels. In case there is the removal of a large quantity of material, it is referred to as seizure and it is a catastrophic failure of the contact.
- Abrasive wear arises when one material in contact is very hard, and the other is softer. In the case of railway industry, it occurs when contaminants are crushed into small fragments embedded in the softer material which will then in turn scratch the harder material, wearing it out.
- Corrosive wear transpires when there's removal of layers of oxides from the contact surfaces due to chemical and electrochemical reaction. Hard oxide particles, trapped in the contact will increase wear in both materials.
- Delamination wear consists in the detachment of layers of fine material.
- Finally, the so-called rolling contact fatigue (RCF) occurs in cases where stress concentrates near material defects, especially near the surface, and exceeds the yield stress of materials, causing failure of the system. Fig. 2.1 shows the tread of a wheel that suffered rolling contact fatigue.

A more in-depth analysis of these different forms of wear can be found in Olofsson et al. review [21].

Figure 2.1: Wheel tread with RCF damage highlighted. Taken from: "Enhancing rail infra durability through freight bogie design" [22].

A less complex classification is the distinction of mild and severe wear, two types of wear that can also be described in Archard's law of wear [23], which will be described in greater detail below. The mild wear is characterized by a polished surface after wear. It occurs for either low or very high levels of creep and moderate contact pressure. Severe wear, which happens for intermediate levels of creep, is recognizable by the rough surface of the worn material, as if it was subjected to pitting. In the rail-wheel contact, the primary wear mechanisms are adhesion and delamination.

Wear occurs due to the sliding between the surfaces of wheel and rail, and, depending on its value, the wear may be classified either as mild or severe. It should also be noted that the transition between an acceptable level of wear and a catastrophic one depends on the materials' hardness and surface. Namely, it is commonly assumed that in case the contact pressure reaches approximately 80% of the material's hardness, there's a transition into the so-called seizure wear, characterized by failure of the contact. Temperature also plays a role in which wear mechanism is dominant, as it can reduce the yield strength and other material properties, as experimentally established by Lewis et al. [24].

2.1 Wear models

In the literature of wheel-rail interaction, mathematical models used to predict the behaviour of the material removed due to wear can be classified in two main categories:

- Sliding models: in these models the material removed due to wear is proportional to the distance travelled in sliding motion.
- Energetic models: the material removed depends on the energy dissipated in the contact area.

The most common wear laws adopted are those of Archard [25], Kraus and Poll [26], Zobory [27], British Rail Research (BRR) centre [28], and Sheffield University (USFD) [29].

2.1.1 Sliding model: Archard's law

One of the most widely used approaches to estimate wear in the railway field is the Archard's wear law [25]. It calculates the amount of worn volume $V_{removed}$ as:

$$V_{removed} = k_{Arch} \cdot \frac{N \cdot d_s}{H_s} \tag{2.1}$$

where is the N normal load, d_s is the sliding distance, H_s the Brinell hardness of the softer contacting material and finally k_{Arch} is the wear coefficient. The latter is commonly evaluated as a function of contact pressure and sliding speed, from experimental maps that usually feature four wear zones, see Fig. 2.2.

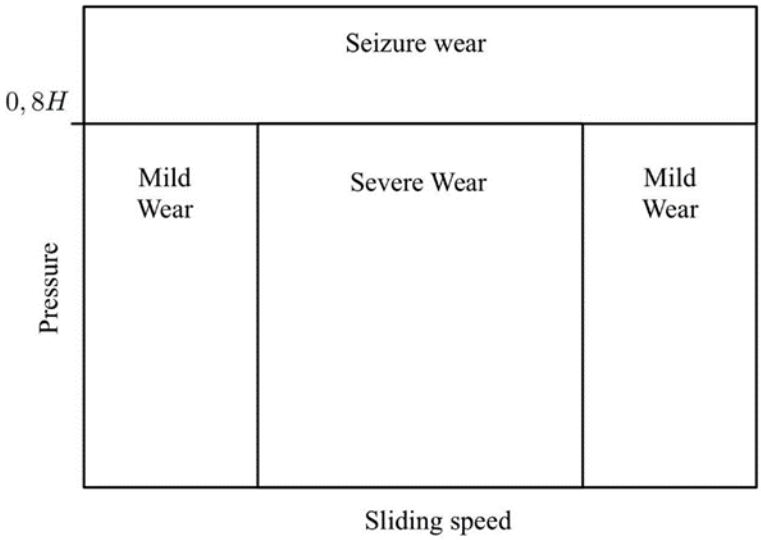

Figure 2.2: Archard Wear Map.

One of the most widely used maps is the one obtained from work carried out at the Swedish Royal Institute of Technology (KTH) [30]. Typically, constants coefficients are taken for each zone, and their values as well as the boundaries of each zone are obtained from literature data obtained in a range of different conditions. This law is also implemented in various multibody software, such as SIMPACK. Enblom et al. [31] have obtained a wear map with different materials at dry conditions, they can be seen in Table 2.1, where K_1 is the coefficient for seizure wear, K_2 and K_4 are the coefficients for mild wear and K_3 is the one for severe wear. In railway operations the main regimes are the ones in the regions characterised by the coefficient K_2 and K_3.

Wear coefficient K	$v_{slip} < 0.2$ m/s	0.2 m/s $< v_{slip} <$ 0.7 m/s	$v_{slip} > 0.7$ m/s
$P > 0.8 * H$ MPa	$K_1 = 300 - 400 \times 10^{-4}$ m/km		
$P < 0.8 * H$ MPa	$K_2 = 1 - 10 \times 10^{-4}$ m/km	$K_3 = 30 - 40 \times 10^{-4}$ m/km	$K_4 = 1 - 10 \times 10^{-4}$ m/km

Table 2.1: Values of the wear coefficient according to Enblom et al [31].

Starting from these values, Bosso and Zampieri obtained values of k_{Arch} for different values of sliding speed using a scaled roller-rig [32], seen in Table 2.2.

Wear coefficient K	v_{slip}						
	<0.1	0.1 ÷ 0.2	0.2 ÷ 0.3	0.3 ÷ 0.4	0.4 ÷ 0.5	0.5 ÷ 0.7	>0.7
Wheel							
$P > 0.8 * H$ MPa				370×10^{-4}			
$P < 0.8 * H$ MPa	1×10^{-4}	3.6×10^{-4}	8.5×10^{-4}	29×10^{-4}	31.8×10^{-4}	18×10^{-4}	1×10^{-4}
Roller							
$P > 0.8 * H$ MPa				520×10^{-4}			
$P < 0.8 * H$ MPa	2×10^{-4}	7.8×10^{-4}	13.3×10^{-4}	48.2×10^{-4}	53×10^{-4}	21.7×10^{-4}	2×10^{-4}

Table 2.2: Values of the wear coefficient used in Bosso and Zampieri [31] work. The coefficients are expressed in m/km rolled.

Archard's law can also be applied locally in the worn-out area to calculate the wear depth Δz_n normal to the contact patch, as stated in the following equation:

$$\Delta z_n(x,y) = k_{Arch} \frac{p_z(x,y)}{H_s} \cdot \frac{v_s(x,y)\Delta x}{v_0} \tag{2.2}$$

Where v_s is the sliding speed, v_0 is the rolling speed and Δx is the contact patch discretization step in longitudinal direction.

2.1.2 Energetic modelling: Krause and Poll

Also available in the wear module of the SIMPACK commercial code is the energetic wear law proposed by Krause and Poll [26]. It correlates the volume of removed material to the energy dissipated due to friction, as the following expressions state:

$$V_{removed} = \begin{cases} C_m W_{friction} & \frac{P_{friction}}{A} \leq 4\ W/mm^2 \\ C_s W_{friction} & \frac{P_{friction}}{A} > 4\ W/mm^2 \end{cases} \tag{2.3}$$

$$W_{friction} = P_{friction} \Delta t, \qquad P_{friction} = v_0 T \gamma \tag{2.4}$$

Where $W_{friction}$ is the dissipated energy, $P_{friction}$ is the dissipated power per contact area, Δt is the integration time step and C_m and C_s are the wear coefficients for the mild and severe wear zones respectively.

2.1.3 Energetic modelling: Zobory

Zobory suggested another energetic wear law to calculate locally the flow rate of removed material in each element of the contact patch. It states that the flow rate of mass per unit of contact area of worn material is proportional to a specific dissipated power, as the following expressions state:

$$\dot{m}_d(x,y) = k_{zob}(w_{sp}) \cdot \dot{w}_{sp}(x,y) \tag{2.5}$$

$$\dot{w}_{sp}(x,y) = v_0 \frac{T\gamma}{A} \cdot \frac{p_z(x,y)}{p_{z,avg}} \tag{2.6}$$

Where:

- $\dot{m}_d$ is the flow rate of removed material per unit of contact area,
- $\dot{w}_{sp}$ is the specific dissipated power,
- k_{zob} is the wear coefficient suggested by Zobory,
- $p_{z,avg}$ is the average normal contact pressure
- $T\gamma$ is a wear number, related to the amount of specific dissipated energy at the contact interface per unit of contact length, that can be obtained using Equation (2.7).

$$T\gamma = |F_x\xi| + |F_y\eta| + |M_z\varphi| \tag{2.7}$$

Where F_x and ξ are the longitudinal force and its creepage coefficient, F_y and η are the lateral force and φ its creepage coefficient and M_z and are the spin moment and its creepage coefficient.

This model considers only the mild and severe wear zones and the transition between them depends on the value of specific dissipated power. As the coefficient depends on the contact patch, the model is used for a local application, thus requiring the identification of the distribution of sliding speed and tangential pressure.

2.1.4 Other models and conclusions

Another useful work for gaining insights into wear transitions are present in work by Lewis et al. [33]. According to this work, stemming from a collaboration of the Sheffield University (USFD), Swedish Royal Institute of Technology (KTH), technical university of Lisbon and the ALSTOM Ferroviaria company, the transition from mild to severe regime is related to the development of full slip conditions on the contact patch. Furthermore, the transition from severe to seizure mode is linked to a drop in mechanical properties, such as yield stress, of materials due to high temperatures.

Due to the intrinsic complex nature of wear mechanisms, accurately modelling the physical phenomena underlying the wear process to calculate removed material is practically impossible. Consequently, the prevailing approach in the literature involves devising wear laws calibrated using data gleaned from experimental test

campaigns. It is clear then that to obtain said wear coefficients, the test campaigns must be able to replicate as best as possible the contact geometry, kinematics and dynamics. A diagram showing the prevailing approach is shown in Fig. 2.3.

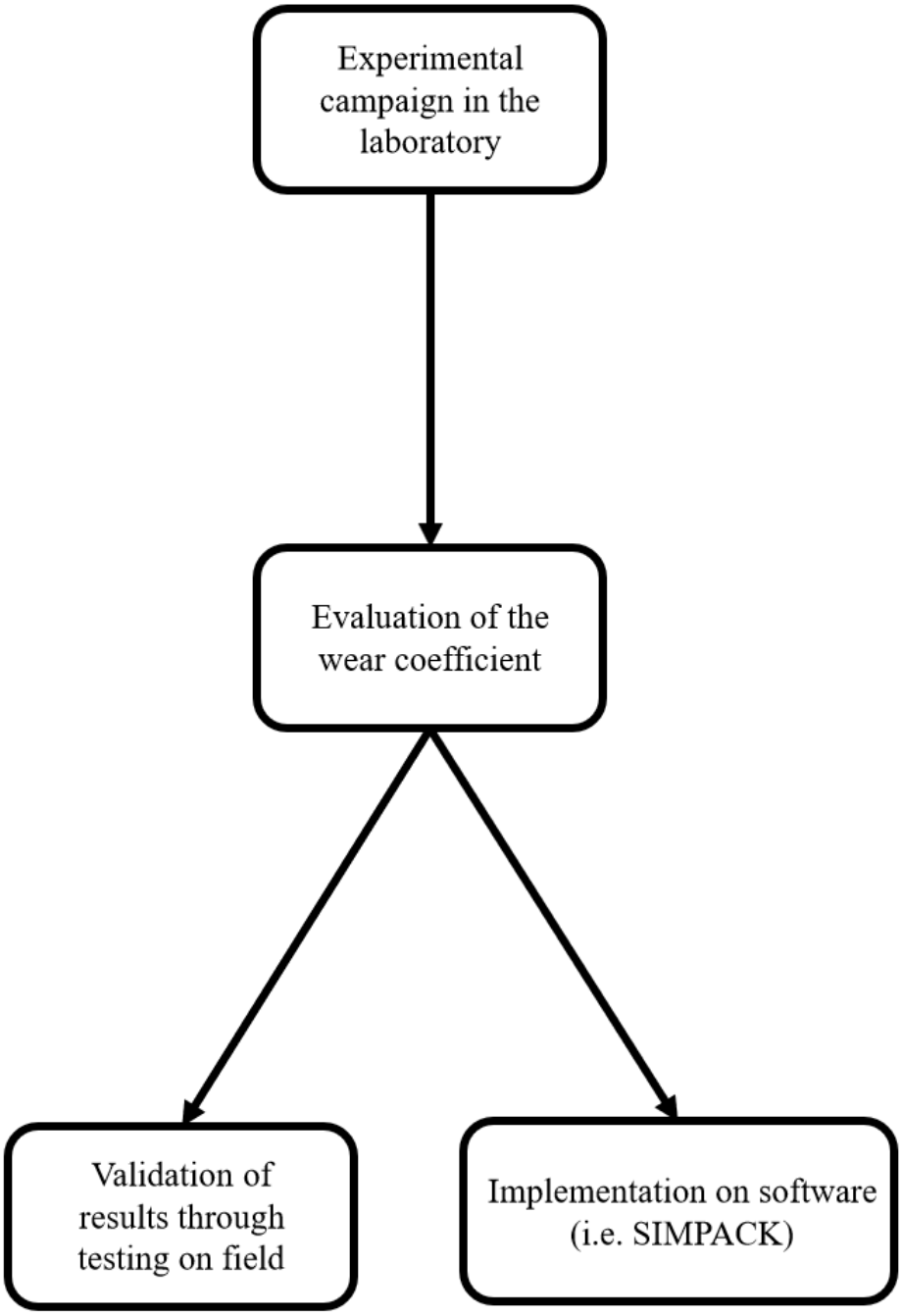

Figure 2.3: Diagram of the common sequence of events for wear tests.

3.State of the art of Twin Disc tribometers in railway systems

3.1 Field test and full-scale benches

As stated in the previous chapter, it's possible to build models in order to predict the tribological behaviour of wheels and rails. These models often require wear coefficients, which need to be obtained through rigorous experimental test campaigns.

These tests can be carried out directly on field, by studying the profiles and worn material of real wheels and rails. However, these tests turn out to be often expensive as they are intrinsically time consuming and may need for a railway to shut down in order for them to take place. Additionally, the limited time due to operational requirements, may also cause the researchers to be unable to gather enough data to conduct statistical analysis [4]. Furthermore, as it is the case for other research areas, there is little control over the environment, thus it's practically impossible to completely negate the effects of contaminants and climate. For these reasons the data that can be obtained through field tests is rather aleatory and the tests have low repeatability. Instead, field data and tests should be carefully planned in conjunction with scaled tests in order to validate models, as it is suggested by Zhu et al. [34]. This manuscript also offers a useful summary of the state of the art of research regarding the influence of environmental conditions on wheel-rail wear. To study rails in particular, it's also possible to gather a section of a rail that has been used on operational lines and subject it to full scale tests, as is the case of the work done by Olofosson et al. [2].

Full scale benches, evidently allow to simulate the phenomena with greater fidelity and accuracy, however they are expensive and are not suitable for small laboratory facilities. An example of full-scale benches are roller-rigs test benches, in which a wheel is in contact with a roller which, unlike a rail, has a finite value of curvature in the longitudinal direction. By reproducing the dynamics of railway vehicles, these benches lend themselves well to investigate a multitude of phenomena, according to Allen et al. [35] these include wheel-rail contact, adhesion, traction and braking operations, wear and rolling contact fatigue (RCF), derailment, curving, noise and vibrations, testing of component performance and finally investigation of component performances. An example of a full-scale roller-rig is the one used by Zhang et al. in their investigation of adhesion phenomena [36] and is featured in Fig. 3.1.

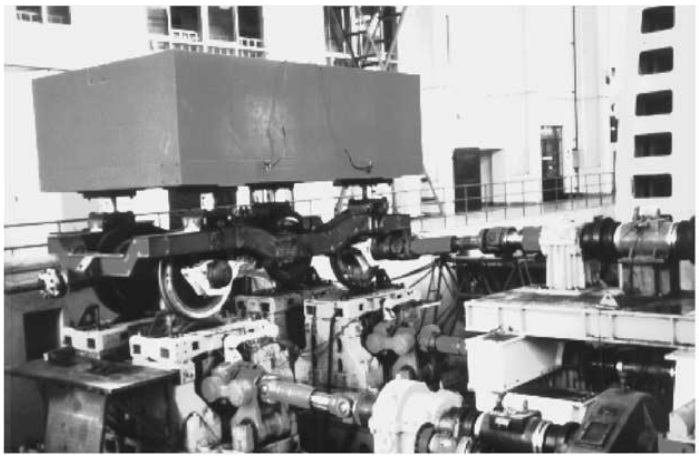

Figure 3.1: Full-scale roller-rig used by Zhang et al. Taken from "Wheel/rail adhesion and analysis by using full-scale roller rig" [36].

As it can be observed in the figure above, a full-scale roller-rig featuring multiple wheels is rather cumbersome and, evidently, depending on the phenomena that need to be investigated, the design makes the test bench intrinsically complex and expensive. In contrast, traditional tribometers offer a more straightforward and cost-effective means of gathering valuable insights into the tribological behaviour of wheels. Additionally, their smaller size allows for installation in a greater number of laboratories, further enhancing accessibility and versatility.

3.2 Traditional tribometers

As stated earlier, smaller test benches are more cost-effective, they allow for greater repeatability, control over the conditions and environment, and are overall reliable.

The most basic laboratory apparatus utilized for measuring the wheel-rail friction coefficient is the pin-on-disc system. This setup involves pressing a pin specimen against a rotating disc [37]. While the pin-on-disc device effectively replicates sliding friction conditions, it has limitations. Notably, it does not capture the actual geometry of the contacting bodies and overlooks factors such as vehicle dynamic behaviour.

Despite these limitations, the pin-on-disc device serves as a dependable tool for swiftly evaluating the impact of various contaminants on the friction coefficient, as demonstrated by Abassi [38] and Cann [39], or various lubricants as seen in the work by Sundh et al. [9]. The compact size of the tribometer also allows for it to be placed inside a controlled chamber, in which temperature and humidity can be easily monitored and controlled. The pin-on-disc machine used by Abassi in their study [38] can be seen in Fig. 3.2.a.

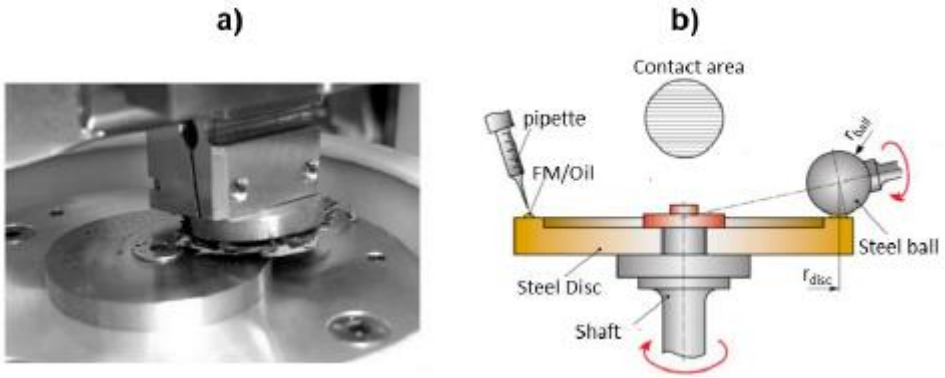

Figure 3.2: (a) Pin on disc tribometer [38] and (b) example of mini-traction-machine. Taken from "Development of numerical and experimental tools for the simulation of train braking operations" [40].

An advancement from the pin-on-disc system is the mini-traction-machine (MTM) or ball-on-disc tribometer, where the pin is substituted with a ball capable of rotation around a fixed axis, see Fig. 3.2.b. With separate motors driving the ball and the disc, controlled slip can be achieved at the contact patch. The MTM facilitates the replication of rolling-sliding motion of steel materials under various friction conditions by appropriately contaminating the contact interface. As seen on pin-on-disc, also these test benches lend themselves well to test the effects of contaminants, such as leaves [39], and lubrification [41].

Both scaled systems described above, utilized for studying adhesion at the wheel-rail interface, exhibit a common limitation: they overlook the real dynamic behaviour of the vehicle, thereby failing to replicate the interaction among geometry, kinematics, and vehicle dynamics, especially after wear.

By scaling a roller-rig, it is possible to replicate the contact dynamics of wheel-rail interaction, while still gaining the benefits linked to a smaller test bench. It can be installed in smaller laboratories; it is generally cheaper as the components are less bulky, and the actuation would not need to handle large masses. However they require for a scaling strategy to be defined, which often depends on the type of tests the rig is supposed to carry out.

3.2.1 Scaling strategies and scaled roller-rig test benches

Both full-scale and scaled roller-rigs exhibit differences to the operational scenario of real systems, primarily stemming from differences in geometry between the rail and the roller. Namely, the roller features a non-zero curvature in the longitudinal direction, as opposed to a rail. Furthermore, a constraint prohibits the translation of wheels mounted on roller-rigs. Additionally, in scaled roller-rigs, size scaling translates to the scaling of all other parameters to ensure compatibility between the scaled system and the full-scale counterpart.

This means that to effectively correlate data from scaled test rigs to full-scale wheel-rail contact, a similitude model is essential. Ensuring similitude between the scaled model and the actual system requires meeting three criteria: geometrical, kinematic, and dynamic similitude. This practice draws primarily from the contributions of Iwnicki, Jaschinski, and Pascal. A comprehensive mathematical exposition on the derivation of scaling factors specific to railway dynamics, including the main ones which will be discussed, is provided in the review by Bosso et al. [42].

The definition of the scaling strategy begins with the choice of the length scaling factor φ_l, which is essentially the ratio between a length in the full-scale system and the corresponding length of the scaled one, as it is expressed in the following equation:

$$\varphi_l = \frac{l_1}{l_0} \tag{3.1}$$

Where the subscripts 1 and 0 represent the full-scale system and the scaled one respectively. With this definition, the scaling factors for cross-section (area) φ_A and volume φ_V, can be defined as follows:

$$\varphi_A = \varphi_l^2 \tag{3.2}$$

$$\varphi_V = \varphi_l^3 \tag{3.3}$$

Similarly, a time scaling factor can be obtained as:

$$\varphi_t = \frac{t_1}{t_0} \tag{3.4}$$

Therefore, the scaling factors for velocity and acceleration are:

$$\varphi_v = \frac{\varphi_l}{\varphi_t} \tag{3.5}$$

$$\varphi_a = \frac{\varphi_l}{\varphi_t^2} \tag{3.6}$$

Finally, by defining the density scaling factor φ_ρ, it is possible to determine also scaling factors for mass φ_m, moment of inertia φ_I and φ_F for inertial force:

$$\varphi_\rho = \frac{\rho_1}{\rho_0} \tag{3.7}$$

$$\varphi_m = \varphi_\rho \varphi_l^3 \tag{3.8}$$

$$\varphi_I = \varphi_m \tag{3.9}$$

$$\varphi_F = \frac{m_1 a_1}{m_0 a_0} = \varphi_m \varphi_a = \frac{\varphi_\rho \varphi_l^4}{\varphi_t^2} \tag{3.10}$$

Depending on the value of these, different scaling strategies can be defined. It's apparent that, defined certain factors, others will be obtained through the physical and mathematical equations that describe the phenomena.

A first scaling strategy is the one proposed by Iwnicki [43]. It is based on setting the scaling factor for time φ_t equal to 1, this way the scaled and full-scale system will feature the same natural frequencies, as the velocity and acceleration scaling factors will be equal to the length scaling factor, as expressed in equations (3.5) and

(3.6). Furthermore, as the materials used frequently are the same, also φ_ρ is unitary, therefore the scaling factor for forces and mass will be:

$$\varphi_F = \varphi_l^4 \tag{3.11}$$

$$\varphi_m = \varphi_l^3 \tag{3.12}$$

These equations clash with each other as inertial forces would not be able to scale according to (3.11) as the mass scales of a factor determined by (3.12). For this reason, in scaled roller-rigs designed using Iwnicki scaling strategy, a system of supporting wires and ropes is usually required to lift the wheel roller, in order to simulate gravity. The work by Liang et al. [43], uses a scaled roller rig installed at University of Huddersfield and shown in Fig. 3.3.

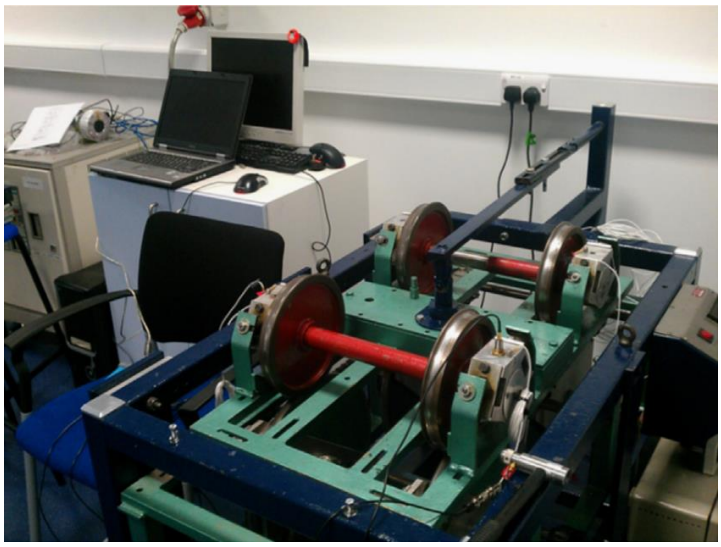

Figure 3.3: scaled roller-rig used in Liang et al.'s work. Taken from "Adaptive noise cancelling and time-frequency techniques for rail surface defect detection" [43].

In order to apply the adaptive noise cancelling (ANC) technique on railway wheel flat and rail surface defect detection, the rig has been scaled using Iwnicki scaling strategy, as it is crucial for the rig to have the same natural frequencies.

A second scaling strategy is derived from the work conducted by Jaschinski in order to develop the scaled roller-rig at the DLR laboratories in Germany, as shown in Fig. 3.4. This bench focuses extensively on investigating non-linear lateral dynamics, known as hunting. For this reason, the scaling of the roller rig requires to maintain the similarity of the equations describing the motion of a wheel. Therefore, acceleration and velocity need to be scaled as follows:

$$\varphi_a = 1 \tag{3.13}$$

$$\varphi_v = \sqrt{\varphi_l} \tag{3.14}$$

However, maintaining similitude for wheel-rail forces necessities scaling density by a factor:

$$\varphi_\rho = \frac{1}{\varphi_l} \tag{3.15}$$

which is challenging to realize with a length scaling factor φ_l equal to 5. Consequently, Jaschinski proposed setting an arbitrary value for the density scaling factor, thereby accepting a lack of similitude for creep forces in the linear portion of the adhesion curve. Therefore, a compromise of a scaling factor for density of:

$$\varphi_\rho = \frac{1}{2} \tag{3.16}$$

Has been reached, instead of the theoretically 1/5, which has proven to provide good experimental results.

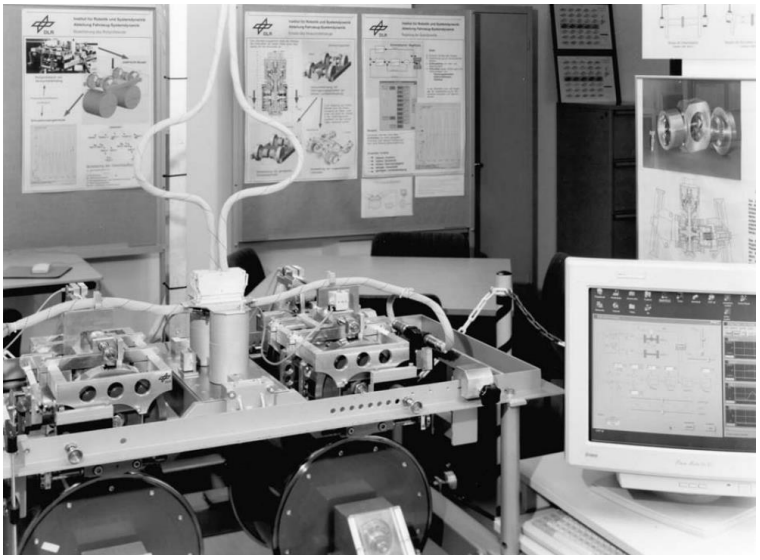

Figure 3.4: The 1/5-scale DLR roller rig developed by Jachinski et al. [44]. Taken from: "The application of roller rigs to railway vehicle dynamics" by Jaschinski, A., Chollet, H., Iwnicki, S., Wickens, A. & Von Würzen, J.

Despite this issue, in Jaschinski's approach inertial forces are scaled like the other forces, unlike Iwnicki's.

Lastly, the scaling strategy developed by Pascal and applied in the French INRETS scaled roller-rig (Institut National de Recherche sur les Transports et leur Securite) will be described. Its main goal is to simulate contact phenomena by imposing a unitary scaling factor for stresses:

$$\varphi_\sigma = \frac{\varphi_F}{\varphi_l^2} = 1 \tag{3.17}$$

Consequently, the contact pressure will also scale accordingly, causing it to have the same value on both the scaled and full-scale systems. From this value, and considering that the scaling for density will be unitary as well, since the materials used are frequently the same, the scaling factor for forces will be:

$$\varphi_F = \varphi_l^2 \tag{3.18}$$

Furthermore, defining the scaling factor for elastic stiffness as:

$$\varphi_c = \frac{\varphi_F}{\varphi_l} = \varphi_l \tag{3.19}$$

A scaling factor for frequency can be defined as well, recalling equation (3.8):

$$\varphi_\omega = \sqrt{\frac{\varphi_c}{\varphi_m}} = \sqrt{\frac{\varphi_l}{\varphi_\rho \varphi_l^3}} = \frac{1}{\varphi_l} \tag{3.20}$$

Thus, gravity on the scaled system is scaled by a factor:

$$\varphi_g = \frac{1}{\varphi_l} \tag{3.21}$$

Which means that it must be artificially introduced in the system, to guarantee that a consistent value of the normal contact force. Namely, the roller-rig will require additional external normal loads in order to ensure a similitude of stresses and contact pressure.

As stated before, depending on the main phenomena that the scaled roller-rig aims to simulate, a different scaling strategy should be adopted. An ingenious solution to carry out different experimental campaigns using the same scaled roller-rig is the one developed by the railway research group of Politecnico di Torino [45-48]. The schematic of the roller rig is shown in Fig. 3.5.

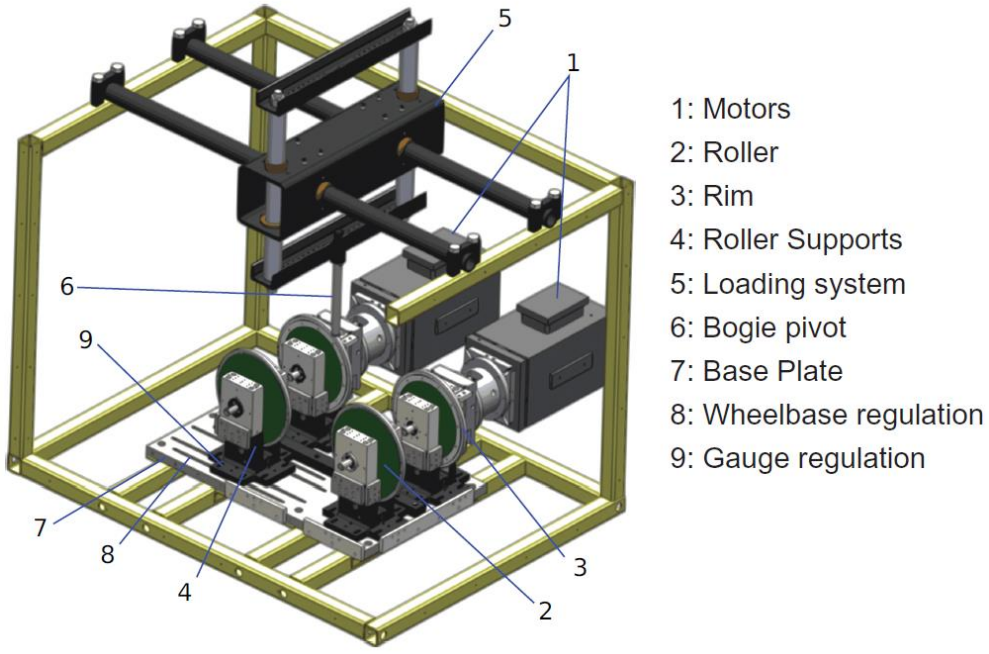

Figure 3.5: Schematic of test rig at Politecnico di Torino. Taken from "Scale testing theory and approaches" [12].

The external rims of the rollers can be changed, depending on the material, profile shape or simply when the profiles are worn out and need to be replaced. This grants flexibility to the scaled roller-rig and allows to investigate multiple aspects of the

vehicle, such as contact forces, adhesion, wear, and traction control. Another scaled roller-rig installed at Politecnico di Torino, featured in Fig. 3.6, is the multi-wheelset test bench [49], an evolution of the single wheelset roller-rig. Two rollers, simulating rails, are each set in motion by a motor and support four wheelsets.

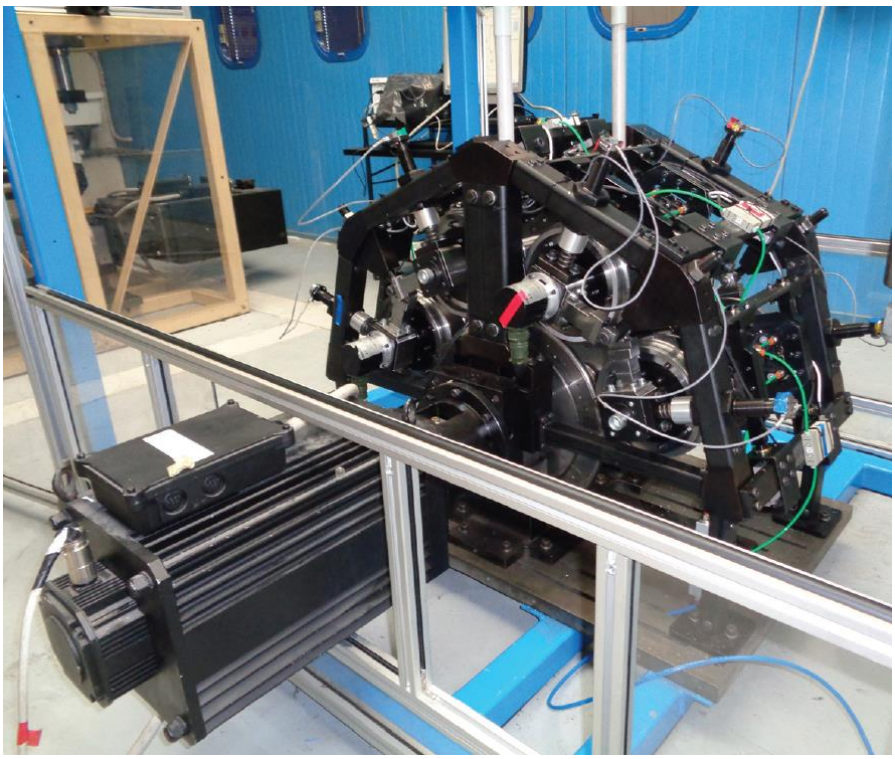

Figure 3.6: Multi-wheelset test bench at Politecnico di Torino. Taken from "Scale testing theory and approaches" [12].

Each of the main similitude models described in this chapter has their own advantages and disadvantages. Iwnicki's scaling strategy allows the scaled and full scaled roller-rigs to be characterized by the same natural frequency. It achieves this by having a scaling factor for time equal to 1 (Equation 3.4). This, however, causes the necessity to artificially modify the gravity on the scaled model, thus it is crucial to take that into account when designing the scaled test bench.

In Jachinski's scaling strategy, by defining a unitary scaling factor for acceleration (Equation 3.13), inertial forces are scaled as the other forces without requiring solving issues linked to the scaling of gravity, present in the other two methods. However, density scales proportionally to the inverse of the length scaling factor, issue that has to be taken into account both in the design phase and in the testing procedure.

Finally, the most suitable scaling strategy for analysing contact phenomena is Pascal's similitude model. It is based on defining a unitary scaling factor for stresses, thus pressure as well. As is the case of Iwnicki's scaling strategy, the scaling of gravity must be considered, specifically, the scaled roller-rig has to include a system to virtually increase the normal load in order to reach the same pressure of the full-scale model.

The following table (Table 3.1), taken from the doctoral dissertation "Development of numerical and experimental tools for the simulation of train braking operations" by Magelli M. [40], is a useful tool to show the values of the scaling factors of the main quantities of interest, depending on the scaling method. Set the scaling factor for length equal to 5, the most common scaling factor for length in the literature, the other scaling factors are as follows:

Quantity	Iwnicki	Pascal	Jashinski (ρ=1)	Jashinski (ρ=1/5)
Length	5	5	5	5
Time	1	5	$\sqrt{5}$	$\sqrt{5}$
Speed	5	1	$\sqrt{5}$	$\sqrt{5}$
Acceleration	5	1/5	1	1
Mass	125	125	125	25
Force	625	25	125	25
Density	1	1	1	1/5
Weight	125	125	125	25
Young's modulus	1	1	1	1
Stiffness	125	5	25	5
Torsional stiffness	3125	125	625	125
Creep force	625	25	125	25
Damping	125	25	$25\sqrt{5}$	$5\sqrt{5}$
Torsional damping	3125	625	$625\sqrt{5}$	$125\sqrt{5}$
Inertia	3125	3125	3125	625

Table 3.1: scaling factors for different similitude models, taken from "Development of numerical and experimental tools for the simulation of train braking operations" [40].

3.3 Twin disc tribometers

Twin disc tribometers can be considered a better tool than pin-on-disc or ball on disc machines to study the effects of wear in the wheel-rail contact as they offer a more realistic simulation of the rolling-sliding motions. It consists of two rotating discs in contact, while an external radial force presses on them increasing the effects of wear. The main parameters that can be set during testing are the rotational velocities of each disc, thus the slippage between them, and the contact pressure that depends on the external force applied.

Figure 3.7: Two discs of a twin-disc tribometer in contact. Taken from "Towards a Standard Approach for the Twin Disc Testing of Top-Of Rail Friction Management Products" [50].

In literature, various configurations of twin disc test rigs have been designed and developed, reflecting diverse approaches to experimentation. The review by Rocha et al. [51] collects and synthesizes the knowledge developed on the different design strategies and experimental campaigns performed using twin disc tribometers in the railway industry.

The prevailing setup of a twin disc machine features two independent motors, enabling the discs to reach different speeds. This configuration affords great methodological flexibility, as the speed of each motor can be controlled independently, thus it allows to reach the desired creep.

Alternatively, some devices utilize a single motor, with the sliding relationship between the discs achieved through a gear system. However, a limitation of this approach is that the range of sliding variation is constrained by the transmission

ratios between the gears. Another method to induce sliding between discs involves installing discs of different sizes, although this approach has become less common due to its inability to facilitate creep control throughout the test duration.

Regarding load application, pneumatic or hydraulic systems are commonly utilized, with pneumatic actuators offering advantages such as the capability to apply higher and more uniform loads throughout the test. Alternatively, simpler, and more cost-effective systems have been identified in the literature, including equipment employing a spring compression mechanism in one of the machine axes to facilitate load application.

Fig. 3.8 provides a schematic representation of the various creep control and load application systems employed in twin disc machines as documented in the literature.

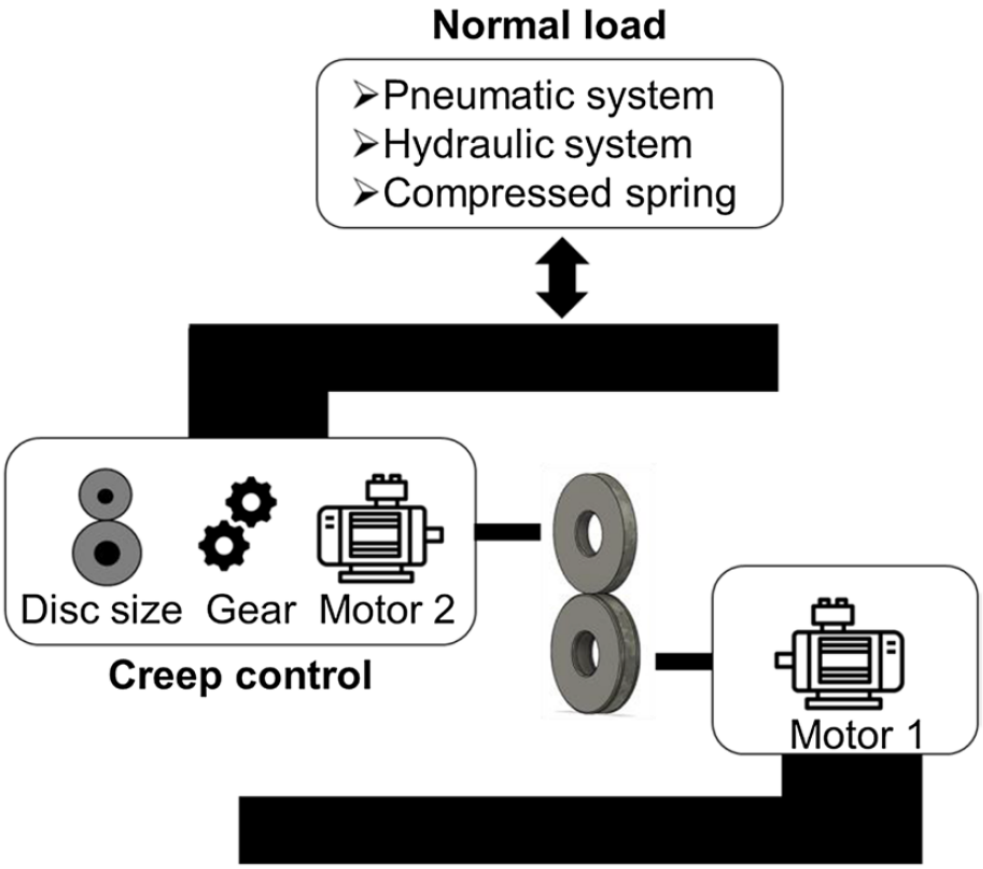

Figure 3.8: schematic representing the different designs of twin-disc tribometers found in the literature. Taken from "Using twin disc for applications in the railway: a systematic review" [51].

In the field of railway engineering, the twin disc test is extensively utilized due to its ability to easily relate test parameters to the operational conditions of railways, as it can simulate both sliding and rolling kinematics. This facilitates the simulation of various factors affecting railway performance, such as axle load, wheel-rail contact pressure, and slippage. By controlling the rotation speed of the test discs, researchers can investigate the influence of these parameters on the efficiency of railway transport.

Studies simulating operational railway conditions have employed the twin disc test to explore a wide range of topics crucial to railway efficiency and safety. These include the management of friction between wheel and rail, the development of new materials for railway components, the impact of environmental conditions and containments on railway operation safety, and the efficacy of surface treatments in enhancing the tribological performance of wheels and rails. The versatility of the twin disc test offers numerous possibilities for research and experimentation in the railway field, with a wealth of contributions available in major scientific databases.

The prevailing twin disc test bench in the literature the Sheffield University Rolling Sliding (SUROS) twin disc. A detailed description of the test rig design, structure and capabilities can be found in [52] and its schematics are shown in Fig. 3.9. This rig has been extensively utilized to explore the tribological behaviour in various contact conditions between rollers, such as Rolling contact fatigue (RCF) [53], coefficient of friction of rails [54], curve lubricant performance [55], mild and severe wear modelling [56], temperature in contact [57], adhesion phenomena [58, 59].

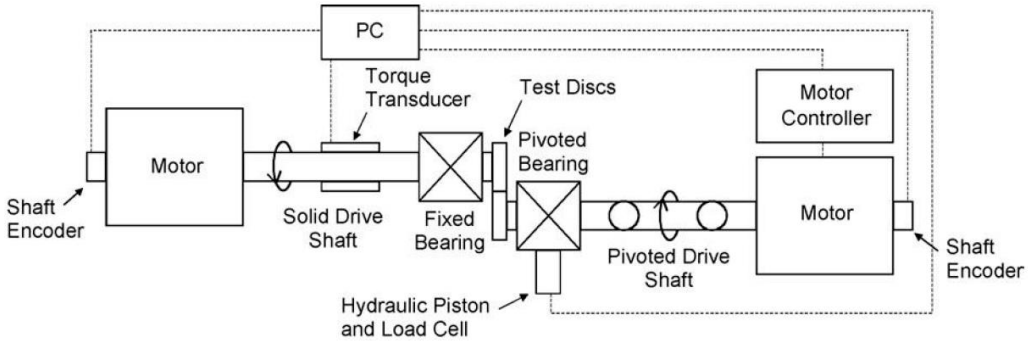

Figure 3.9: schematic of the SUROS test rig. Taken from "Development of a machine for closely controlled rolling contact fatigue and wear testing" [52].

The SUROS tester is built on Colchester Mascot lathe and each disc is connected to an AC motor via a shaft fitted with encoders, thus a difference in angular speed can be easily achieved with a proper control of both motors. The normal load that presses the two discs is obtained through a hydraulic piston and a loading cell allows to measure the contact force.

In the SUROS roller-rig setup, the upper disc functions as the rail disc, while the lower disc serves as the wheel disc. Both are powered, and the speed of each shaft is monitored during tests by the aforementioned encoders. By precisely controlling the two motors, steady state creepage conditions can be attained. The creepage value can be determined by the following equation:

$$\xi = \frac{\omega_w r_w - \omega_r r_r}{0.5 \cdot (\omega_w r_w + \omega_r r_r)} \tag{3.22}$$

Where ω is the rotational speed, r is the disc radius and the subscripts r and w refer to the rail disc and wheel disc respectively. Moreover, the rail disc shaft is equipped with a torque transducer, as shown in Fig. 3.9, capable of measuring the torque on the shaft during the test. As the motors are controlled to achieve steady-state speed

conditions, inertia terms can be disregarded, allowing the adhesion coefficient μ to be calculated, as at a certain instant its value will be:

$$\mu = \frac{T_r}{N r_r} \tag{3.23}$$

Where T_r is the torque measured by the transducer, N is the normal load, which is measured by the load cell, and finally r_r is the rail disc (upper one in Fig. 3.9) radius.

On one hand the contact geometry is very different than the one in the real wheel-rail case, on the other the disc specimens used in tests that make use of the SUROS machine are cut from real wheels and rails, i.e. in [57] the discs were cut from UIC60 900A rail steel for the rail disc while the wheel disc was cut from R8 T wheel steel. This particular consideration goes a long way towards ensuring that the tribological results mirror the real-life case. Fig. 3.10 shows the shape of the discs and how they are cut from their real-life counterparts. Please note how the discs are cut from the closest possible level to the wheel-tread and rail-head surfaces.

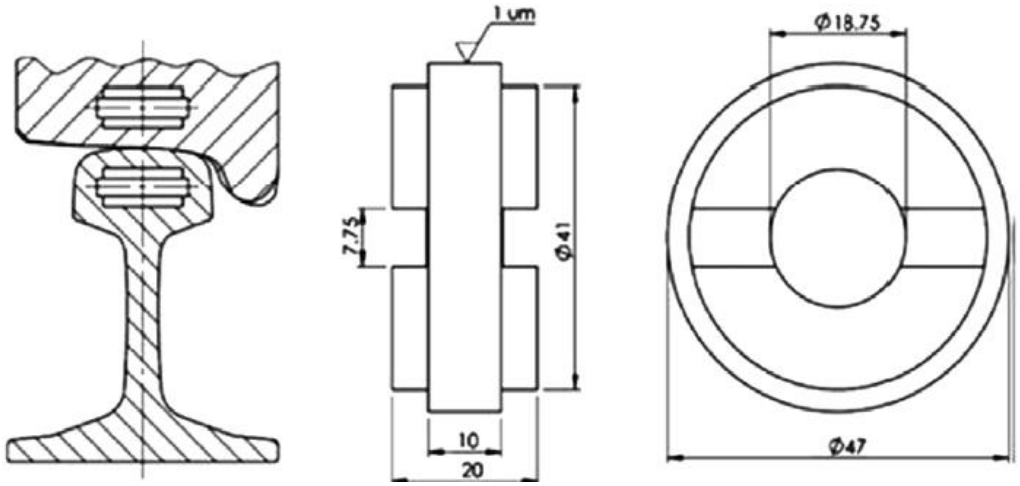

Figure 3.10: Extraction and dimensions of SUROS specimens. Taken from "Assessment of railway curve lubricant performance using a twin-disc tester" [55].

In another experimental campaign by Hu et al. [60] using the SUROS twin disc tribometer and aiming to quantify the wear of driving versus driven discs, the material chemical composition and hardness are shown in Table 3.2.

Type	Grade	Chemical composition (*wt*%)					Hardness/$HV_{0.5}$
		C	Si	Mn	P	S	
Rail	R260	0.62–0.80	0.15–0.58	0.70–1.20	≥0.025	≥0.025	287 ± 10
Wheel	C-class	0.67–0.77	0.15–1.00	0.60–0.90	0.030	0.005–0.040	388 ± 9

Table 3.2: chemical composition and hardness of the disc specimens used in [60].

Depending on the characteristics under investigation, the values of the rotational speed and normal load may vary. Many tests rotate the wheel-disc to a value of 400 rpm, while exerting a load such that the contact pressure reaches 1500MPa. Furthermore, in tests in which both discs' velocity is controlled, creep has been varied from 0.01% to 20%. For reference, during normal operation of a railway vehicle, creep usually tends towards 0.1% to 0.5% nevertheless, being the contact

of the two discs not representative of the real phenomena, very high creep values might be required.

An alternative design involves a single motor system, exemplified by the rig used by Zhao et al. used to investigate the effect of spherical dents on microstructure evolution [61]. A schematic of the rig is shown in Fig. 3.10. The upper disc simulates the rail while the lower one simulates the wheel. This test bench uses a single DC motor and gear transmission to actuate the lower roller (wheel). However, this design presents challenges in replicating specific creep conditions without altering the gear pairs.

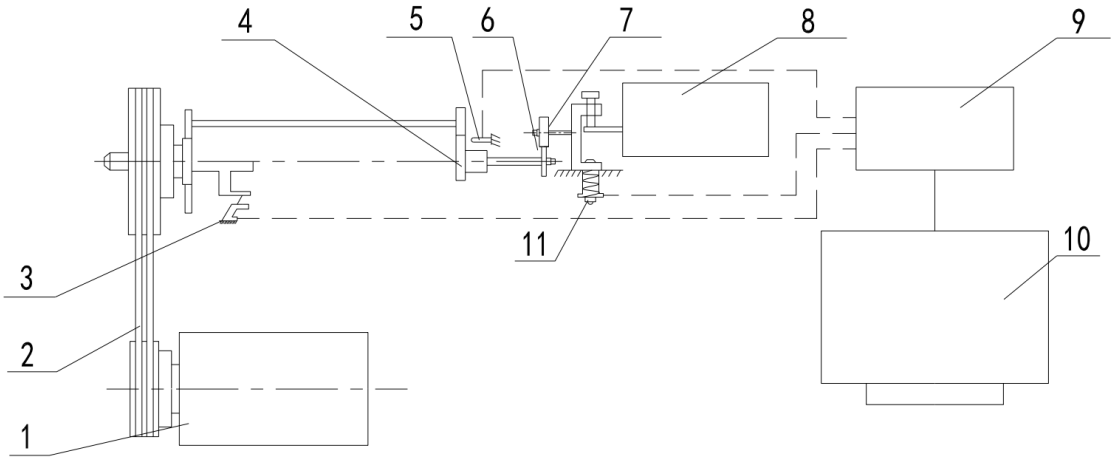

Figure 3.11: Schematic of the Twin Disc tester used in [61]. 1. DC motor; 2. Drive belt; 3. Torque sensor; 4. Drive shaft gears; 5. Photosensor; 6. Lower roller; 7. Upper roller; 8. Driven shaft gears; 9. Controller; 10. Computer; 11. Load sensor. Taken from:" Effect of spherical dents on microstructure evolution and rolling contact fatigue of wheel/rail materials".

Nevertheless, the use of gears, specifically gearboxes, can prove to be necessary in certain conditions. In case the experimental campaign requires the discs to have a high value of torque, it is unlikely that a single electric motor can supply it. For this reason, a gearbox might prove essential in the design of a twin disc bench.

In this rig the normal force is obtained and adjusted through a compressed spring, not featured in Fig. 3.10, while a torque sensor (3) and load sensor (11) measure the dynamic characteristics of the test.

The specimens in this rig are made from real wheel and rails as well. Their chemical composition of the two steels is shown in Table 3.3, while Fig. 3.10 shows their structure and design.

Roller	C	Si	Mn	P	S
Wheel	0.56–0.60	≤0.40	≤0.80	≤0.020	≤0.015
Rail	0.65–0.75	0.10–0.50	0.80–1.30	≤0.025	≤0.025

Table 3.3: chemical composition of the disc specimens (wt%). Taken from:" Effect of spherical dents on microstructure evolution and rolling contact fatigue of wheel/rail materials".

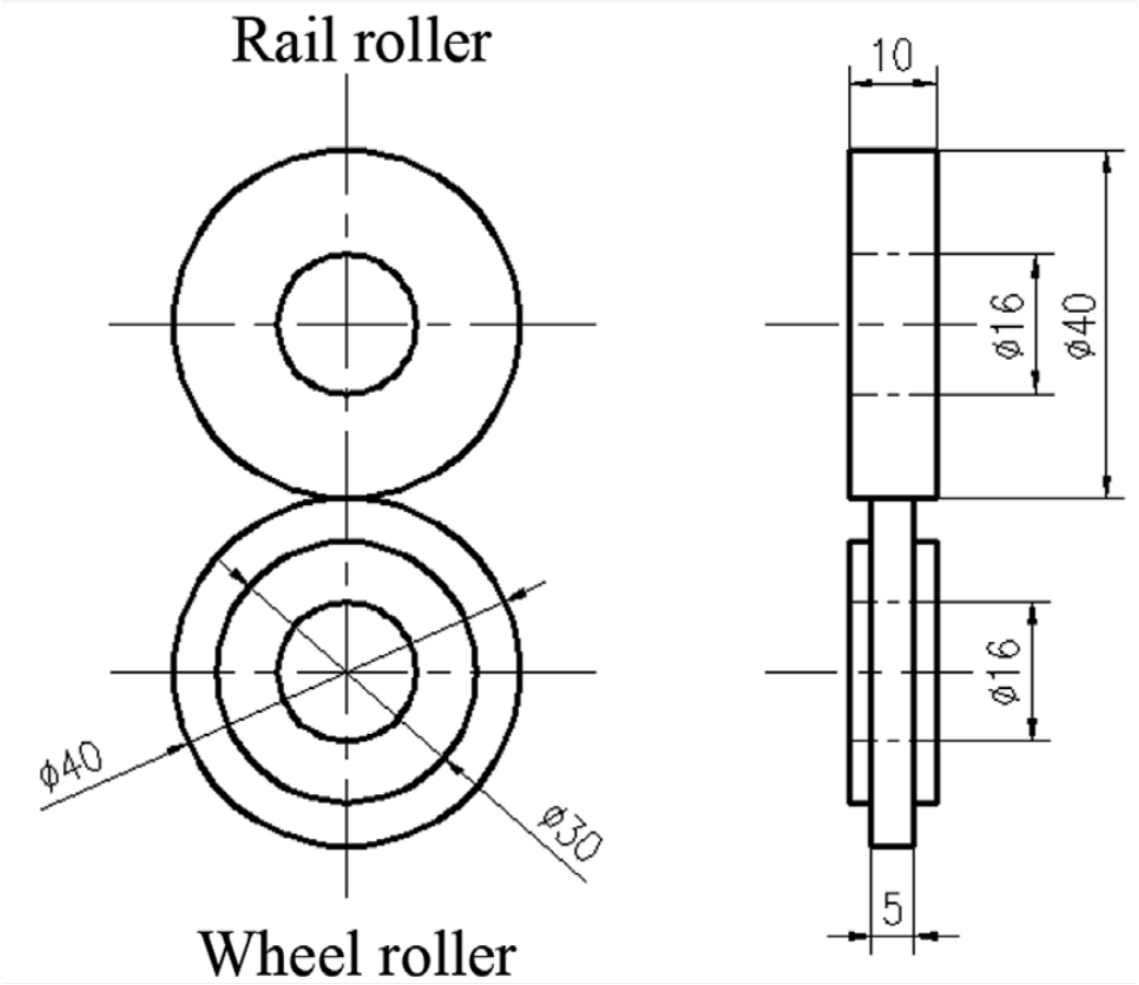

Figure 3.12: Scheme of the two rollers used in [61]. Taken from:" Effect of spherical dents on microstructure evolution and rolling contact fatigue of wheel/rail materials".

As the work in [61] investigates the effect of spherical dents, the specimens also feature dents with a diameter of approximately 1.5 mm, obtained through the use of a pendulum machine for the rail roller and with a hammer for the rail roller. One of the conclusions the research group reached, was that the growth of the crack is not consistent to the real-life case as the contact geometry differs.

Twin disc tribometers can also be a tool to study the effect of third body materials in the wheel-rail contact, as explained by Gutsulyak et al. [62]. Their research used two different twin disc machines, the "Phoenix Tribology TE73 twin disc instrument", shown in Fig. 3.11 and the "Phoenix Tribology TE73H twin disc instrument", shown in Fig. 3.12.

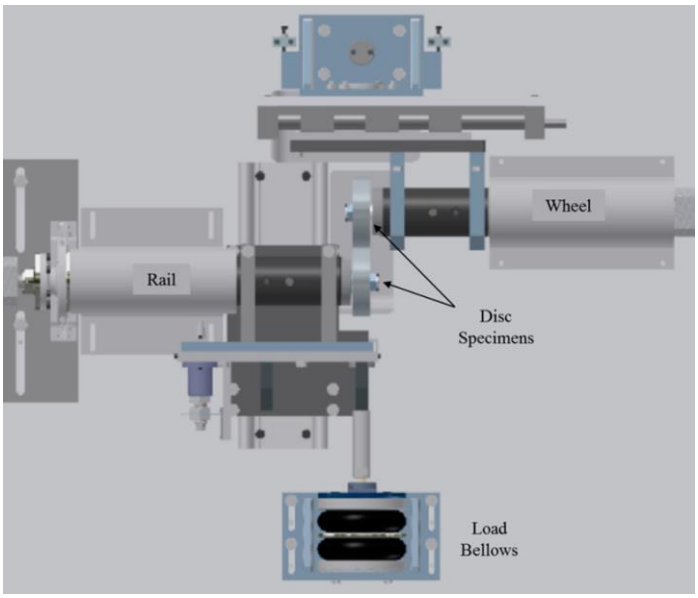

Figure 3.13: Overhead view of the Phoenix Tribology TE72 twin disc instrument. Taken from "Twin disc evaluation of third body materials in the wheel/rail interface" [62].

The main difference between the two tribometers are the specimen size, as the TE72 discs have a diameter of 50 mm, while the TE73H uses discs with 300 m diameter. Whereas the TE72 specimens were made from real wheel and rail steel, the same was not possible for the TE73H, therefore its specimens were made of D2 steel and treated in order to reach the desired surface hardness. In both cases, the disc specimens were polished with grit paper to obtain similar surface roughness.

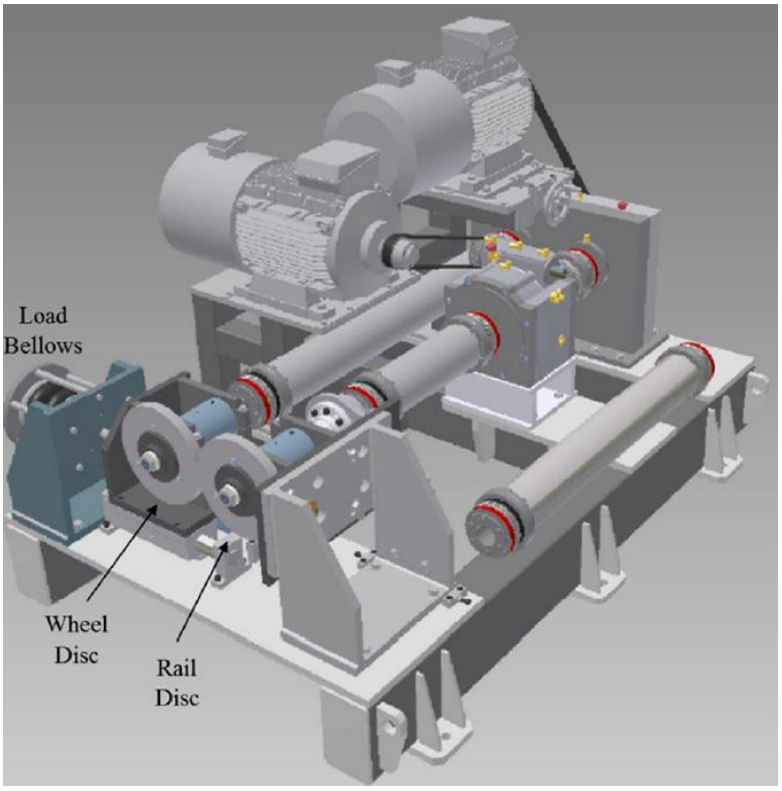

Figure 3.14: CAD model of the Phoenix Tribology TE73H twin disc instrument. Taken from "Twin disc evaluation of third body materials in the wheel/rail interface" [62].

The two tribometers use the same design solution when it comes to powering the discs and pressing them against each other. In both machines, each disc is powered by its own electric motor, thus creep is achieved by controlling the speed of each disc independently. Furthermore, as shown in Fig. 3.11 and Fig. 3.12, both machines use pneumatic loading bellows to reach the desired contact pressure and force transducers send a feedback signal in order to accurately control the contact pressure between the discs. Finally, torque transducers measure the torque level which in turn is used to determine the coefficient of traction.

Strey et al.'s [63] work focuses on linking and comparing the effects of rolling contact fatigue between railway wheels and the classic win-disc specimen. The schematic of the twin disc machine used for their experimental campaign is shown in Fig. 3.13.

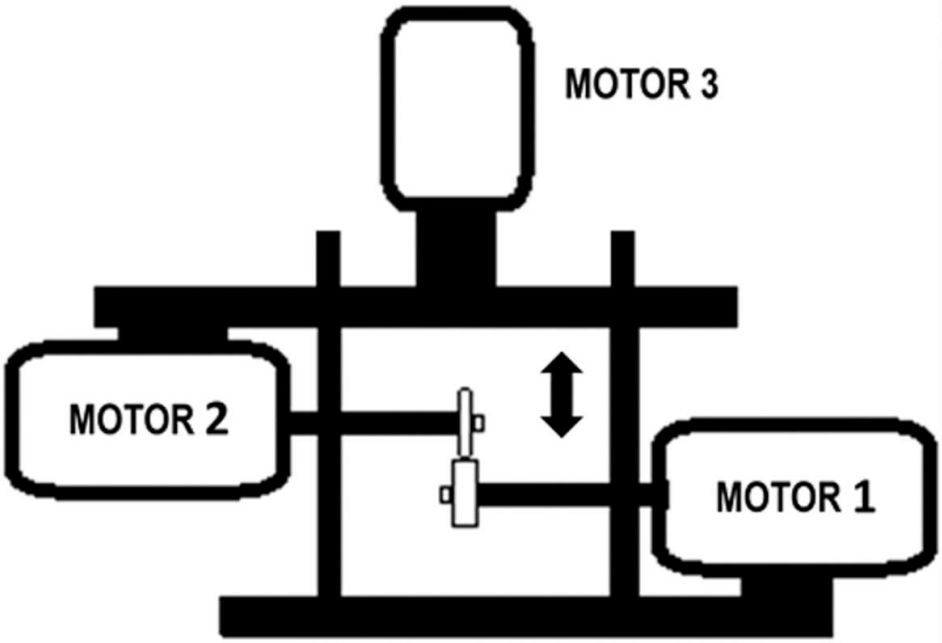

Figure 3.15: Schematic drawing of the twin-disc tribometer used in [63]. Taken from "Comparison of rolling contact fatigue damage between railway wheels and twin-disc test specimens".

Similarly to other twin disc specimens seen so far, both disc specimens were cut from existing wheels and subsequently quenched. Additionally, the upper disc was heat-treated in order to obtain a pearlitic microstructure. Table 4.4 shows the chemical composition of the discs. Fig. 3.14 shows the design of the discs.

	C	Si	Mn	Cr	Cu	Mo+Nb
Disc	0.71	0.43	0.84	0.27	0.21	0.22

Table 3.4: Nominal chemical composition of the steel used in [63] (%wt).

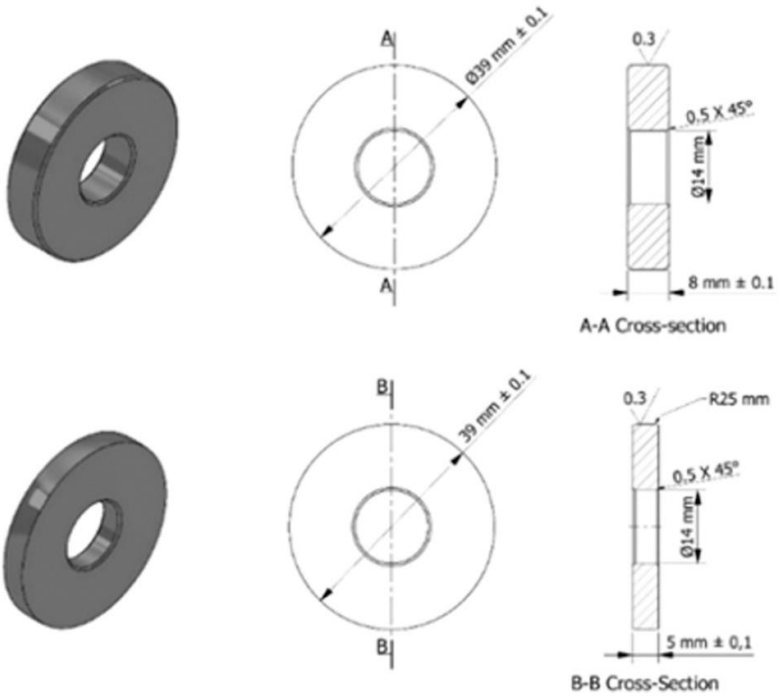

Figure 3.16: Design of the disc specimens used in [63]. Taken from "Comparison of rolling contact fatigue damage between railway wheels and twin-disc test specimens".

As is the case with twin disc tribometers featuring two electric motors, slip is achieved from the angular speed difference between motor 1 and motor 2 (in Fig. 3.13). Motor 3 is used to apply the normal load through a spindle system. Software controllers were used to monitor and set the desired speeds and applied load, which is kept constant throughout the tests.

The aim of this work was to compare the performance of twin disc specimens and wheels removed from operation in regards to the damage caused by RCF. They found that while twin disc proves to be a good method to investigate the phenomena on the surface of the wheel, the tribometer fails to replicate conditions if the cracks have a more advanced propagation. They attributed this difference to the presence of contaminants in the wheel's normal operation and the difference in contact between a wheel-rail system and twin disc one.

The review carried out by Rocha et al. [51] is valuable as it summarises the state of the art of twin disc tribometers for applications in the railway, an delves into the different characteristics the machine is used to investigate. The different groups identified by the research group are:

- Evaluation of materials for rails and wheels: tests usually consist in assessing the properties of new materials to be used in the railway industry. Twin disc tribometers are an ideal instrument as they can replicate both sliding and rolling motions and are more cost-effective than other test benches.
- Environmental condition: the tests in this category aim to replicate the effects of the main environmental conditions that influence the wheel-rail contact. These are rain, relative humidity, temperature, leaves, and sand. The

studies' main goal was to evaluate how these contaminants influenced the coefficient of adherence.

- Operating condition: this group includes studies that aim to link the increasingly harsh operating conditions required in the railway industry to the conditions in the contact between wheels and rails. Fig. 3.15 shows the correlation of field operating parameters with those used in the twin disc tests and their range.
- Friction management: tests either consist in evaluating the coefficient of friction between the flange of the wheel and face of the track gauge or the friction between top of the rail and the wheel rolling surface. These tests include the characterization of lubricant properties.
- Simulation of defects and their consequences: twin disc machines are used to both generate defects and study them. The defects include white layer, defects originating from RCF, and defects that cause local geometric alterations, such as dents, holes, and scratches.
- Railway signalling: Railway signalling predominantly relies on circuit paths for operation. In this signalling model, the rails are electrically energized, and the track is segmented into sections by insulating joints placed between the rails, effectively creating electrically isolated sections. Research on railway signalling in the literature is primarily directed towards investigating the impact of third bodies on the loss of electrical contact between the wheel and the rail. Such interference can potentially result in erroneous signals indicating a free section in the track circuits, posing a significant safety risk to railway operations.
- Surface treatments on rails and wheels: this subject includes the main surface treatments used on wheel and rail steels in order to increase their lifespan in operating conditions. The three treatments identified were laser cladding, laser-dispersed treatment, and laser shock peening.
- Validation of computational/mathematical models: computational modelling of the wheel-rail tribological system is inherently complex due to the involvement of mechanisms spanning from atomic to macroscopic scales, as stated in the prior chapter. To ensure the reliability of these models, it is crucial to experimentally validate the characteristics of materials under stresses that accurately simulate railway operating conditions. The twin disc setup, designed to operate under contact loads involving both rolling and sliding, offers an adequate instrument for investigating these material properties.

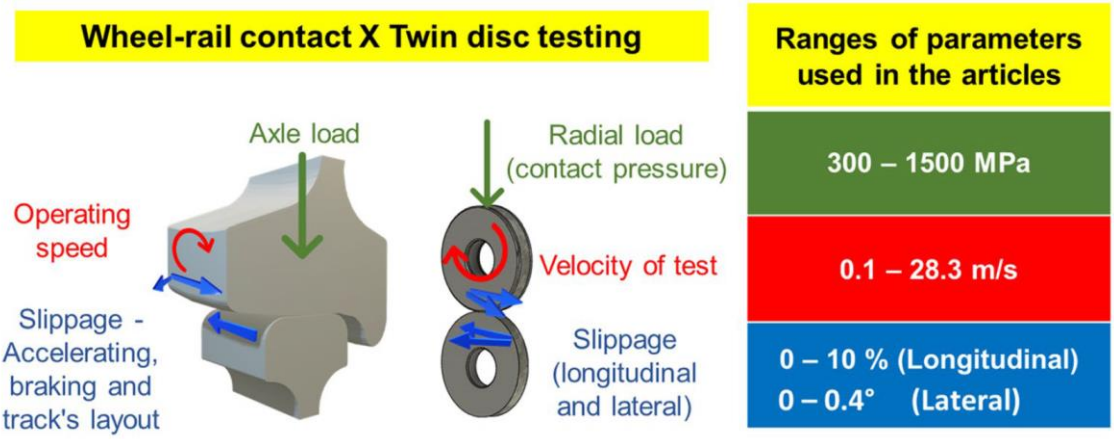

Figure 3.17: Correlation of field operating parameters with those used in the twin disc test and the range of values used in the category tests. Taken from "Using twin disc for applications in the railway: a systematic review" [51].

However, in the literature, twin disc setups commonly share a limitation: the contact geometry between the discs is oversimplified and not representative of actual contact conditions. In many cases, as observed in setups like the SUROS rig, the discs utilized are essentially two cylinders, which deviates significantly from the actual wheel-rail contact geometry. Even in instances where the wheel-simulating disc mirrors an actual wheel's profile, the rail-representing disc still has a cylindrical shape [63]. This discrepancy presents a challenge in accurately replicating the nuanced interactions present in real wheel-rail systems.

4.Design of the novel Twin Disc tribometer

The core of this thesis is the conception and design of a test bench that can faithfully emulate the process of wear of a wheel of a railway vehicle. Ideally, testing can be done on an actual wheel and validation of the experimental results would be conducted on field, however, reproducing the scenario in a laboratory setting is rather complex, as it would entail high costs and large laboratory facilities. Therefore, to approach this issue, a scaled test rig is often preferred. In order to design it different hypothesis and design choices have been made, which will be extensively explored.

As stated in chapter 2.1, one of the objectives of a tribometer is to provide data that allows to estimate wear coefficients that can be used in a model, which in turn can quantify wear and worn material of the real case.

This chapter will be structured as follows. The first section describes the design constraints and hypotheses, as well as describe the components which are already available in the laboratory, which will be used in the final design. Then, the adopted scaling strategy will be described, including the different scaling factors and the profile of the wheel disc. Afterwards, attention is given to the design choices, in particular the kinematic and dynamic parameters of the discs, the correction of the lateral curve of the rail disc, the application of the normal force, and other additional design choices. Subsequently, a feasibility analysis is carried out, by focusing on the bearing service life and a structural analysis of the most critical component. A description of the possible tests that can be conducted using the newly designed bench will then be described. Finally, an overview of the twin disc machine summarizes the design.

4.1 Design constraints

4.1.1 Conservation of the maximum pressure

As illustrated in earlier chapters, wear is closely related to the maximum pressure reached in the contact patch between rail and wheel, both in energetic and sliding models. Experimentally, it is shown that for the same materials in contact, with the same surface roughness, sliding speed and pressure are the factors that influence the worn material the most. While it is trivial to control the sliding speed in a twin disc tribometer, as the prevalent method featuring two independent motors easily allows that, particular care has to be put on the contact pressure, since it depends on both the normal load and the shape of the surfaces in contact.

In order to faithfully reproduce the contact, the twin disc machine in this paper will be designed with the intent of reaching the same maximum pressure in the contact between the discs as in the contact between wheel and rail.

4.1.2 Operating conditions

In designing a test bench, it is crucial to determine which real conditions it must simulate. Since the bench is designed to carry out wear tests, factors such as contaminants, testing of new materials or studying the effect of defects will not be considered in the designing phase. The main parameters concerning wear tests are the angular speeds at which each roller spins and the contact pressure they will reach when pressed. In the wheel-rail systems these are caused by the vehicle speed and load.

As design parameters, two distinct conditions have been identified, conditions of a passenger wagon, i.e. an axle load of M=12 t/axle and a speed of V=80 km/h, and for a freight wagon, i.e. an axle load of M=22.5 t/axle and a speed of V=60 km/h, which is a typical operating condition of a European freight wagon [64]. These conditions are presented in Table 4.1.

	Passenger	**Freight**
Axle load [t/axle]	12	22.5
Speed [km/h]	80	60

Table 4.1: Different conditions that the designed twin disc machine will be able to simulate.

The materials that will be used for the rollers will replicate as closely as possible the actual steels used for wheels and rail, especially their surface hardness.

4.1.3 Refurbished components

The railway engineering laboratory at Politecnico di Torino features already available components from pre-existing benches. In early design stages it became self-evident how to minimize costs and promote sustainability, the newly twin disc machine had to refurbish and make use of said components. Thus, a starting point has been defined and during the design process only the strictly necessary components will be manufactured.

Firstly, the rig will be mounted on a rigid frame, available at the railway engineering lab. The CAD model of the frame is shown in Fig. 4.1. The frame's geometry has been measured and replicated in the 3D CAD software SOLIDWORKS.

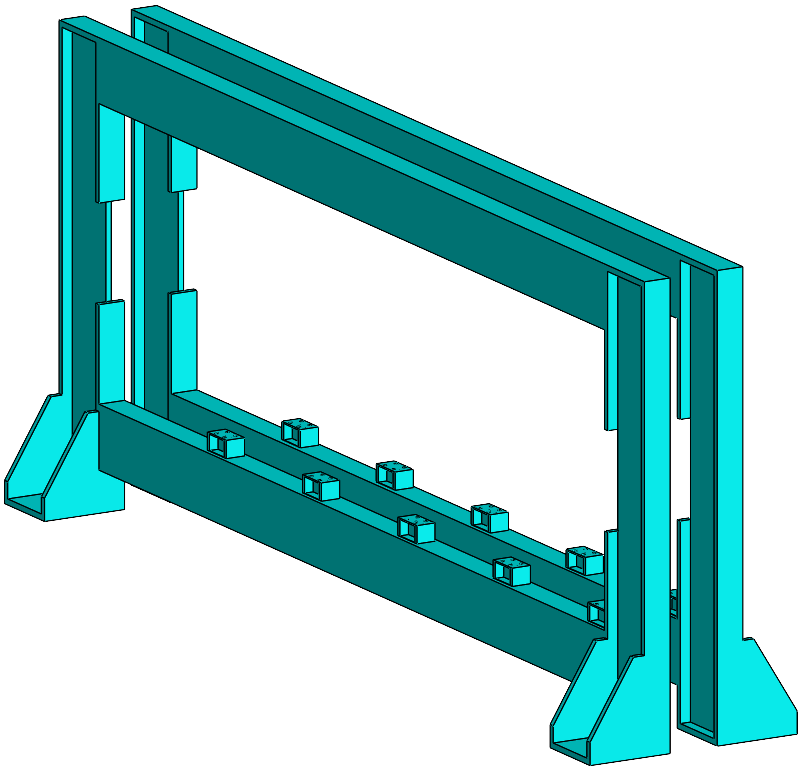

Figure 4.1: Rigid frame on which the test bench will be mounted.

To power the discs, as previously described, the use of two independent motors is highly advised as this allows to easily achieve creepage between the rollers. Fortunately, two brushless motors are already available in the railway lab. The CAD model of the motor is shown in Fig. 4.2.

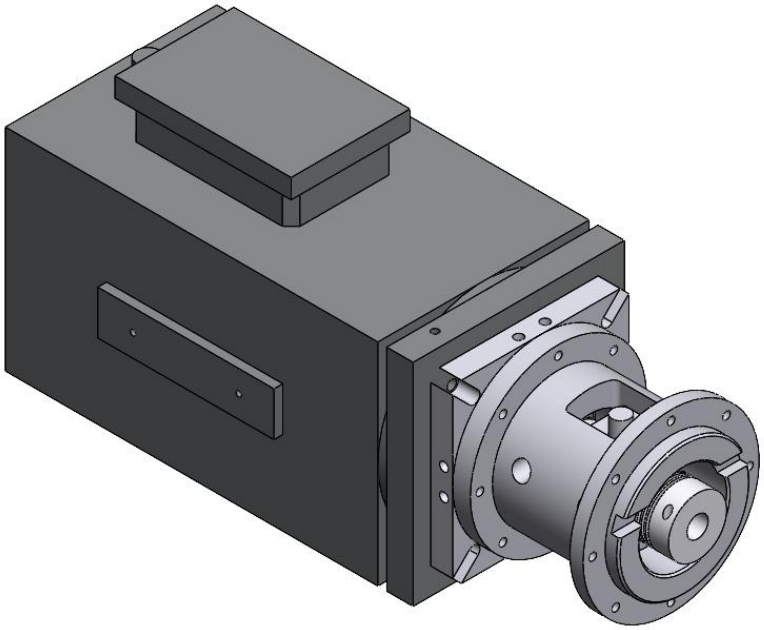

Figure 4.2: The brushless motor ACM BRL 220 available in the lab.

The motors include a centring sleeve, joints and high-resolution digital encoders that are used to measure the rotational speed of each roller. More in detail, the motor is a synchronous permanent magnets motor (brushless) motor ACM BRL 220. It provides a maximum torque of 650 Nm and a nominal torque of 150 Nm at 2000 rpm.

The motors can be coupled with two identical mechanical shafts, shown in Fig 4.3. These are also already available in the lab. These will evidently be used to power the discs.

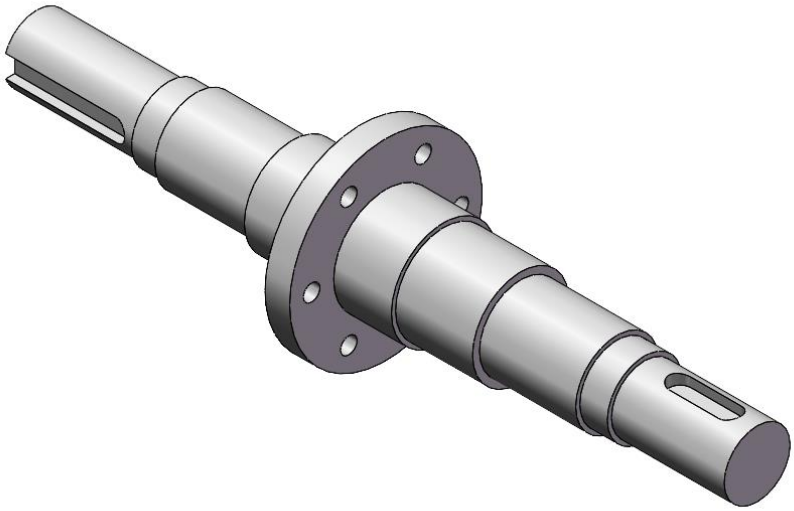

Figure 4.3: Mechanical shaft that will be refurbished.

Finally, the lab is also equipped with supporting components for the shaft, shown in Fig. 4.4. The shaft support (Fig. 4.4.a) also includes ball bearings.

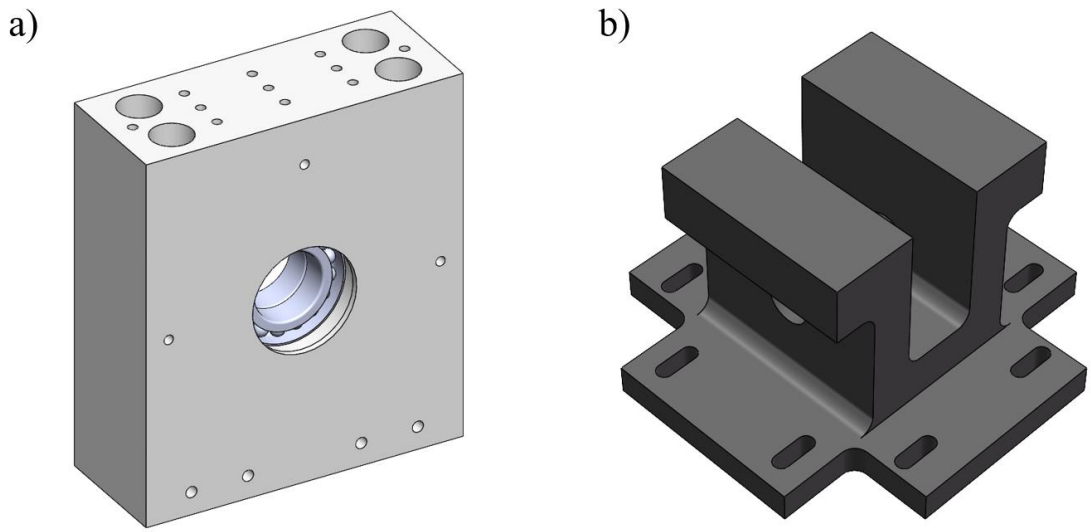

Figure 4.4: (a) Shaft support. (b) Support for the shaft support.

From this starting point, the rest of the twin disc machine will be designed. The most important elements to take into consideration are:

- Scaling,
- Shape of the discs,
- Loading to obtain the desired contact pressure,
- Pre-test and post-test measurements.

4.2 Scaling

Different scaling strategies have been described in chapter 3.2.1. These are traditionally used to design scaled roller-rig test benches, however the innovative design of the twin disc described in this thesis, aims to maintain the same contact pressure between the discs and the real wheel-rail contact. Consequently, Pascal's similitude model is the one applied in this work, as it ensures a unitary scaling factor for the contact pressure. The scaling strategy, applied to the INRETS scaled roller-rig, firstly requires for a scaling factor for length to be defined.

The most appropriate size scaling factor for the discs is selected considering several critical constraints, mainly the torque and rotational speed limitations of the readily available motors as well as the need for a compact size of the test rig. In fact, although Pascal's scaling strategy is the most used when investigating the wheel-rail contact tribology, it still features some drawbacks. Precisely, Pascal's strategy leads to a unitary scaling factor for peripheral speeds, thus requiring high values of the total power supplied to the discs. Small radii of the rollers would bring to huge angular speeds, while large radii would require the motors to provide big torques. These limitations could be partially overcome with the installation of gearboxes, which however would increase the complexity of the bench layout and the overall costs of the test rig. Eventually, the size scaling factor is chosen equal to $\psi_l=5$. This value allows to adopt the motors available, and the components mentioned above, which were realized by the research group for test benches developed in past activities [65, 66]. Furthermore, this value, as seen in the previous chapter, is frequently adopted for the rollers used in scaled roller-rigs found in the literature.

Defined a scaling factor for the size of the discs, Table 3.1 can be used to view the values of the other factors. For convenience, Table 4.2 shows the most important scaling factors that will be obtained using Pascal's strategy with a size scaling factor equal to 5.

Quantity	Scaling factor (Pascal)
Length	5
Area	25
Volume	125
Time	5
Speed	1
Mass	125
Force	25
Density	1
Weight	125
Young's Modulus	1
Stress	**1**
Stiffness	5
Creep Force	25
Inertia	3125

Table 4.2: The main scaling factors obtained through Pascal's similitude model.

Please note that while Pascal's similitude model ensures a unitary scaling factor for the contact pressure, it does not ensure the similarity of the contact patch area. This stems from the fact that a longitudinal curvature is introduced in the disc simulating

the rail, which is null in the real system. Therefore, a major novelty of the designed twin disc is that the rail profile curvature is slightly modified to keep a coherent scaling of the contact area, and normal load, which will be elaborated later on.

This scaling strategy is an upgrade to the traditional twin disc setups, as it allows to obtain results that can be directly related to typical operating conditions of different types of railway vehicles, thus overcoming the main limitation of twin discs, that are used in most cases as basic tribometers.

Obtained a scaling factor, it is crucial deciding what real wheel and rail profiles are going to be scaled down. To simulate the most common contact scenario, the profiles should be representative of the main profiles used in the industry. Consequently, the profile of the wheel will derive from the standard ORE S1002, and the rail will stem from the UIC 60 profile. The profile of an ORE S1002 wheel is shown in Fig. 4.5.

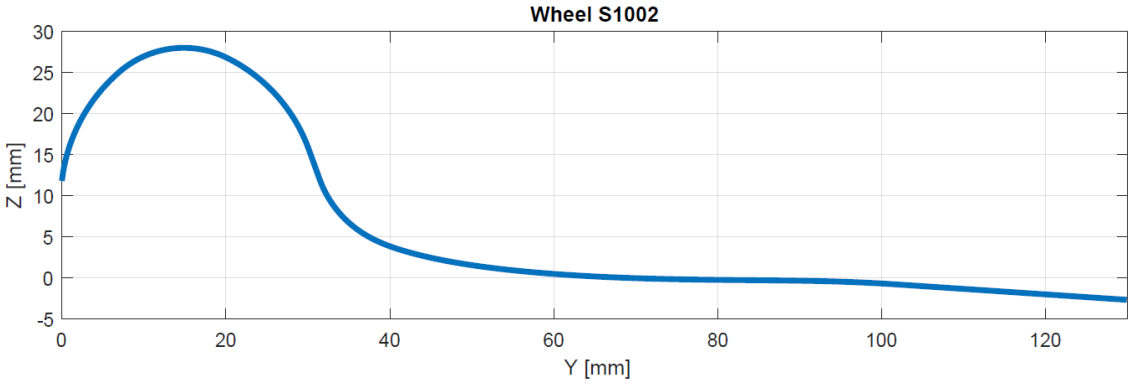

Figure 4.5: Wheel ORE S1002 profile. The coordinate Z=0 corresponds to the tread of the wheel.

The wheel profile is not modified during the scaling process. Therefore, the profile of the disc representing the wheel is easily obtained by dividing the profile to the size scaling factor (ψ_l=5). The wheel roller's profile is thus shown in Fig.4.6.

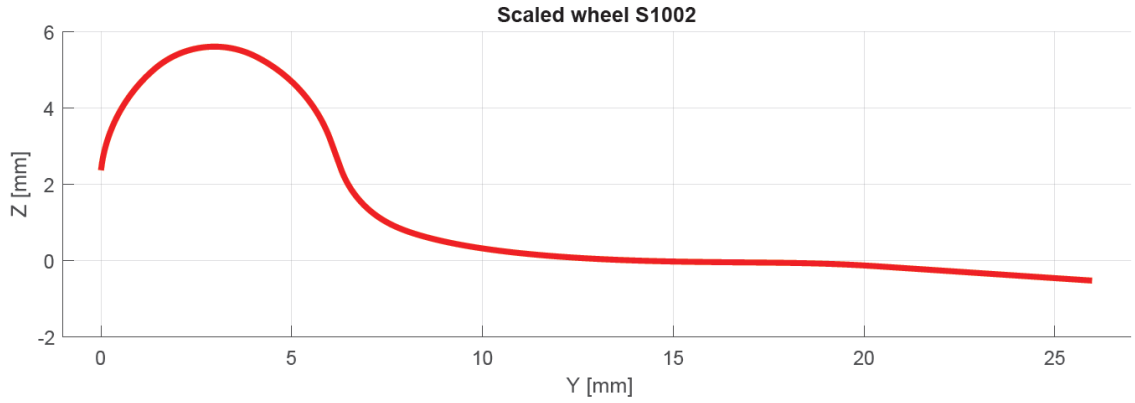

Figure 4.6: Scaled wheel ORE S1002 profile.

For the following calculations, the tread of the real profile is considered the ideal contact point, and the longitudinal diameter of the wheel at that point is:

$$d_t = 920\ mm \qquad d_{t_{scaled}} = 184\ mm \tag{4.1}$$

4.3 Design

4.3.1 Kinematic and dynamic parameters

To determine the feasibility of building the twin disc using the available motors, it is crucial to determine the rotational speed, maximum, and nominal torque required from them. These can be obtained starting from the conditions that must be simulated, which were described in chapter 4.1.2 and shown in Table 4.1.

In both cases the friction coefficients used for the design process will be:

μ_{max}	0.6
μ_{cont}	0.4

Table 4.3: Friction coefficients

As expressed in Table 4.2, the speed scaling factor is unitary, consequently, the wheel disc must have the same peripherical velocity as the real case. It becomes apparent how the angular speed that the disc must reach is proportional to the size scaling factor, since the disc is ψ_l times smaller than the real wheel. The rotational speed can be determined as follows:

$$\omega_w = \frac{V}{\frac{d_{t_{scaled}}}{2}} \tag{4.2}$$

Where V is the peripherical velocity, the subscript w indicates the wheel-disc, and the diameter is obtained from equation (4.1). The contact force originates from the axle load. As shown in Table 4.2, the force is scaled by a factor of ψ_l^2. Starting from the axle load wished to simulate, the normal force is computed as follows:

$$F_v = \frac{M \cdot g}{2 \cdot \psi_l^2} \tag{4.3}$$

Where M is the real axle load and g is the gravitational constant. The value of the axle load is divided by 2 as the weight is equally distributed on both wheels. This value will be necessary to obtain the contact pressure between the discs.

In order to determine the torque required by the motors, the tangential force has to be calculated first. The tangential force is caused by the friction between the discs. It is obtained as:

$$F_t = \mu \cdot F_{v_w} \tag{4.4}$$

Depending on the value of friction coefficient from Table 4.3 chosen, two tangential forces, thus two torques can be obtained, these correspond to two distinct working conditions, a maximum torque or starting torque to move the system from a static state, and a continuous or nominal torque during the test. Finally, the torque can be calculated as:

$$C_w = F_t \cdot \frac{d_{t_{scaled}}}{2} \tag{4.5}$$

Please note how the torque has the subscript w, as it is different between wheel-disc and rail-disc, unlike the forces which are the same since they are transmitted among them. Similarly, the power needed depends on the disc and is equal to:

$$P_w = C_w \cdot \omega_w \tag{4.6}$$

Using these equations, it is possible to evaluate these parameters for the two operational conditions that must be simulated, these are shown in Table 4.4.

Parameters for wheel-disc [unit]	**Passenger**	**Freight**
Peripheral speed [km/h]	80	60
Axle load [t/axle]	12	22.5
Angular speed [rad/s]	242	181
Angular speed [rpm]	2307	1730
Normal load [N]	2354	4415
Max/starting tangential force [N]	1413	2649
Continuous tangential force [N]	942	1766
Max/starting torque [Nm]	130	244
Continuous torque [Nm]	87	162
Max/starting power [kW]	31	44
Continuous power [kW]	21	29

Table 4.4: Mechanical parameters for the wheel disc.

The combination of angular speed, torque, and power obtained are compatible with the limits imposed by the motors. This applies to the wheel-disc, after the geometry of the rail-disc is determined as well, this verification will be carried out once again.

4.3.2 Correction of the lateral curvature

Currently, the profile of the wheel disc is machined to the S1002 profile with a scaling factor of 5. On the other hand, the disc representing the rail is designed starting from the standard rail profile of the UIC60. To account for the finite longitudinal curvature, a slight change of the lateral curvature is required.

The value of the said longitudinal curvature can be arbitrarily set. Ideally its value should be as high as possible, as to simulate the infinite curvature radius of the rail. For constructive reasons, the longitudinal curvature chosen is equal to 132 mm. With reference to Fig. 4.7, the known curvature radii at the contact point are as follows:

$$R_{wx} = 92\ mm \tag{4.7}$$
$$R_{wy} = 64\ mm \tag{4.8}$$
$$R_{rx} = 132\ mm \tag{4.9}$$

Where the subscripts w and r denote the wheel disc and rail disc respectively and the subscripts x and y are the directions shown in Fig. 4.7.

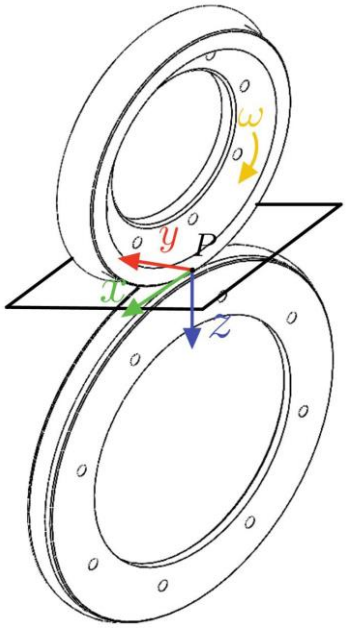

Figure 4.7: Contact between the two rollers.

The required value of the lateral curvature of the rail disc can be calculated iteratively with the application of Hertz's theory of contact, changing the value of the curvature until the desired value of contact area (and hence pressure) is achieved. According to Hertz theory, the contact area between two bodies is an ellipse with semi-axis a and b, which can be calculated as:

$$a = \alpha \cdot \sqrt[3]{\frac{3 \cdot F \cdot Req}{E'}} \tag{4.10}$$

$$b = \beta \cdot \sqrt[3]{\frac{3 \cdot F \cdot Req}{E'}} \tag{4.11}$$

$$\frac{2}{E'} = \frac{1-\nu_w^2}{E_w} + \frac{1-\nu_r^2}{E_r} \tag{4.12}$$

Where F is the normal load, E and ν are Young's and Poisson's moduli for steel. The coefficients α and β are a non-linear function of the equivalent curve radius R_{eq}, as stated in the expressions below:

$$\frac{1}{R_{eq}} = \frac{1}{R_{wx}} + \frac{1}{R_{wy}} + \frac{1}{R_{rx}} + \frac{1}{R_{ry}} \tag{4.13}$$

$$\lambda = \frac{\frac{1}{R_{wy}} + \frac{1}{R_{ry}}}{\frac{1}{R_{wx}} + \frac{1}{R_{rx}}} \tag{4.14}$$

$$\kappa \approx 1 + \sqrt{\frac{\ln\left(\frac{16}{\lambda}\right)}{2\,\lambda}} - \sqrt{\ln(4)} + 0.16 \cdot \ln(\lambda) \tag{4.15}$$

$$m = 1 - \kappa^2 \tag{4.16}$$

$$I(m) \approx \frac{\pi}{2} \cdot (1-m) \cdot \left[1 + \frac{2m}{\pi \cdot (1-m)} - \frac{1}{8}\ln(1-m)\right] \tag{4.17}$$

$$\alpha \approx \kappa^{\frac{1}{3}} \cdot \sqrt[3]{\frac{2 \cdot I(m)}{\pi}} \tag{4.18}$$

$$\beta \approx \kappa^{-\frac{2}{3}} \cdot \sqrt[3]{\frac{2 \cdot I(m)}{\pi}} \tag{4.19}$$

The maximum contact pressure can be then calculated as:

$$p_{max} = \frac{3}{2} \cdot \frac{F}{A} \tag{4.20}$$

An iterative calculation is performed to determine the required lateral curvature of the rail profile at the contact point to obtain a unitary scaling factor for the contact pressure. Using Equation (4.20), the contact pressure in the two scenarios is:

	Passenger	**Freight**
Maximum pressure [MPa]	1330	1640

Table 4.5: maximum pressure reached in the two cases.

It is found that the lateral rail curve radius on the scaled bench should be set equal to:

$$R_{ry} = 184\ mm \tag{4.21}$$

Using the values of the semi-axis it is possible to evaluate the contact patch areas for the two scenarios, both in the real case and scaled one, which are shown in Table 4.6.

	Passenger		**Freight**	
	Real	Scaled	Real	Scaled
Contact patch [mm^2]	66.38	2.66	100.93	4.04

Table 4.6: Contact patch area in the different cases.

Please note how the area scales by a factor of ψ_I^2, exactly as anticipated by adopting Pascal's scaling principle. However, it is important to highlight how the aspect ratio of the contact ellipse does not scale accordingly, showing how this is only a compromise solution.

With the value of the longitudinal radius obtained, the correction of the curvature continues by ensuring the continuity of the profile and its first derivative. Furthermore, to simulate the contact as closely as possible, the profile is canted by 1:20, as is the case of a real wheel. Fig. 4.8 shows the scaled profiles in contact.

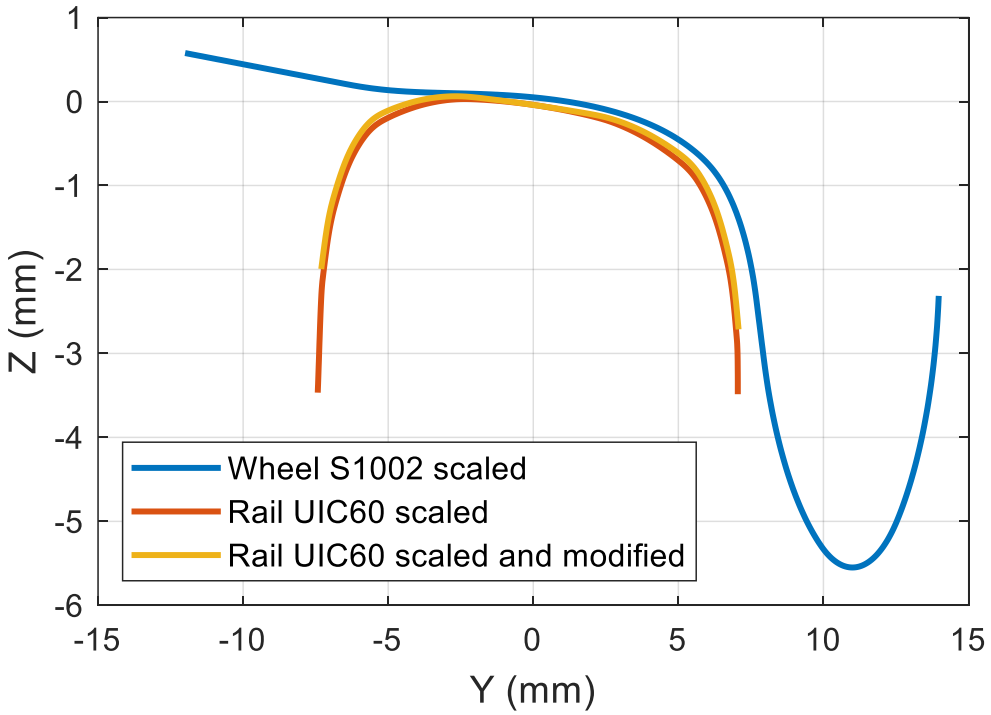

Figure 4.8: Comparison among the scaled S1002 wheel profile (blue), the scaled UIC60 rail profile canted (red) 1:20 and the modified rail profile used on the bench (yellow).

4.3.3 Design of the rollers

The discs are made of a machined rim mounted on a hub, thus allowing to test different types of profiles by simply changing the outer rim. The discs (hub and roller) are then mounted on the already available mechanical shafts, as shown in Fig. 4.9. Both the shaft-hub and the hub-roller connections are achieved by coupling them and using bolts.

Steels suitable to realize wheel and rails are listed in the EN13262 and EN13674-4 standards, respectively. Typically, wheels are realized in R7 steel, while the rails are realized in R260 steel. Obtaining the raw material of these type of steels with a shape suitable to realize the rollers is quite challenging, e.g. the rail-roller should be realized starting from a real rail, requiring a very complex design and very high costs. For this reason, the first set of rollers is realized with steels which have chemical properties similar the ones listed in the EN standards. Since the hardness is the main mechanical property that affects the wear behaviour, thermal treatments are used to obtain rollers which have hardness values close to the one of real wheel and rails.

During the experimental tests the rollers are subjected to wear leading to a modification of the original profile, affecting the contact area and pressure. To reuse the same pair of rollers for several wear tests, they have been designed to be machined several times to restore the required profiles, reducing the costs of the test bench setup.

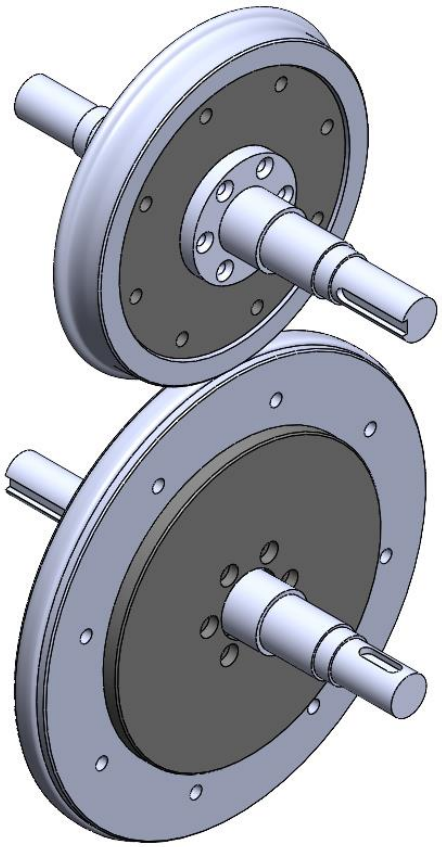

Figure 4.9: The CAD model of the final design for the discs, consisting of a hub and a roller.

4.3.4 Application of the normal force

Up to this point in the paper, the setup includes the discs, motors, and the remaining refurbished components. By adding a base plate, which is used to connect the bench to the rigid frame, the layout obtained is shown in Fig. 4.10.

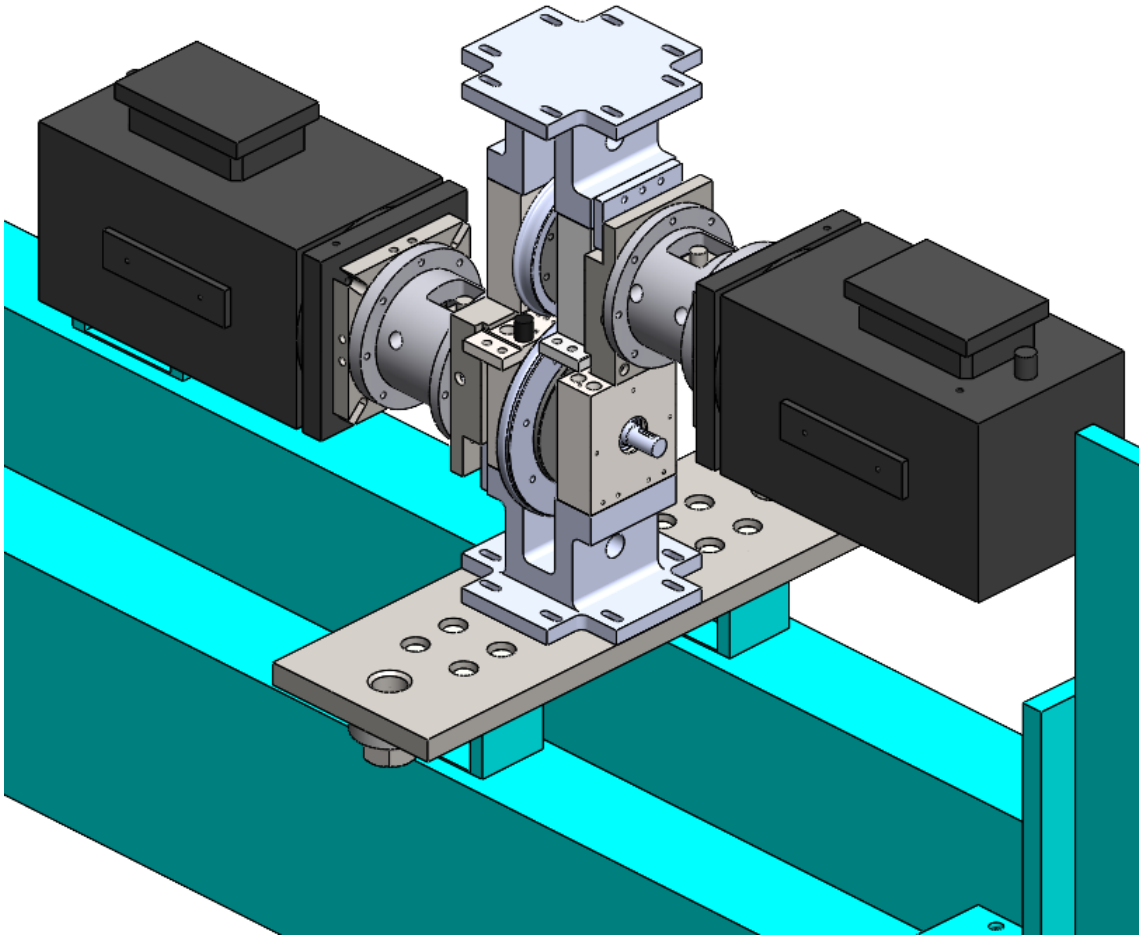

Figure 4.10: the twin disc machine design up to this point in the paper.

Because of the wear of the profiles during tests, it is necessary to design a loading system able to maintain a constant contact load also when the roller radii change due to material removal. In chapter 3 various twin disc setups have been described and it was highlighted how in literature different solutions may be adopted in order to press the discs against each other. After exploring various potential load application systems, the use of helical springs has been selected.

The contact load is applied to the wheel-roller (the upper disc in Fig. 4.10) by means of a couple of helical springs (shown in Fig. 4.11), which are preloaded by means of a screw system.

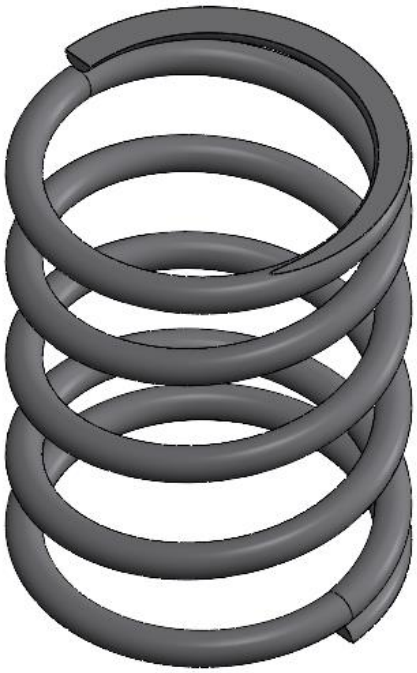

Figure 4.11: The spring chosen to apply the normal load (Model 14830).

The selection of the appropriate springs to simulate the required axle load and the maximum load reduction due to wear is a crucial aspect of the test rig design. The adopted spring must guarantee the application of the maximum design contact load without reaching their limit deflection. Furthermore, the spring stiffness should be designed in order to reduce the load loss caused by wear of the contacting discs as much as possible. In fact, when the profiles are worn out, the upper plate approaches the lower plate, thus increasing the spring length and consequently reducing the applied force. This phenomenon could be completely avoided with the adoption of a hydraulic cylinder to generate the vertical load, but this solution would entail increased costs and a more complex mechanical arrangement. Therefore, as a proper value of the spring stiffness can still partially mitigate this issue, the spring loading system is selected to be installed on the bench.

The selected stiffness of the helical springs (k=29.87 N/mm) assures a load decrease equal to 2.4% of the maximum contact load (corresponding to axle-load of 22.5 ton), when the radius of each disc is reduced by 1 mm.

This loading mechanism is placed above of an upper plate, which in turn is positioned on top of the wheel-roller group. Two steel traction rods connect the upper and lower plates, supporting the load application system and enhancing the overall stiffness of the structure. The upper plate is guided in vertical direction by linear bearings (shown in Fig. 4.13), which slide on the vertical traction rods. The helical springs act between a loading beam and the upper plate. The traction rods are threaded on both ends, on the lower side this allows to screw nuts that fastens the rig and grants stiffness, while on the upper the nuts are used to compress the springs, thus increasing the applied load. The system described is shown in Fig. 4.12.

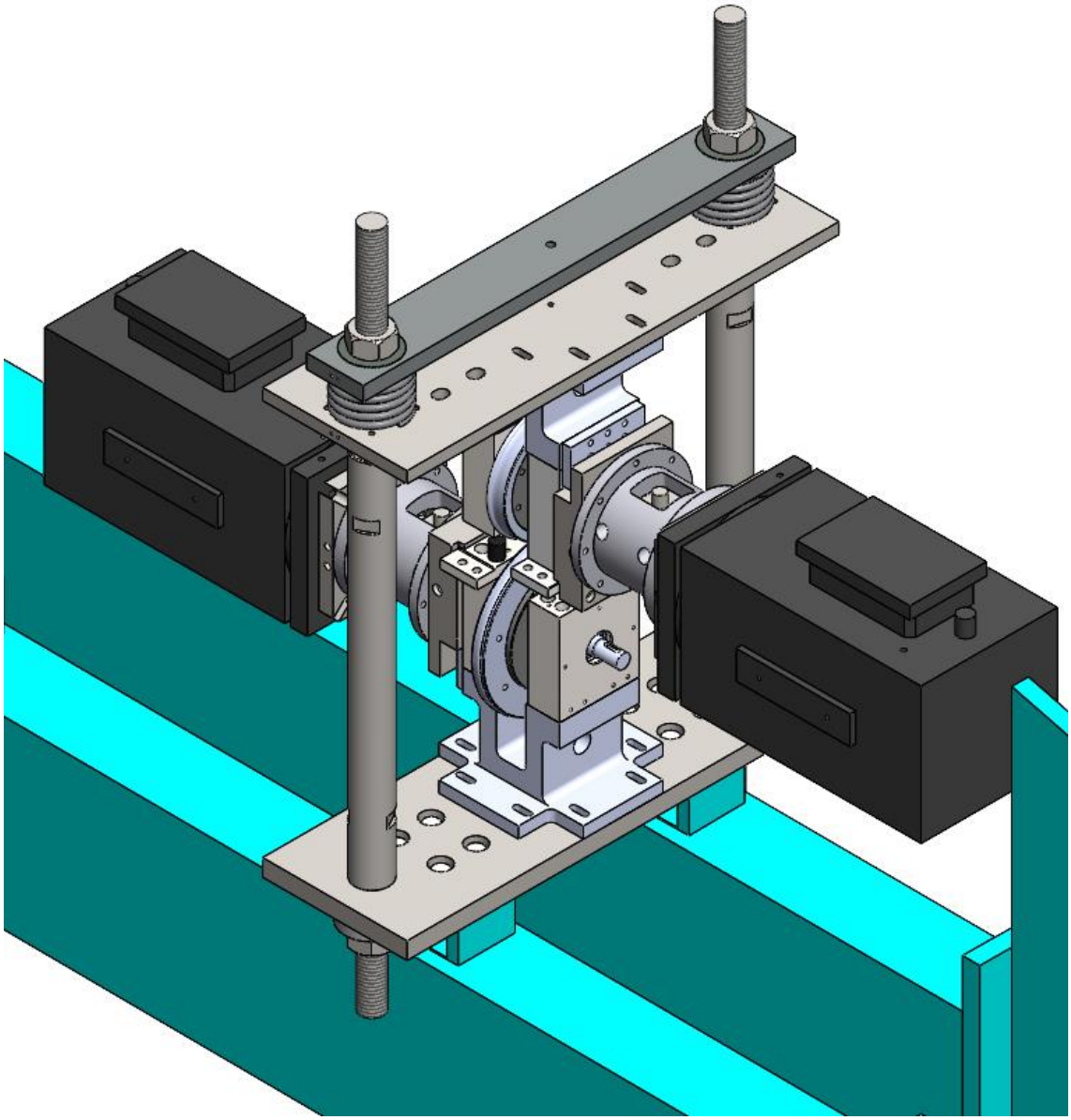

Figure 4.12: The twin disc rig featuring the compressed helical springs.

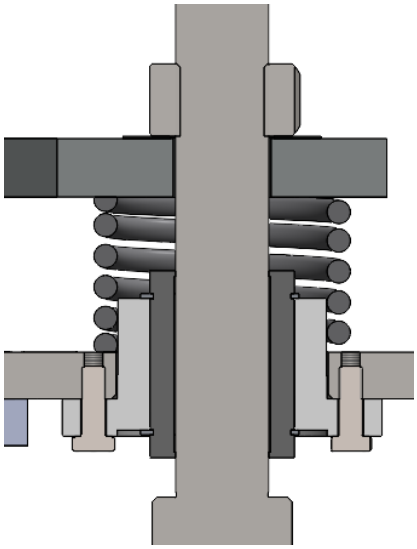

Figure 4.13: Detail of the helical spring and linear bearing.

4.3.5 Additional design choices

In this chapter the designed components will be described more in depth, and their design explained.

Fig. 4.14 shows the base and upper plates.

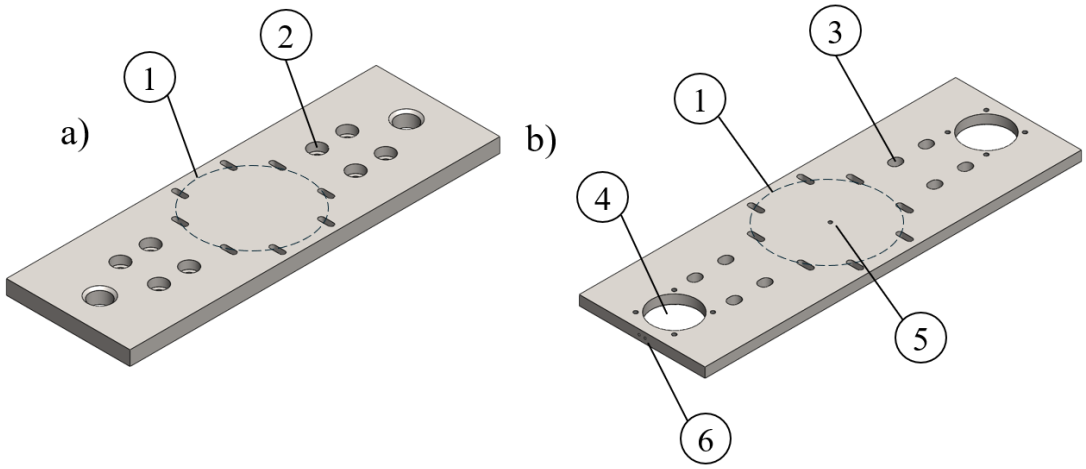

Figure 4.14: (a) the base plate and (b) the upper plate.

Number 1 in Fig. 4.14 shows a pattern of slotted holes. These holes are machined on both plates and mirror the ones featured on the component already available in the laboratory shown in Fig. 4.4.b. These holes allow to adjust the relative position between the contacting discs, thus facilitating positioning them in the optimal contact point.

The holes marked with 2 are the ones used to fasten the rig to the frame, through a bolt-nut system. These are machined to be slightly larger than the ones measured on the frame, to account for potential measurement errors and inaccuracies of the holes' geometry.

The slotted holes marked with number 3 are drilled only on the upper plate. They are used to attach additional components to the rig that allow it to carry out other tests. More about the potential tests and components will be described in chapter 6: "Future developments".

The symmetrical pattern of holes numbered 4 are used to install the two linear bearings that allow the upper plate to slide on the traction rods. The linear bearing chosen is shown in Fig. 4.15. They are fundamental to avoid a loss of vertical load due to friction forces since the applied load must act entirely on the contact patch.

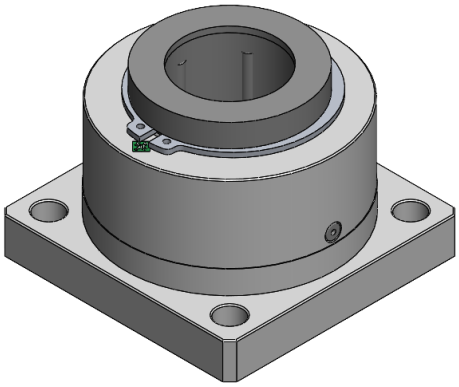

Figure 4.15: Linear bearing KFB40.

The hole at the centre of the upper plate (5) is a threaded hole which is used for the potential need of lifting the plate with a mechanical crane. Given that the upper plate will be positioned atop the bench, any elevation adjustments are likely to be accomplished using appropriate tools, which may use that hole.

Finally, the lateral threaded holes marked with number 6 are used to install a potentiometer on the side of the load application system, which will be described later. The potentiometer will work between the upper plate and the beam used to compress the springs, therefore it will feature similar holes as well, as shown in Fig. 4.16. Please note how the beam also features a central hole. This allows a string to pass through it in case there is the need to attach it to the upper plate's central hole (5 in Fig. 4.14.b).

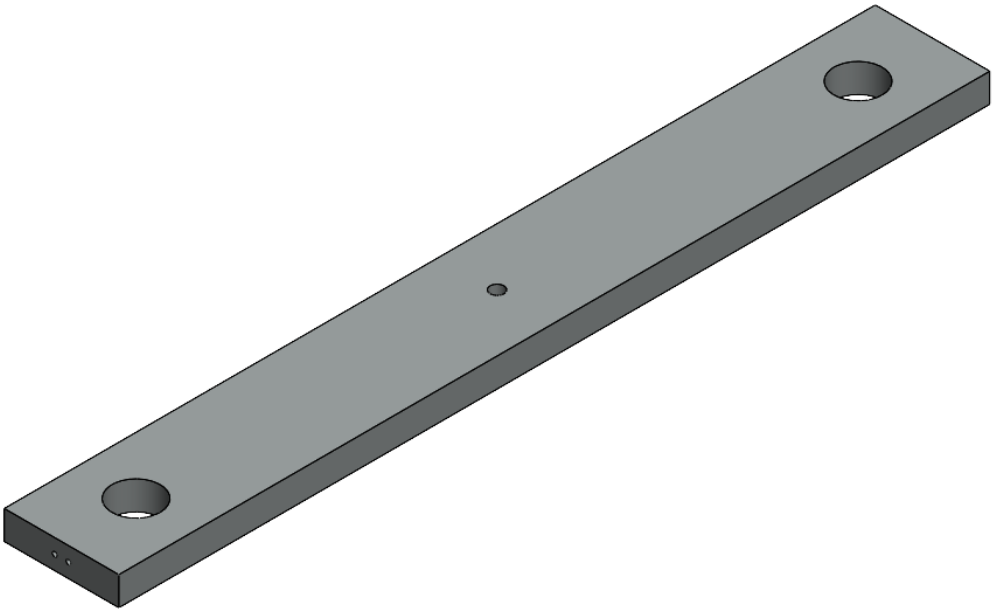

Figure 4.16: The loading beam.

As stated earlier, because of the wear of the profiles during tests, the roller radii decrease due to material removal. This will cause the helical springs to extend and would cause the two motor groups to clash with each other. Evidently, this is a

situation which must be avoided. Considering this possibility, the traction rods (Fig. 4.17) are designed appropriately.

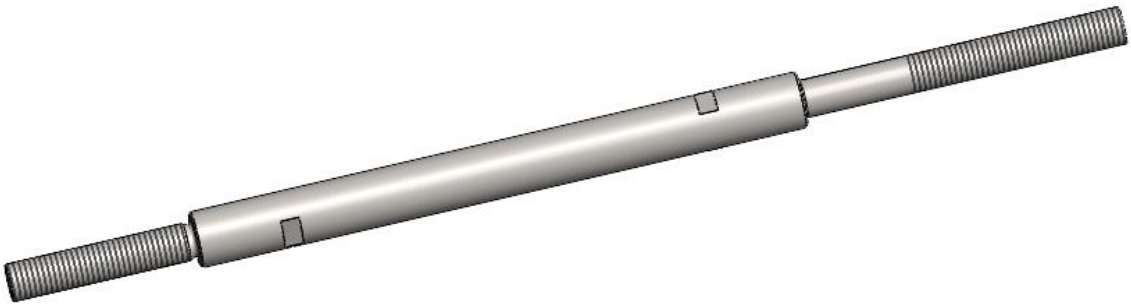

Figure 4.17: Traction rod.

The traction rod is threaded on both ends (M40) to allow the rig to be installed on the frame and to apply the normal load by compressing the helical springs between the loading beam and the upper plate. Underneath the upper threaded section, the rod is tolerated in order to couple the rod to the linear bearing. Finally, as shown in Fig. 4.17, two slots for a spanner are machined to easily allow the nuts to be screwed.

The rod features a larger diameter in its central segment. On one end it allows the rod to be placed on top of the base plate, while the other end is designed in such a way as to prevent the two motor groups from clashing. Namely, as the material is removed from the discs and the upper part of the rig slides down thanks to the linear bearings, the upper plate will encounter the larger diameter of the rod before the two shaft supports collide.

4.4 Mechanical analysis

4.4.1 Bearing service life

The ball bearings already available and refurbished are angular contact ball bearings with a single row. According to the SNFA nomenclature they are EX30 7CE1 DDL series, or 7006CE/P4A series according to the SKF standard. The ball bearing is shown in Fig. 4.18.a.

They are characterized by an inner diameter of 30 mm, a 15° contact angle, and an external cage made of phenolic resin. They are arranged back-to-back (< >), as shown in Fig. 4.18.b, and it was assumed that they do not have to withstand an axial load, thus disregarding the cant angle of the rail disc.

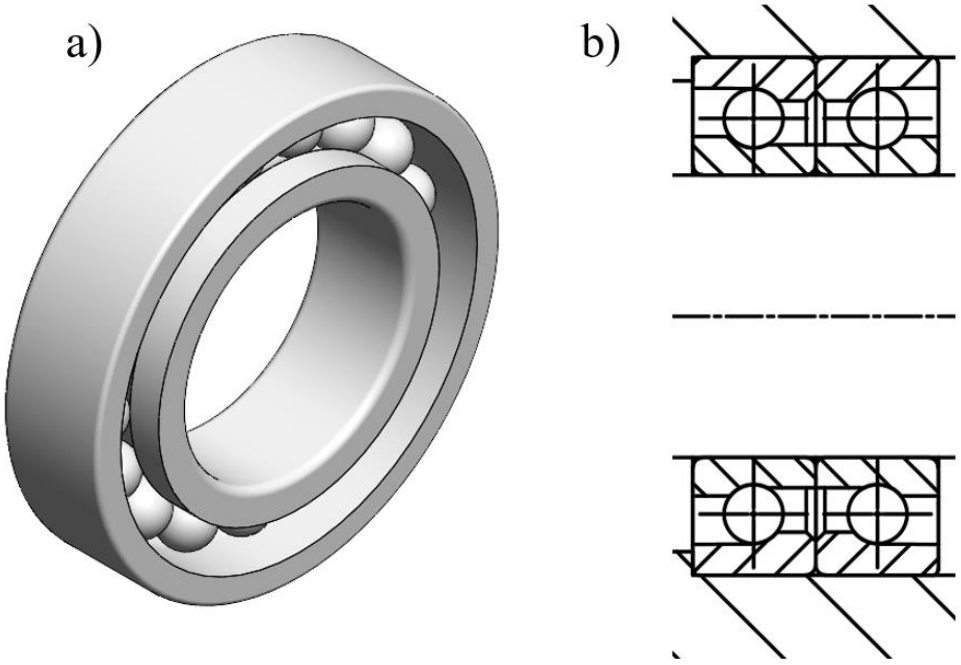

Figure 4.18: (a) CAD model of the ball bearing and (b) The ball bearings are arranged back-to-back.

Using the data provided by the technical specification sheet found in the SKF website, and the load that the ball bearing will suffer, calculations were carried out to determine the bearing service life. Using the harsher conditions (freight wagon), the results are presented in Table 4.7.

Static study			
Static safety factor	S_0	4.1	
Bearing service life			
Life in millions of cycles	L_{10}	261	[millions of cycles]
Life in hours	$L_{10,h}$	2513	[h]
Speed limitations			
With grease lubricant	$n_{max,1}$	31200	[rpm]
With oil-air lubricant	$n_{max,2}$	48000	[rpm]

Table 4.7: Results of the ball bearing analysis.

4.4.2 Structural analysis

In order to design the upper plate, a structural analysis is required. It needs to withstand the whole contact load, therefore a minimum thickness of the component must be determined, as well as its deflection.

Fig. 4.20 shows a schematic of the forces that the upper beam must withstand, where F is the normal contact force in the freight simulation scenario (Table 4.8).

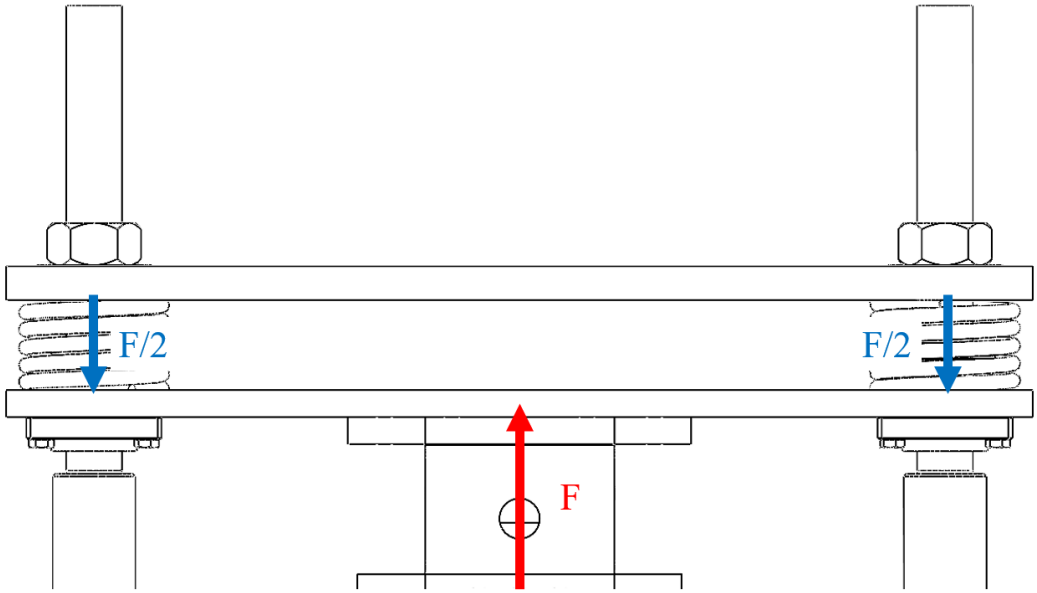

Figure 4.19: schematic of the forces applied to the loading beam.

The maximum stress σ_{max} is situated at the centre of the plate and can be calculated as:

$$\sigma_{max} = \frac{M_{fmax}}{J} \cdot \frac{h}{2} = \frac{F}{2} \cdot \frac{l}{2} \cdot \frac{1}{J} \cdot \frac{h}{2} \tag{4.22}$$

Where J is the moment of inertia, l is the length of the plate and h is its thickness. The moment of inertia is calculated as:

$$J = \frac{b \cdot h^3}{12} \tag{4.23}$$

This value will be compared to a σ_{id}, which depends on the material chosen. For steel, the σ_{id} chosen is the yield strength σ_y=400 MPa. The safety factor is equal to:

$$SF = \frac{\sigma_{id}}{\sigma_{max}} \tag{4.24}$$

Table 4.8 shows the geometry of the plate and the values calculated using Equations (4.22), (4.23), and (4.24).

Parameter		Unit
h	20	[mm]
b	254	[mm]
l	630	[mm]
F	5000	[N]
Moment of inertia	169333	[mm^4]
σ_{max}	46.51	[MPa]
SF	8.6	

Table 4.8: Structural analysis of the plate.

Subsequently, a calculation of the plate's deflection is performed. Although the plate is structurally verified, a deflection that is too high might cause instabilities and pose safety risks. The maximum deflection is located at the centre of the plate, and it can be calculated as:

$$y_{\max} = \frac{F \cdot l^3}{48 \cdot E\,J} \tag{4.25}$$

Where E is the material's Young modulus, which is equal to 210 GPa. The value of the maximum deflection is y_{max} = 0.73 mm, which is considered acceptable as it is less than a millimetre.

4.4.3 Traction rods thread

The nuts used to compress the helical springs need to withstand half of the contact force each. Specifically, using the following equation, the bolt-tightening torque is determined:

$$M_T = \frac{F}{2} \cdot \left(\frac{p}{\pi} + d_m \cdot \frac{tan\varphi}{cos\alpha} + d_t \cdot tan\varphi_s\right) \tag{4.26}$$

Where F is the force acting on the thread, p is the thread pitch, d_m is the average diameter, tan φ is the coefficient of friction between the nut and the screw, tan φ_s is the coefficient of friction between the nut and the loading beam, d_t is the effective diameter, and α is the thread angle, which is equal to 30° for metric threads.

The coefficients of friction are assumed to be equal to 0.2, d_t is assumed as 130% of the nominal diameter and the other parameters are obtained by referring to the appropriate charts. For a M40 thread, it is found that in the case of the newly designed twin disc test bench, the bolt-tightening torque is equal to:

$$M_T = 73.26\ Nm \tag{4.27}$$

4.5 Testing procedure

The configuration of the new twin disc, based on two independently controlled brushless motors, allows to perform different types of tests. By controlling the angular speed of each motor, a constant creepage can be achieved at the contact interface. This kind of control can be adopted to carry out wear tests at different values of creepage, reference speed and normal load, measuring the amount of worn material on the surfaces of the contacting bodies at discrete times with a laser system already available in the laboratories of the research group.

The wear tests will be run to tune the wear coefficient for different operating conditions of real passenger and freight vehicles. Table 4.9 shows the most critical operating conditions that can be reproduced on the newly designed bench considering a nominal friction coefficient of 0.4. The table also provides the values of the main quantities that need to be adjusted on the bench during the test. The values of torque correspond to continuous operations of the two motors, however larger values, corresponding to higher friction coefficient, can be provided in case of short-term overloading conditions.

Disc	Parameter	Passenger M= 12 t/axle, V= 80 km/h	Freight M= 22,5 t/axle, V=60 km/h	Unit
Wheel	Rotational speed	2307	1730	rpm
	Normal load	2354	4415	N
	Nominal Torque	87	162	Nm
Rail	Rotational speed	1608	1206	rpm
	Normal load	2354	4415	N
	Nominal Torque	124	233	Nm

Table 4.9: Parameters of the two disc specimens depending on the operating conditions to be simulated.

More in detail, one of the most widely used approaches to estimate wear in the railway field is the Archard's wear law, which was described in chapter 2. It calculates the amount of worn volume $V_{removed}$ as described in equation (2.1) which is transcribed below:

$$V_{removed} = k_{Arch} \cdot \frac{N \cdot d_s}{H_s} \tag{2.1}$$

where N is the normal load, d_s is the sliding distance, H_s is the Brinell hardness of the softer contacting material and finally k_{Arch} is the wear coefficient. The wear coefficient is typically determined as a function of contact pressure and sliding speed, often derived from experimental maps featuring four distinct wear zones, as shown in Fig. 4.21.

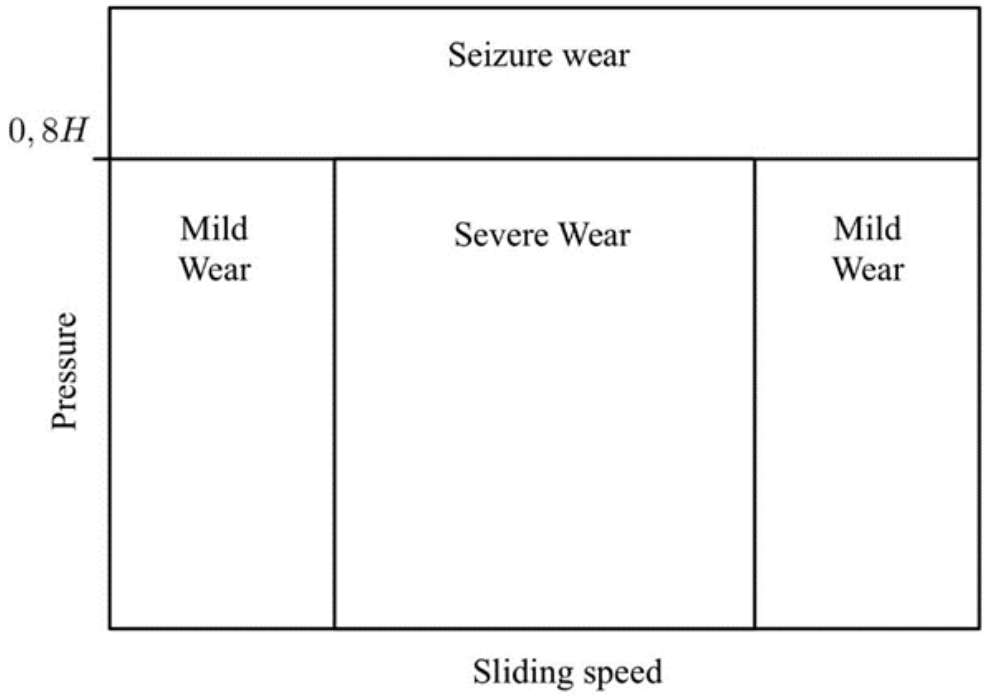

Figure 4.20: Archard wear map.

One of the most utilized maps is derived from research conducted at the Swedish Royal Institute of Technology (KTH). Typically, constant coefficients are assigned to each zone, and their values, as well as the boundaries of each zone, are established based on literature data obtained across various conditions. Therefore, it is believed that the major features of the newly designed bench, namely the use of scaled profiles and the correction of the lateral curvature of the rail disc profile compensating for the introduction of a longitudinal curve radius of the rail, will allow to derive more refined maps from testing conditions that can be easily related to real operations of railway vehicles.

The same control approach as for the wear tests can be also applied to derive experimental adhesion curves, by recording the torque provided by each motor and the speed of both discs in steady-state conditions for different values of creepage and contamination at the contact patch.

On the other hand, a different kind of test can be performed by setting a constant speed for one disc, while progressively increasing the resistant torque on the other roller, thus achieving an increasing creepage. This strategy enables the measurements of adhesion curves in dynamic conditions, whereby the creepage at the contact interface changes quickly until approaching full slip conditions.

During the testing procedure, as the discs suffer wear, the helical springs will extend, and the contact load will gradually decrease. Therefore, a linear potentiometer (PZ34 series), shown in Fig. 4.22, is installed between the upper plate and the loading beam, allowing to accurately measure the load applied by the loading system.

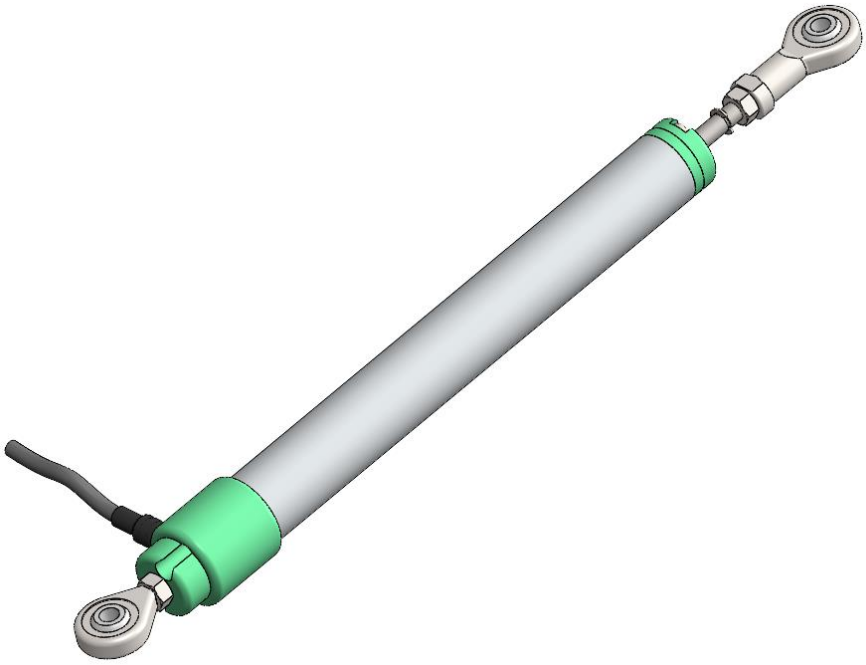

Figure 4.21: CAD model of the PZ34 series potentiometer.

To account for the minimal distance between the plate and the beam, two additional small plates are specifically machined. The installed potentiometer is shown in Fig. 4.23.

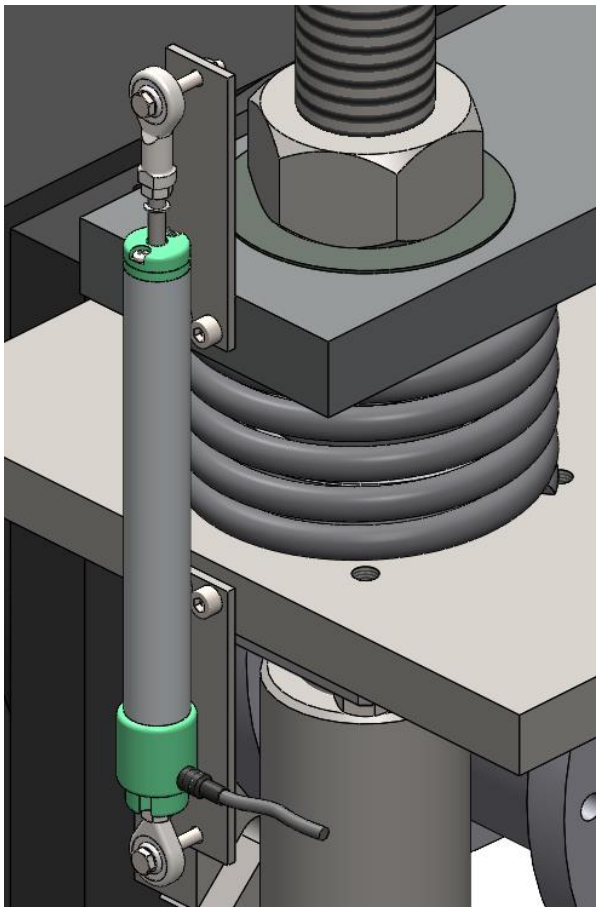

Figure 4.22: CAD of the potentiometer installed on the side of the bench.

To verify the actual normal load acting between the rollers and to calibrate the position transducer (Fig. 4.23), a setup process is defined. Before running the wear tests two special elements, which fit the profiles of the discs, are positioned between them, as shown in Fig. 4.24. These elements allow to install a button load cell between the rollers, thus verifying, from the spring compression, if the applied load corresponds to the desired one, hence estimating possible load loss due to friction. This initial calibration ensures that the desired load can be accurately applied between the discs. It is expected that load loss due to friction is very low since the vertical sliding of the upper plate is guaranteed by a couple of linear bearings, as shown in Fig. 4.13.

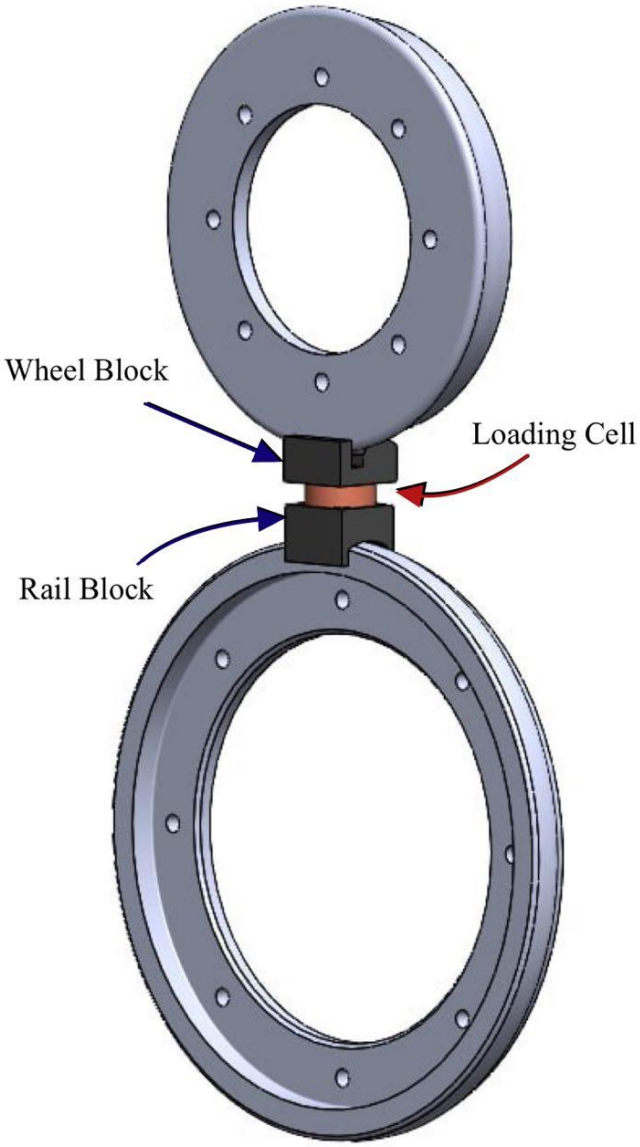

Figure 4.23: Configuration of the wheels during the pre-test load verification.

4.6 Overview of the twin disc tribometer design

This paragraph includes a summary of the main elements of the novel twin disc test bench, in order to show an overview of its design. The CAD model of the newly designed bench is shown in Fig. 4.25.a. The test rig is connected to a rigid frame (1), through a series of bolts. Two steel traction rods (2) connect the upper (3) and lower (4) plates, supporting the load application system and enhancing the overall stiffness of the structure.

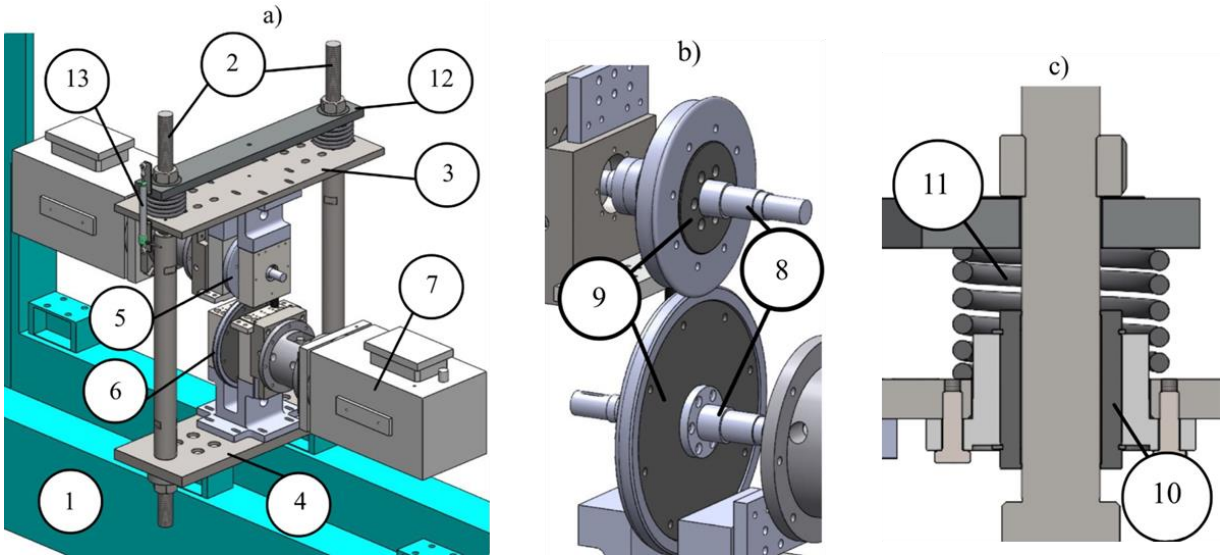

Figure 4.24: (a) CAD model of the novel twin-disc tribometer, (b) detail of the wheel and rail rollers and, (c) detail of the helical spring and linear bearing.

The core of the twin disc tribometer is represented by the disc specimens (5) and (6). Each disc is mechanically connected to a motor assembly comprising a brushless motor (7), a shaft (8), an encoder, joints, and supports. The wheel and rail rollers both include a hub (9), connected to the corresponding shaft, and an outer rim machined to the desired scaled wheel/rail profile. This strategy allows to only replace the rim after severe wear and to test different combinations of wheel and rail materials/profiles, thus allowing to reduce the setup costs. The supports of both motors are connected to the two plates (3) and (4), on which specifically designed slotted holes are machined in order to adjust the relative position between the contacting discs. As shown in Fig. 4.25.c, the upper plate (3) is guided in vertical direction by linear bearings (10), which slide on the vertical traction rods (2) connecting the two plates. The linear bearings are fundamental to avoid a loss of vertical load due to friction forces since the applied load must act entirely on the contact patch.

To simulate different axle-load values, the bench includes a system for the application and adjustment of the normal load at the contact interface between the rollers. After exploring different solutions, the choice is for a system based on helical springs (11), which act between the loading beam (12) and the upper plate (3). Compared to rigid loading systems, where the profiles are pressed without elastic elements, the selected solution ensures a limited loss of the contact load when the profiles are worn out. A linear potentiometer (PZ34 series) (13), mounted

between the upper plate and the loading beam, allows to accurately measure the load applied by the loading system.

The creepage between the two discs, subjected to an adjustable normal load, is achieved through a pair of independently controlled motors. More in detail, the angular speed of each disc is controlled by a synchronous permanent magnets motor (brushless) motor ACM BRL 220, providing a maximum torque of 650 Nm and a nominal torque of 150 Nm@2000 rpm. Motors include high resolution digital encoders that are used to measure the rotational speed of each roller.

5.Multibody simulation

In addition to being used to experimentally determine Archard's law coefficients, the twin disc test rig will be used to validate wear algorithms implemented within commercial multibody codes [67]. For this reason, during the design activity, a numerical model of the twin disc test rig was realized in the Simpack environment. The model, shown in Fig. 5.1, includes the roller-rail that is connected to the main bench frame by a rotational degree of freedom (d.o.f). The bench frame is composed by two bodies, i.e. the main frame and the upper frame. The former is modelled as a body with 0 d.o.fs, since it is rigidly connected to the inertial system, while the latter has one d.o.f. in vertical direction with respect to the main frame.

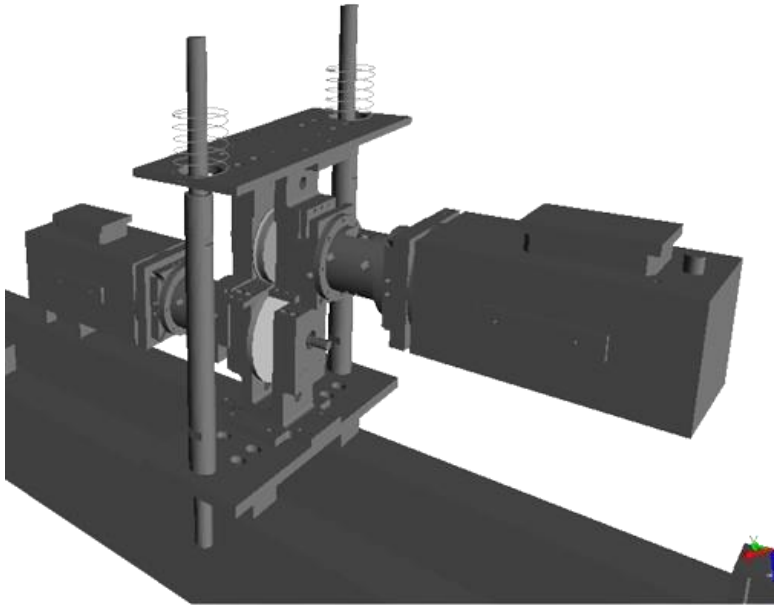

Figure 5.1: Multibody model of the twin-disk test rig realized with the Simpack MB code.

The last body in the model is the wheel roller, which is connected to the upper frame of the bench by means of the Simpack general rail-track joint. A constraint element, based on Lagrange multipliers, is used to only allow the rotational degree of freedom to the wheel-roller. The use of a general rail-track joint is strictly necessary in order to define the contact pair element. The normal force is determined by the equivalent elastic method, while tangential forces are calculated using the FASTSIM algorithm, considering a friction coefficient of 0.4.

The vertical load is realized by means of two point-to-point force elements, acting between the upper frame and the main frame, that simulate the test bench loading system. The speed of the two rollers is controlled by means of Simpack PID control elements, implementing the behaviour of the motor drives used to actuate the rollers. Wheel roller wear is calculated using the Simpack Wheel Profile Wear module, implementing the Archard's wear law. The update of the wheel profile after a predetermined travelled distance is realized by an in-house QtScript routine [68]. The discrete update and post-processing of the worn profiles is indeed the key to improve the numerical stability of the method [69].

Preliminary simulations are performed for a typical operating condition of a European freight wagon running at 60 km/h with axle load of 20 ton (400 kg on the test bench), considering different creep levels (ξ = 1%, 2.5% and 5%). The adopted creep levels correspond to the mild 1, severe and mild 2 regions of the Archard's wear map respectively, see Fig. 4.21. Simulation results are obtained considering literature data for the wear coefficients and Archard wear map, but they are useful to understand the expected wear rate and the evolution of the shape of the wheel profile. In future activities, the wear map used in the simulations will be tuned against experimental data collected from the bench.

For each creepage level, the evolution of the wheel profile is evaluated for a total rolling distance of 80 km (corresponding to 400 km on the full-scale), with profile replacement every 200 m (1 km on the full-scale system), thus performing 400 iterations. Please consider that this simulation distance corresponds to a large amount of travelled distance of a real vehicle, as creepage at the wheel-rail contact is always well below 1%. The results of the simulations are shown in Fig. 5.2, which displays the original, final, and intermediate worn profiles during the simulation for the three tested creepage levels, with zoom on the worn region. For all cases, wear occurs on the tread, whereby the nominal contact point is located. As expected, the largest amount of wear is obtained for creepage value of 2.5% (Fig. 5.2.c), which corresponds to the severe region of the wear map, featuring a larger wear coefficient. The final profile for this value of creepage looks harsh, and this means that the large amount of wear is leading to numerical instabilities, that may be caused by incorrect values of the wear coefficient. Therefore, the results of the numerical simulation confirm that further investigation is needed to obtain proper wear coefficients for the simulated conditions.

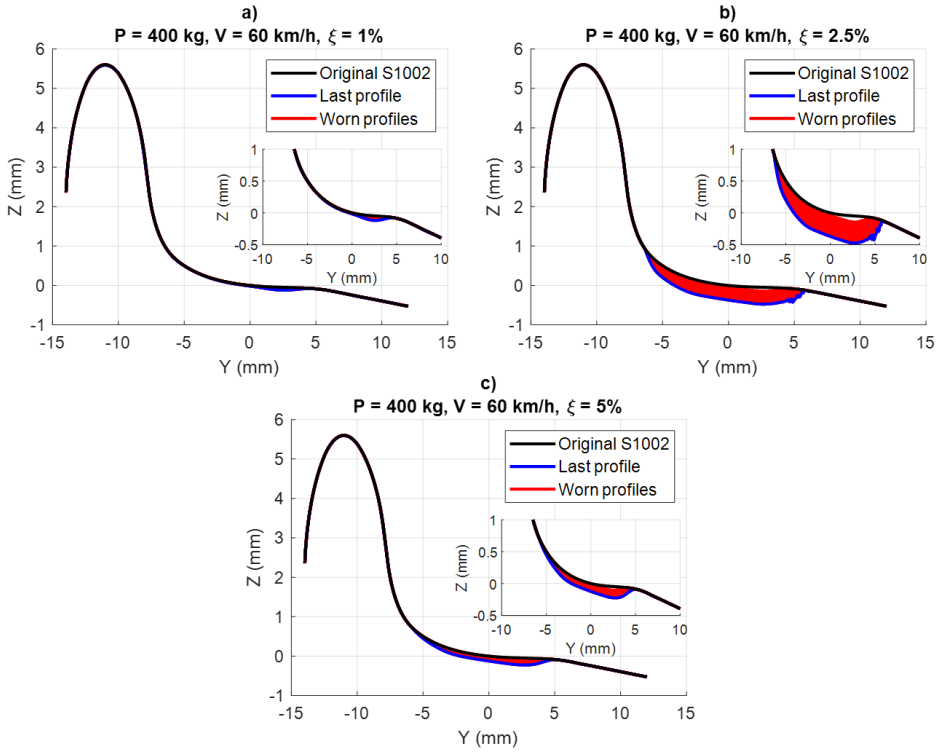

Figure 5.2: Results from the simulations of multibody model. Worn profiles for creepage equal to: (a) ξ=1%, (b) ξ=2.5%, (c) ξ=5%.

6. Future developments

As mentioned in previous chapters, the slotted holes machined in the upper plate (Fig. 4.14.b (3)), allow for the integration of additional components into the twin disc test bench.

After careful consideration, the research team proposed adding a tread braking system to the bench that would allow to execute tests investigating the thermal behaviour induced by the brakes. By installing a support structure using bolts, the upper plate can accommodate the braking system. A prototype of the braking system is illustrated in Fig. 6.1, showcasing a brake positioned on each side of the wheel roller.

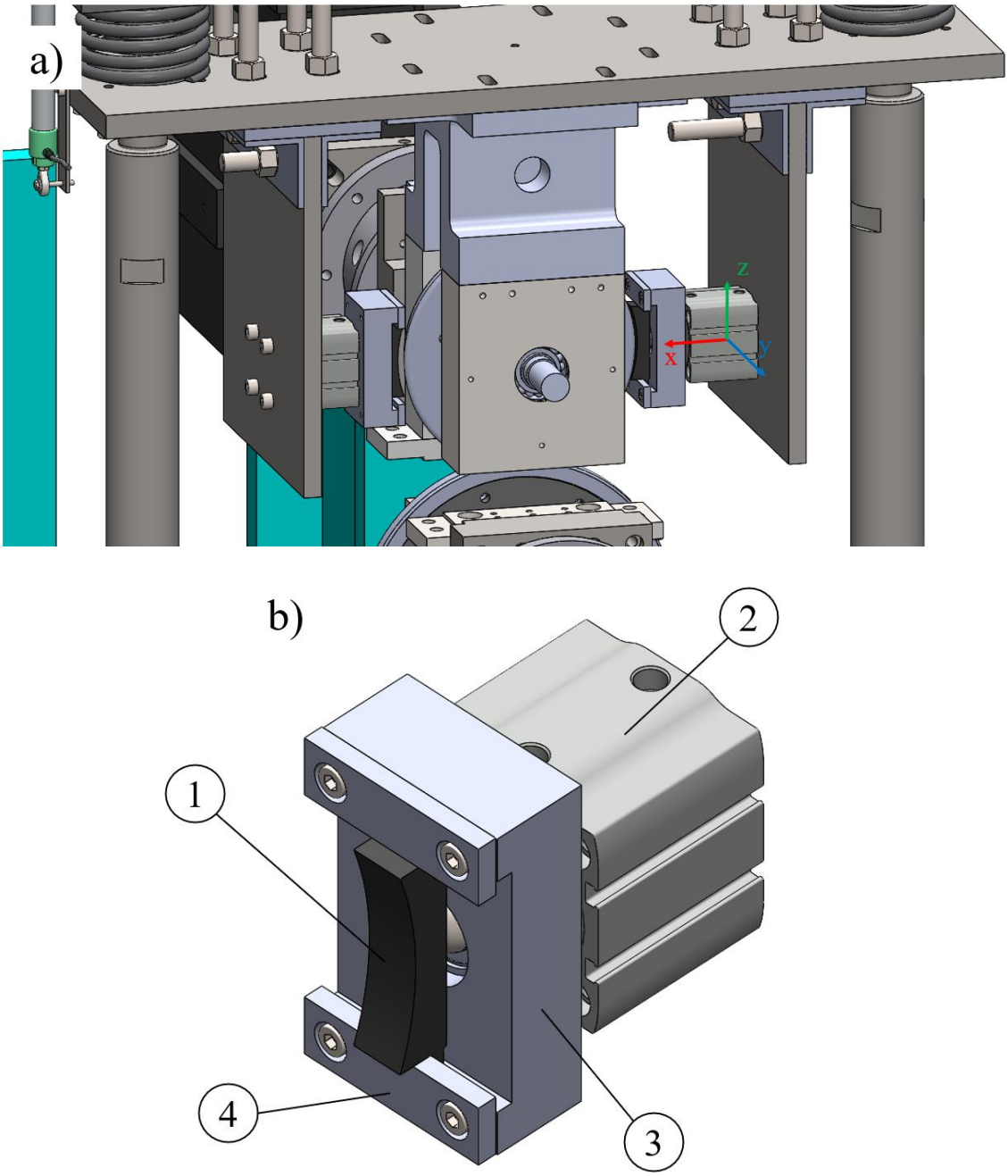

Figure 6.1: The twin disc test bench featuring the possible braking system and (b) Brake prototype that can be potentially added to the test bench.

Referring to Fig. 6.1.b, the cast iron shoe (1) is crafted to closely mimic the geometry of a real railway brake, particularly its curvature. As depicted in Fig. 6.1, the brake is pressed against the wheel disc by a pneumatic piston (2). For this example, a pneumatic piston ADN-S-50-25-I-P-A series was selected. Using the air compressor already available in the laboratory, it is possible to apply a pressure of 0,8 MPa to the cylinder, which in turn will press the brake with a force of F=1570 N against the wheel. Due to the cast iron composition of the shoe, threading a hole and directly attaching it to the piston is not feasible. Instead, the shoe is initially placed in a support component resembling a C-shape (3) and subsequently secured via two smaller plates (4) using screws. Fig. 6.2 illustrates the section of the braking system, highlighting the connection between the piston and the rest of the system.

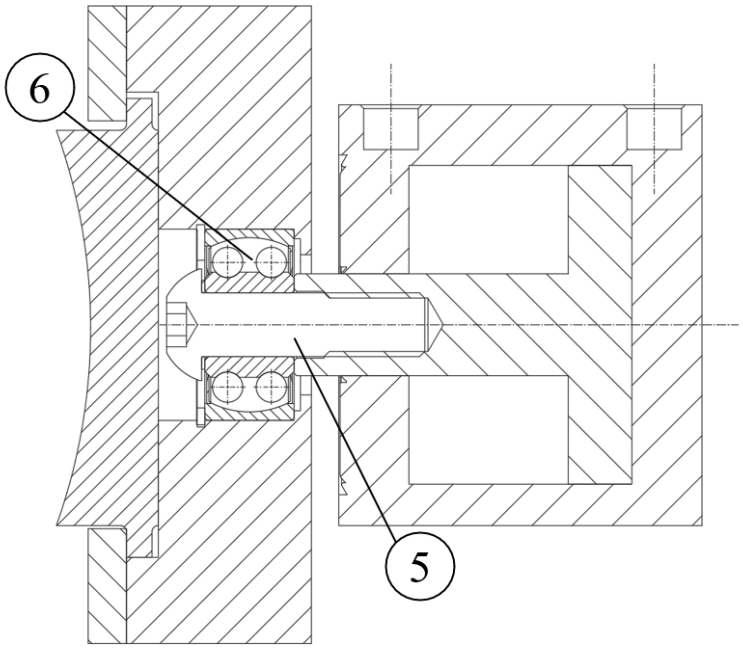

Figure 6.2: Section of the braking system, side view.

A screw (5) inserted into the piston's rod links the actuator to a self-aligning ball bearing (6) of SKF 2200 E-2RS1TN9 series. This bearing, featuring two rows of balls and sealed on both sides, allows for limited rotational mobility of the brake along the y and z axes in the reference system depicted in Fig. 6.1.a. This rotational mobility enables the brake to establish better contact with the wheel as wear of the shoe occurs. As the brake is pressed against the wheel, it suffers wears and, since the contact phenomena in this case is very complex, the material may not be removed homogeneously. Therefore, being able to rotate even slightly, allows the brake to make better contact to the wheel. Rotation along the X axis is prevented, as it is undesirable. Machining the opening to insert the piston rod with a small clearance, as shown in Fig. 6.3, ensures that only rotational movement along this axis is restricted, while allowing movement along the others. Finally, to immobilize the outer ring of the ball bearing, a circlip ring is inserted into the designated housing machined into the brake support.

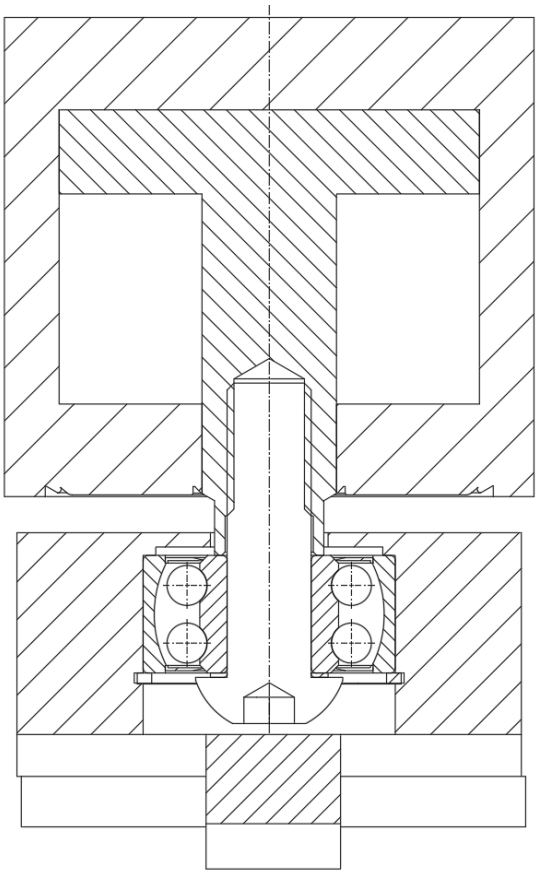

Figure 6.3: Horizontal section of the braking system, top view.

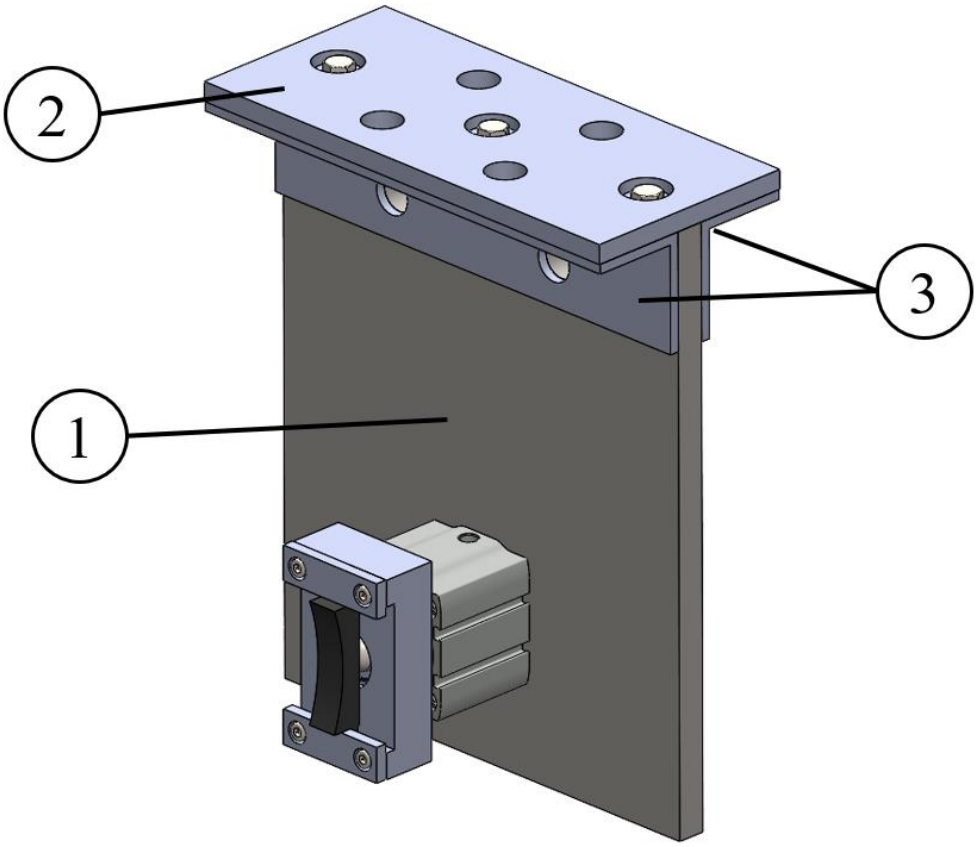

Figure 6.4: CAD model of the braking system including its support.

The braking system, including its support that links it to the main test bench is shown in Fig. 6.4. This is a simple system that includes a vertical plate (1) that supports the braking system, a horizontal plate (2) that is placed directly under the upper plate of the test rig, and two L-beams (3) which are used increase the rigidity of the structure. As the brake presses against the wheel, the force it receives must be transferred via these components to the main bench, for this reason, it is crucial to have a rigid constraint.

Three screws are inserted in the holes of the horizontal plate, which are used to connect it to the vertical plate, which has three threaded holes, as shown in the blueprints in Annex B. To install the system on the slotted holes of the upper plate, four bolts are inserted vertically through the horizontal plate and the L-beams. Afterwards, two horizontal bolts are used to connect the L-beams to the vertical plate. Finally, the pneumatic cylinder is mounted on the vertical plate using four screws, which pass through dedicated slotted holes on the vertical plate, as shown in Fig. 6.5. The presence of slotted holes on both the upper plate and the vertical plate grants greater freedom in positioning the braking system, addressing possible inaccuracies caused by the manufacturing of the components.

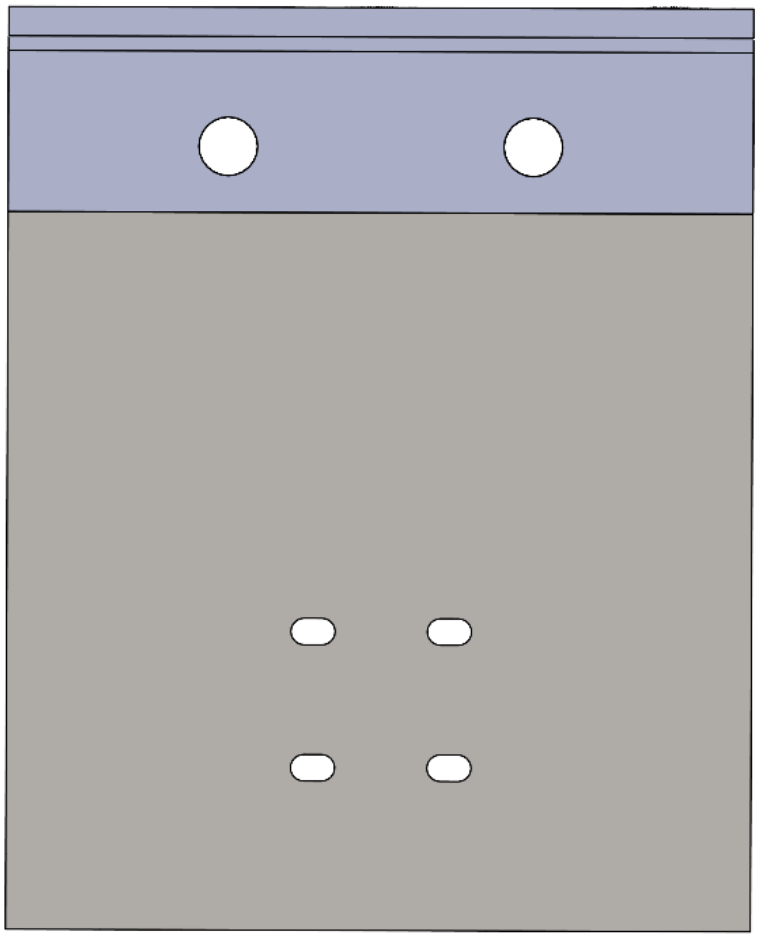

Figure 6.5: Front view of the support for the braking system.

7. Conclusions

After reviewing various tribometers from the literature and highlighting their key characteristics, this thesis presents an innovative design for a twin disc test rig for railway applications. A common limitation observed among these test rigs is the use of disc specimens that fail to accurately replicate the profiles of real wheels and rails. The proposed twin disc tribometer addresses this limitation by using discs with lateral profiles closely resembling those used in real applications, considering the standards ORE S1002 for the wheel and UIC 60 for the rail. Furthermore, the lateral curvature of the rail disc is slightly adjusted so as to replicate the same contact pressure for a set axle load, using Pascal's similitude model.

The main characteristics of a twin disc tribometer are the normal force and the slippage between the discs. The first one is achieved via compression springs, a cost-effective solution that allows to keep constant contact pressure. Creep between the discs can be easily obtained by powering each shaft with an independent AC motor.

The rig is designed to simulate the conditions of heavily loaded European fright wagons, namely withstanding an axle-load of 22.5t and a speed of 60 km/h, but it can also replicate operating conditions of passenger vehicles. Therefore, the rig is able to simulate a vast array of real contact conditions. The bench will be used to perform wear test campaigns, by independently controlling the speed of both shafts to achieve desired creepage values. The experimental results will drive the definition of more refined wear maps, based on the measurements performed on the bench, that include the measurement of the worn profiles through a laser scanner system already available in the lab.

The twin disc bench will be used to validate wear algorithms currently adopted in commercial multibody codes. For this reason, a detailed multibody model of the test bench is realized in Simpack environment. The model is used to obtain preliminary worn profiles of the wheel roller.

Future work regarding the test rig includes designing and adding a tread braking system with scaled shoes to the tribometer. These will be used to brake the wheel disc, so that the bench will enable the execution of tests to investigate the wear and thermal behaviour caused by tread braking operations as well.

8.References

[1] Dearden J. The wear of steel rails and tyres in railway service. Wear 1960; 3: 43–49.

[2] Olofsson U and Telliskivi T. Wear, friction and plastic deformation of two rail steels full scale test and laboratory study. Wear 2003; 254: 80–93.

[3] Olofsson U and Nilsson R. Surface cracks and wear of rail: a full-scale test on a commuter train track. Proc IMechE, Part F: J Rail and Rapid Transit 2003; 216: 249–264.

[4] Harmon, M.; Santa, J.F.; Jaramillo, J.A.; Toro, A.; Beagles, A.; Lewis, R. Evaluation of the coefficient of friction of rail in the field and laboratory using several devices. Tribol. Mater. Surf. Interfaces 2020, 14, 119–129.

[5] McEwan I, Harvey R (1985) Full scale wheel on rail testing: comparisons with service wear and developing a theoretical predictive model. Lub Eng 41 (2):80-88

[6] Stock R, Eadie DT, Elvidge D, Oldknow K (2011) Influencing rolling contact fatigue through top of rail friction modifier application – A full scale wheel–rail test rig study. Wear 271 (1):134-142. https://doi.org/10.1016/j.wear.2010.10.006

[7] Stock R, Pippan R (2011) RCF and wear in theory and practice—The influence of rail grade on wear and RCF. Wear 271 (1):125-133. https://doi.org/10.1016/j.wear.2010.10.015

[8] Sundh J, Olofsson U (2011) Relating contact temperature and wear transitions in a wheel–rail contact. Wear 271 (1):78-85. https://doi.org/10.1016/j.wear.2010.10.046

[9] Sundh J, Olofsson U, Sundvall K (2008) Seizure and wear rate testing of wheel–rail contacts under lubricated conditions using pin-on-disc methodology. Wear 265 (9):1425-1430. https://doi.org/10.1016/j.wear.2008.03.025

[10] Lyu Y, Zhu Y, Olofsson U (2015) Wear between wheel and rail: A pin-on-disc study of environmental conditions and iron oxides. Wear 328-329:277-285. https://doi.org/10.1016/j.wear.2015.02.057

[11] Lewis SR, Lewis R, Olofsson U, Eadie DT, Cotter J, Lu X (2013) Effect of humidity, temperature and railhead contamination on the performance of friction modifiers: Pin-on-disk study. Proceedings of the Institution of Mechanical Engineers, Part F: Journal of Rail and Rapid Transit 227 (2):115-127. 10.1177/0954409712452239

[12] Liu HC, Zhang BB, Bader N, Venner CH, Poll G (2021) Scale and contact geometry effects on friction in thermal EHL: twin-disc versus ball-on-disc. Tribology International 154:106694. https://doi.org/10.1016/j.triboint.2020.106694

[13] Björling M, Habchi W, Bair S, Larsson R, Marklund P (2013) Towards the true prediction of EHL friction. Tribology International 66:19-26. https://doi.org/10.1016/j.triboint.2013.04.008

[14] Ciulli E (2013) Thermal effects of different kind influencing lubricated non-conformal contacts. Tribology International 59:181-189. https://doi.org/10.1016/j.triboint.2012.05.007

[15] Fantecelle Strey N, Bavaresco Rezende A, da Silva Miranda R, Tamara da Fonseca S, Mei PR, Scandian C (2021) Comparison of rolling contact fatigue damage between railway wheels and twin-disc test specimens. Tribology International 160:107037. https://doi.org/10.1016/j.triboint.2021.107037

[16] Megna G, Bracciali A, Mandal NK (2023) Design, wheel-rail interaction and testing of an innovative reinforced smooth transition insulated rail joint. Wear 530-531:205038. https://doi.org/10.1016/j.wear.2023.205038Z

[17] Megna G, Bracciali A (2022) Smooth transition insulated rail joints. Paper presented at the 12th International Conference on Contact Mechanics and Wear of Rail/Wheel Systems, Melbourne (Australia), 4-7 September

[18] Bosso N, Magelli M, Zampieri N (2021) Investigation of adhesion recovery phenomenon using a scaled roller-rig. Vehicle System Dynamics 59 (2):295-312. 10.1080/00423114.2019.1677922

[19] Bosso N, Gugliotta A, Magelli M, Oresta IF, Zampieri N Study of wheel-rail adhesion during braking maneuvers. In, 2019/01/01/ 2019. pp 680-691. 10.1016/j.prostr.2020.02.060

[20] Kato K. Classification of wear mechanisms/models. Proceedings of the Institution of Mechanical Engineers, Part J: Journal of Engineering Tribology. 2002;216(6):349-355. doi:10.1243/135065002762355280

[21] Olofsson, U., and Lyu, Y. (November 14, 2017). "Open System Tribology in the Wheel–Rail Contact—A Literature Review." ASME. Appl. Mech. Rev. November 2017; 69(6): 060803. https://doi.org/10.1115/1.4038229

[22] Hiensch, Martin & Burgelman, Nico & Hoeding, Wouter & Linders, Mark & Steenbergen, Michaël & Zoeteman, Arjen. (2018). Enhancing rail infra durability through freight bogie design. Vehicle System Dynamics. 1-20. 10.1080/00423114.2017.1421766.

[23] Archard, J.F., Contact and Rubbing of Flat Surfaces. Journal of Applied Physics, 24(8), pp. 981-988, 1953. https://doi.org/10.1063/1.1721448.

[24] R. Lewis e R. Dwyer-Joyce, «Wear mechanisms and transitions in railway wheel,» Proc. Instn Mech. Engrs Part J: J. Engineering Tribology, vol. 218, 2004. https://doi.org/10.1243/1350650042794815

[25] Archard JF (1953) Contact and Rubbing of Flat Surfaces. Journal of Applied Physics 24 (8):981-988. 10.1063/1.1721448

[26] Krause H, Poll G (1986) Wear of wheel-rail surfaces. Wear 113 (1):103-122. 10.1016/0043-1648(86)90060-8

[27] Zobory I (1997) Prediction of Wheel/Rail Profile Wear. Vehicle System Dynamics 28 (2-3):221-259. 10.1080/00423119708969355

[28] McEwen IJ, Harvey RF (1986) Interpretation of Wheel/Rail Wear Numbers. Railway Technical Centre, Derby (UK)

[29] Lewis R, Braghin F, Ward A, Bruni S, Dwyer-Joyce R, Bel Knani K, Bologna P (2003) Integrating dynamics and wear modelling to predict railway wheel profile evolution. Paper presented at the 6th International Conference on Contact Mechanics and Wear of Rail/Wheel Systems: CM2003, Gothenburg (Sweden), 10-13 June 2003

[30] Jendel T (2002) Prediction of wheel profile wear—comparisons with field measurements. Wear 253 (1):89-99. 10.1016/S0043-1648(02)00087-X

[31] R. Enblom and M. Berg, "Simulation of railway wheel profile development due to wear influence of disc braking and contact environment," Wear, vol. 258, no. 7-8, pp. 1055–1063, 2005.

[32] Bosso N, Zampieri N (2014) Experimental and Numerical Simulation of Wheel-Rail Adhesion and Wear Using a Scaled Roller Rig and a Real-Time Contact Code. Shock and Vibration 2014. 10.1155/2014/385018

[33] Lewis, R., Dwyer-Joyce, R.S., Olofsson, U., Pombo, J., Ambrósio, J., Pereira, M., et al., Mapping railway wheel material wear mechanisms and transitions. Proceedings of the Institution of Mechanical Engineers, Part F: Journal of Rail and Rapid Transit, 224(3), pp. 125-137, 2010. https://doi.org/10.1243/09544097jrrt328.

[34] Zhu, Y., Wang, W.-J., Lewis, R. et al. (3 more authors) (2019) A review on wear between railway wheels and rails under environmental conditions. Journal of Tribology, 141 (12). 120801. ISSN 0742-4787

[35] Allen, P., Zhang, W., Liang, Y., Zeng, J., Jung, H., Meli, E., et al., Roller Rigs. Handbook of Railway Vehicle Dynamics, ed. S. Iwnicki, M. Spiryagin, C. Cole, T. McSweeney, CRC Press: Boca Raton (FL, USA), pp. 761-823, 2019.

[36] Zhang, W., Chen, J., Wu, X. & Jin, X., Wheel/rail adhesion and analysis by using full scale roller rig. Wear, 253(1), pp. 82-88, 2002. https://doi.org/10.1016/S0043-1648(02)00086-8.

[37] Stolarski, T.A., Friction in a pin-on-disc configuration. Mechanism and Machine Theory, 24(5), pp. 373-381, 1989. https://doi.org/10.1016/0094-114X(89)90067-0.

[38] Abbasi, S., Olofsson, U., Zhu, Y. & Sellgren, U., Pin-on-disc study of the effects of railway friction modifiers on airborne wear particles from wheel–rail contacts. Tribology International, 60, pp. 136-139, 2013. https://doi.org/10.1016/j.triboint.2012.11.013.

[39] Cann, P.M., The "leaves on the line" problem—a study of leaf residue film formation and lubricity under laboratory test conditions. Tribology Letters, 24(2), pp. 151-158, 2006. https://doi.org/10.1007/s11249-006-9152-2.

[40] Development of numerical and experimental tools for the simulation of train braking operations / Magelli, Matteo. - (2023 Apr 20), pp. 1-249.

[41] Zhu, Y., Olofsson, U. & Persson, K., Investigation of factors influencing wheel–rail adhesion using a mini-traction machine. Wear, 292-293, pp. 218-231, 2012. https://doi.org/10.1016/j.wear.2012.05.006.

[42] Bosso N, Allen P, Zampieri N (2019) Scale Testing Theory and Approaches. In: Iwnicki S, Spiryagin M, Cole C, McSweeney T (eds) Handbook of Railway Vehicle Dynamics. Second Edition edn. CRC Press, Boca Raton (FL, USA), pp 825-867

[43] B. Liang, S. Iwnicki, A. Ball, A.E. Young, Adaptive noise cancelling and time-frequency techniques for rail surface defect detection, Mechanical Systems and Signal Processing, 54, 41–51, 2015.

[44] Jaschinski, A., Chollet, H., Iwnicki, S., Wickens, A. & Von Würzen, J., The application of roller rigs to railway vehicle dynamics. Vehicle System Dynamics, 31(5-6), pp. 345-392, 1999. https://doi.org/10.1076/vesd.31.5.345.8360

[45] N. Bosso, A. Gugliotta, A. Somà, Dynamic identification of a 1:5 scaled railway bogie on roller rig, WIT Transactions on the Built Environment, 88, 829–838, 2006.

[46] N. Bosso, A. Gugliotta, A. Somà, Design and simulation of railway vehicles braking operation using a scaled roller-rig, WIT Transactions on the Built Environment, 88, 869–883, 2006

[47] N. Bosso, A. Gugliotta, A. Somà, Simulation of narrow gauge railway vehicles and experimental validation by mean of scaled tests on roller rig, Meccanica, 43(2), 211–223, 2008.

[48] N. Bosso, A. Gugliotta, N. Zampieri, Study of adhesion and evaluation of the friction forces using a scaled roller-rig, Proceedings 5th World Tribology Congress, 8–13 September 2013, Politecnico di Torino (DIMEAS), Torino, Italy, 2640–2643, 2014.

[49] N. Bosso, A. Gugliotta, N. Zampieri, A test rig for multi-wheelset adhesion experiments, In J. Pombo (Ed.), Proceedings 3rd International Conference on Railway Technology: Research, Development and Maintenance, Civil-Comp Proceedings, 110, 223, 2016.

[50] White B, Lee ZS, Lewis R. Towards a Standard Approach for the Twin Disc Testing of Top-Of Rail Friction Management Products. Lubricants. 2022; 10(6):124. https://doi.org/10.3390/lubricants10060124

[51] Rocha, R.C., Ewald, H., Rezende, A.B. et al. Using twin disc for applications in the railway: a systematic review. J Braz. Soc. Mech. Sci. Eng. 45, 191 (2023). https://doi.org/10.1007/s40430-023-04104-1

[52] D.I. Fletcher, J.H. Beynon, Development of a machine for closely controlled rolling contact fatigue and wear testing, J. Test. Eval. 28 (2000) 267–275, https://doi.org/10.1520/JTE12104J.

[53] W.J. Wang, S.R. Lewis, R. Lewis, A. Beagles, C.G. He, Q.Y. Liu, The role of slip ratio in rolling contact fatigue of rail materials under wet conditions, Wear, Volumes 376–377, Part B, 2017, Pages 1892-1900, ISSN 0043-1648, https://doi.org/10.1016/j.wear.2016.12.049.

[54] Harmon M, Santa JF, Jaramillo JA, Toro A, Beagles A, Lewis R (2020) Evaluation of the coefficient of friction of rail in the field and laboratory using several devices. Tribology - Materials, Surfaces & Interfaces 14 (2):119-129. 10.1080/17515831.2020.1712111

[55] Lewis SR, Lewis R, Evans G, Buckley-Johnstone LE (2014) Assessment of railway curve lubricant performance using a twin-disc tester. Wear 314 (1):205-212. https://doi.org/10.1016/j.wear.2013.11.033

[56] Al-Maliki H, Meierhofer A, Trummer G, Lewis R, Six K (2021) A new approach for modelling mild and severe wear in wheel-rail contacts. Wear 476:203761. https://doi.org/10.1016/j.wear.2021.203761

[57] Gallardo-Hernandez EA, Lewis R, Dwyer-Joyce RS (2006) Temperature in a twin-disc wheel/rail contact simulation. Tribology International 39 (12):1653-1663. https://doi.org/10.1016/j.triboint.2006.01.028

[58] O. Arias-Cuevas, Z. Li, R. Lewis, E.A. Gallardo-Hernández, Rolling–sliding laboratory tests of friction modifiers in dry and wet wheel–rail contacts, Wear, Volume 268, Issues 3–4, 2010, Pages 543-551, ISSN 0043-1648, https://doi.org/10.1016/j.wear.2009.09.015.

[59] Oscar Arias-Cuevas, Zili Li, Roger Lewis, A laboratory investigation on the influence of the particle size and slip during sanding on the adhesion and wear in the wheel–rail contact, Wear, Volume 271, Issues 1–2, 2011, Pages 14-24, ISSN 0043-1648, https://doi.org/10.1016/j.wear.2010.10.050.

[60] Hu Y, Wang WJ, Watson M, Six K, Al-Maliki H, Meierhofer A, Lewis R (2023) Wear of driving versus driven discs in a twin disc rolling-sliding test. Wear 512-513:204528. https://doi.org/10.1016/j.wear.2022.204528

[61] Zhao XJ, Guo J, Liu QY, Butini E, Marini L, Meli E, Rindi A, Wang WJ (2018) Effect of spherical dents on microstructure evolution and rolling contact fatigue of wheel/rail materials. Tribology International 127:520-532. https://doi.org/10.1016/j.triboint.2018.07.001

[62] Gutsulyak DV, Stanlake LJE, Qi H (2021) Twin disc evaluation of third body materials in the wheel/rail interface. Tribology - Materials, Surfaces & Interfaces 15 (2):115-126. 10.1080/17515831.2020.1829878

[63] Nathan Fantecelle Strey, Andrei Bavaresco Rezende, Rodrigo da Silva Miranda, Solange Tamara da Fonseca, Paulo Roberto Mei, Cherlio Scandian, Comparison of rolling contact fatigue damage between railway wheels and twin-disc test specimens, Tribology International, Volume 160, 2021, 107037, ISSN 0301-679X, https://doi.org/10.1016/j.triboint.2021.107037.

[64] [1] Regulation (EU) 1315/2013 of the European Parliament and of the Council of 11 December 2013 on Union guidelines for the development of the

trans-European transport network and repealing Decision 661/2010/EU. In: Official Journal of the European Union L 348/1, 20.12.2013.

[65] Bosso N, Gugliotta A, Magelli M, Zampieri N (2019) Experimental Setup of an Innovative Multi-Axle Roller Rig for the Investigation of the Adhesion Recovery Phenomenon. Experimental Techniques 43 (6):695-706. 10.1007/s40799-019-00327-x

[66] Bosso N, Gugliotta A, Zampieri N (2015) Strategies to simulate wheel-rail adhesion in degraded conditions using a roller-rig. Vehicle System Dynamics 53 (5):619-634. 10.1080/00423114.2014.981194

[67] Bosso N, Magelli M, Zampieri N (2022) Simulation of wheel and rail profile wear: a review of numerical models. Railway Engineering Science 30 (4):403-436. 10.1007/s40534-022-00279-w

[68] Bosso N, Zampieri N (2020) Numerical stability of co-simulation approaches to evaluate wheel profile evolution due to wear. International Journal of Rail Transportation 8 (2):159-179. 10.1080/23248378.2019.1672588

[69] Bezin Y, Sambo B, Magalhaes H, Kik W, Megna G, Costa JN (2023) Challenges and methodology for pre-processing measured and new rail profiles to efficiently simulate wheel-rail interaction in switches and crossings. Vehicle System Dynamics 61 (3):799-820. 10.1080/00423114.2021.2014897

Annex A: Blueprints of the test bench

Throughout the dissertation, numerous components were custom designed for the twin disc machine. This annex consists of engineering drawings meticulously detailing all the geometric features of these newly designed components. These drawings serve as comprehensive guides for manufacturers to accurately produce the components. Fig. 4.25 is brought back below.

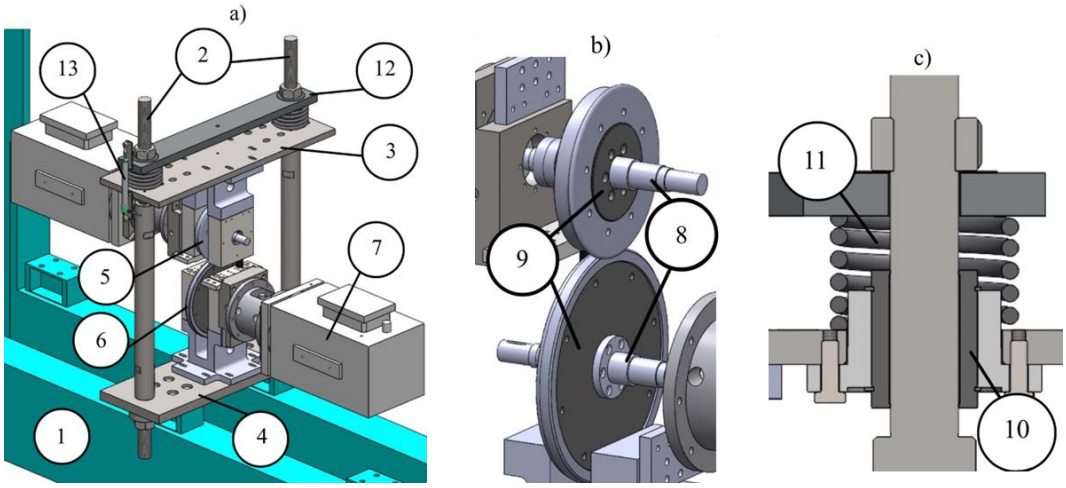

Figure 1A: (a) CAD model of the novel twin-disc tribometer, (b) detail of the wheel and rail rollers and, (c) detail of the helical spring and linear bearing.

Fig. 1A.a (2): Traction rods

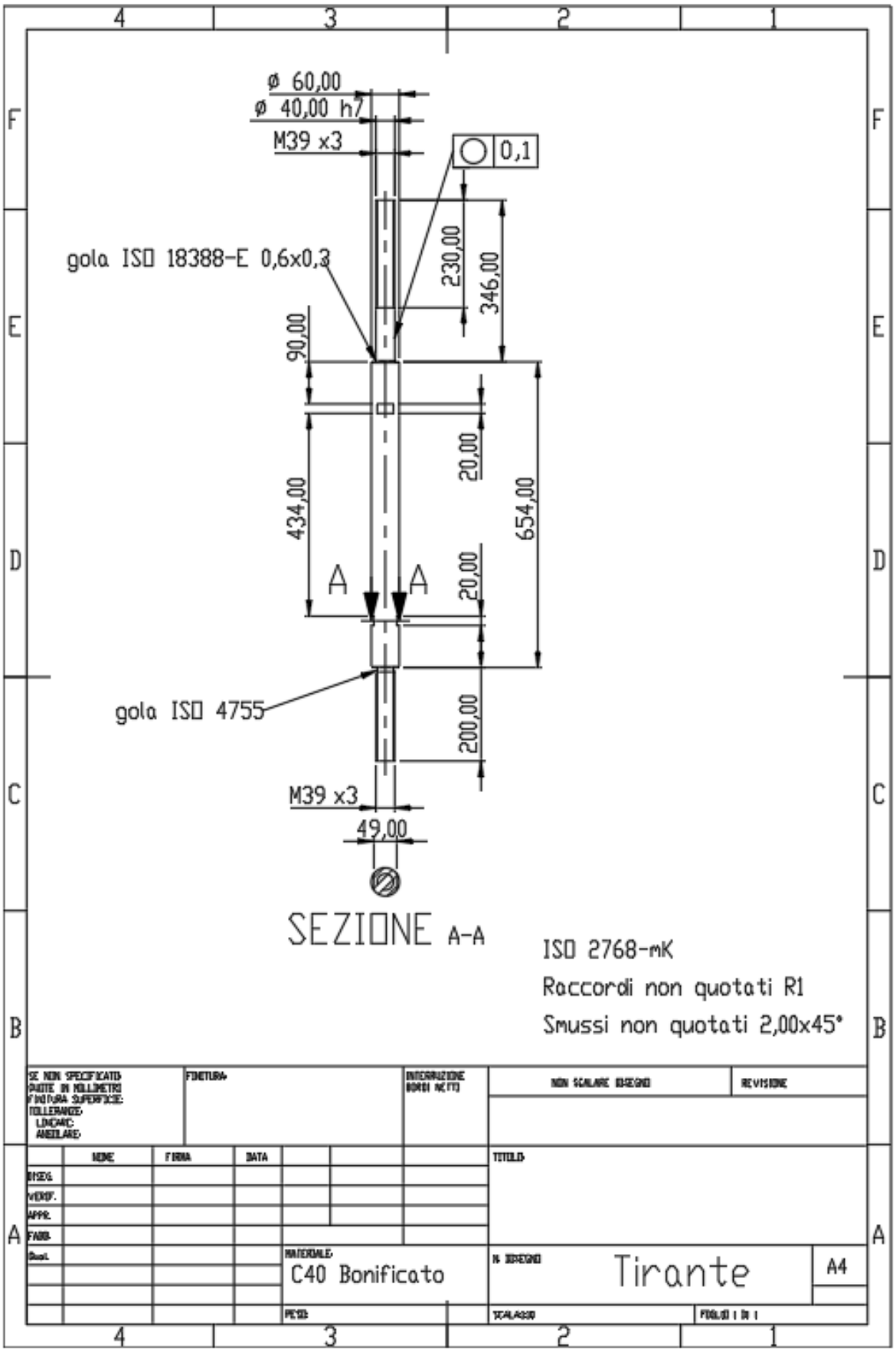

Fig. 1A.a (3): upper plate

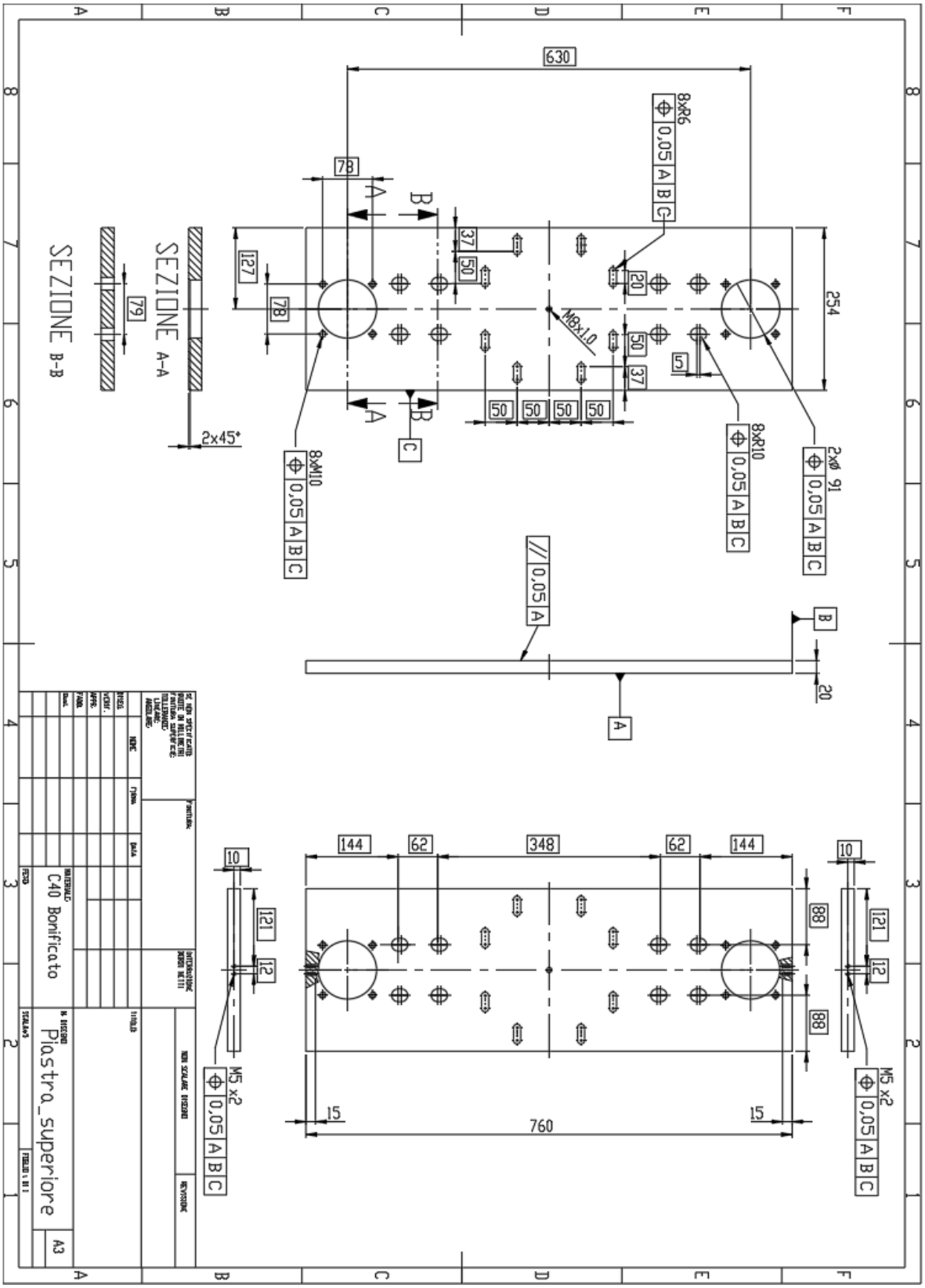

Fig. 1A.a (4): base plate

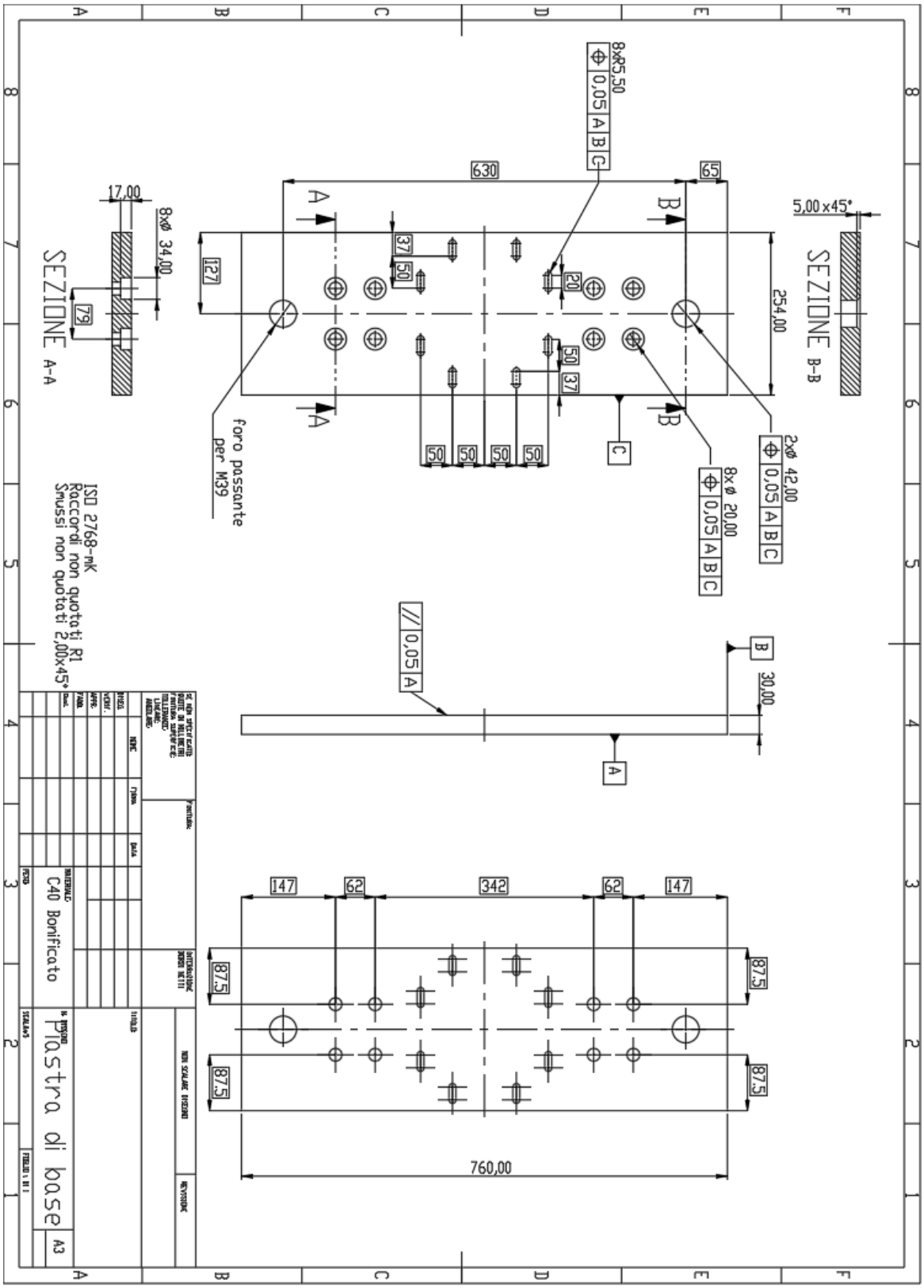

Fig. 1A.a (5): Wheel roller

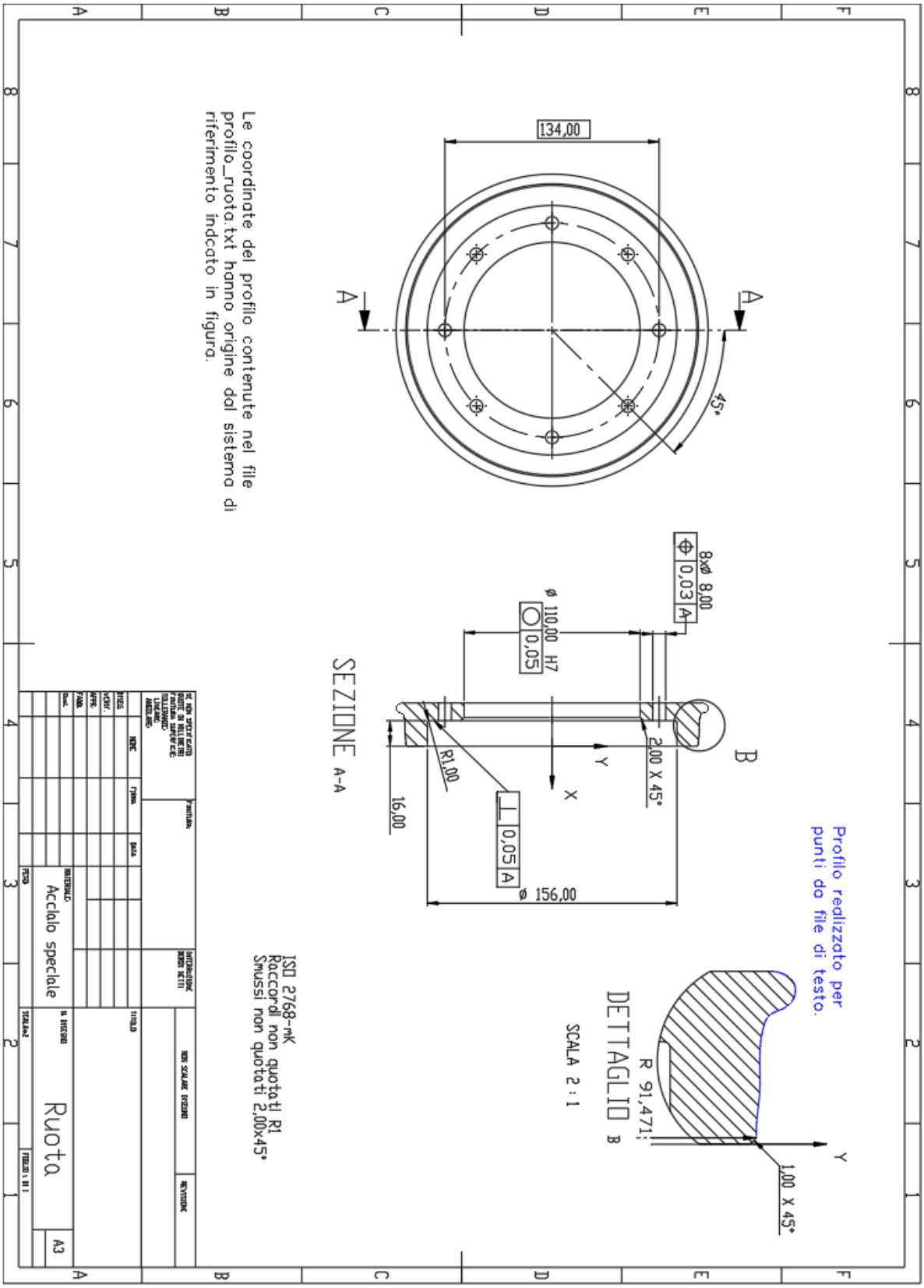

Fig. 1A.a (6): rail roller

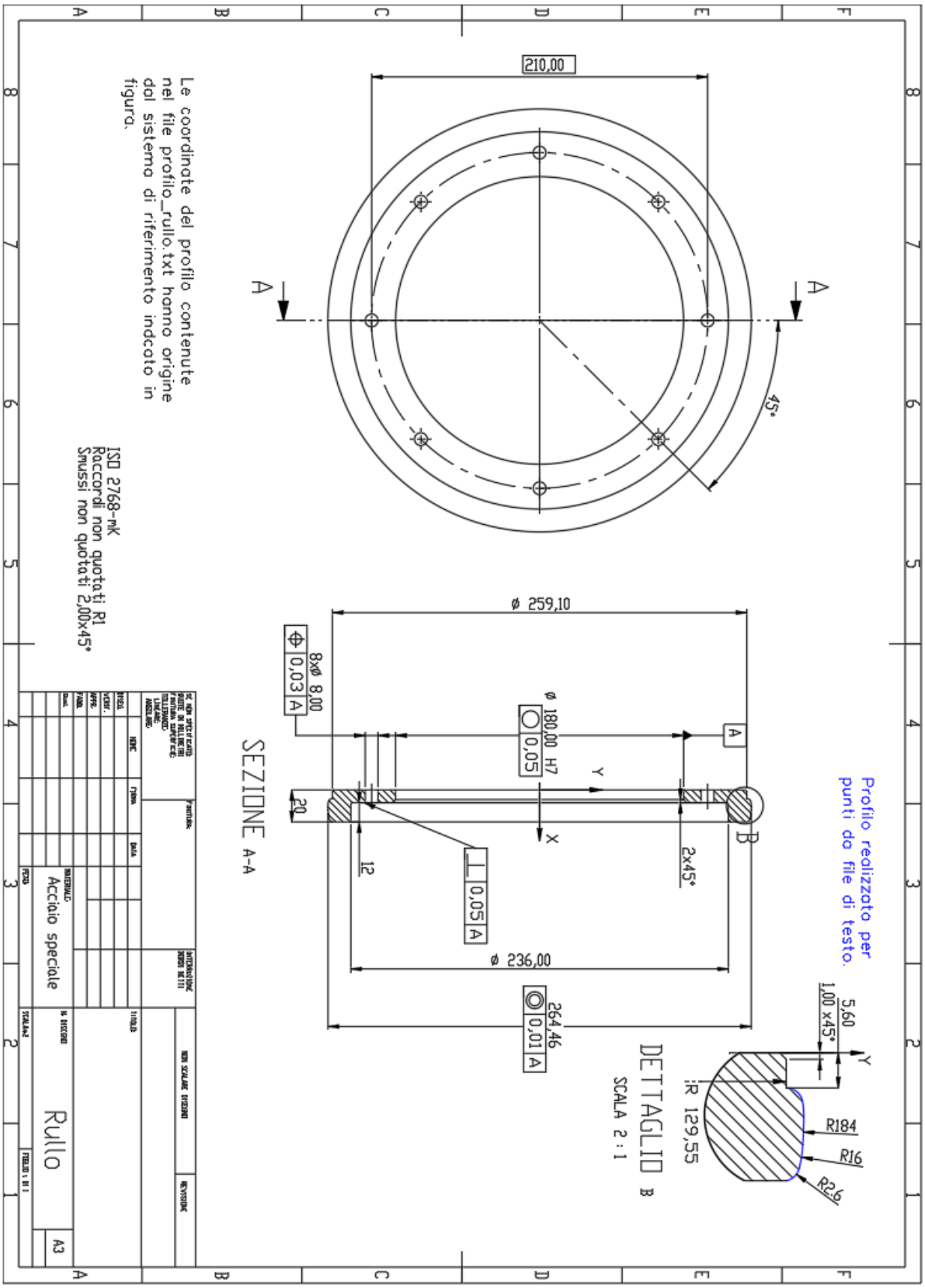

Fig. 1A.b (9): wheel hub

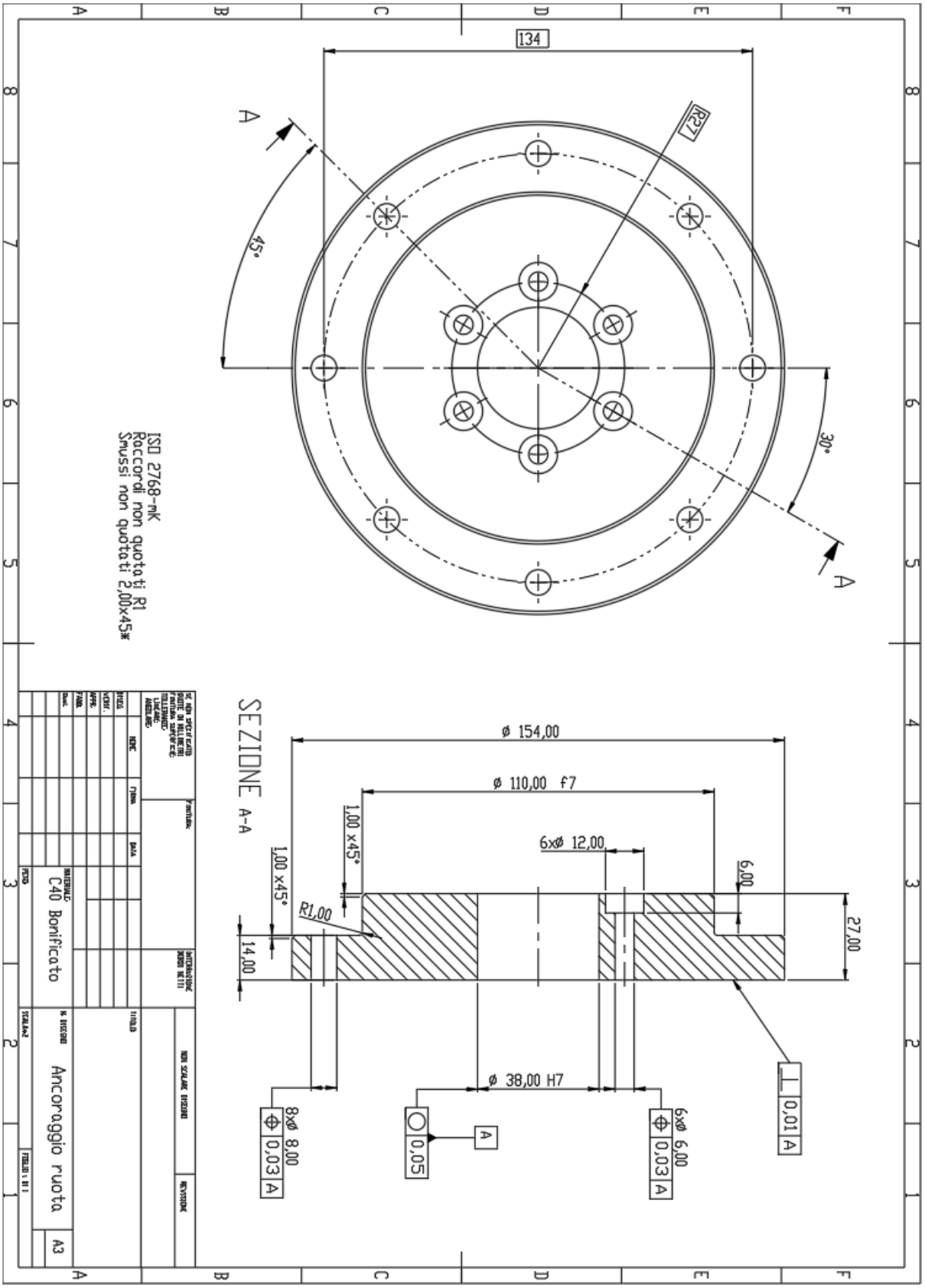

Fig. 1A.b (9): rail hub

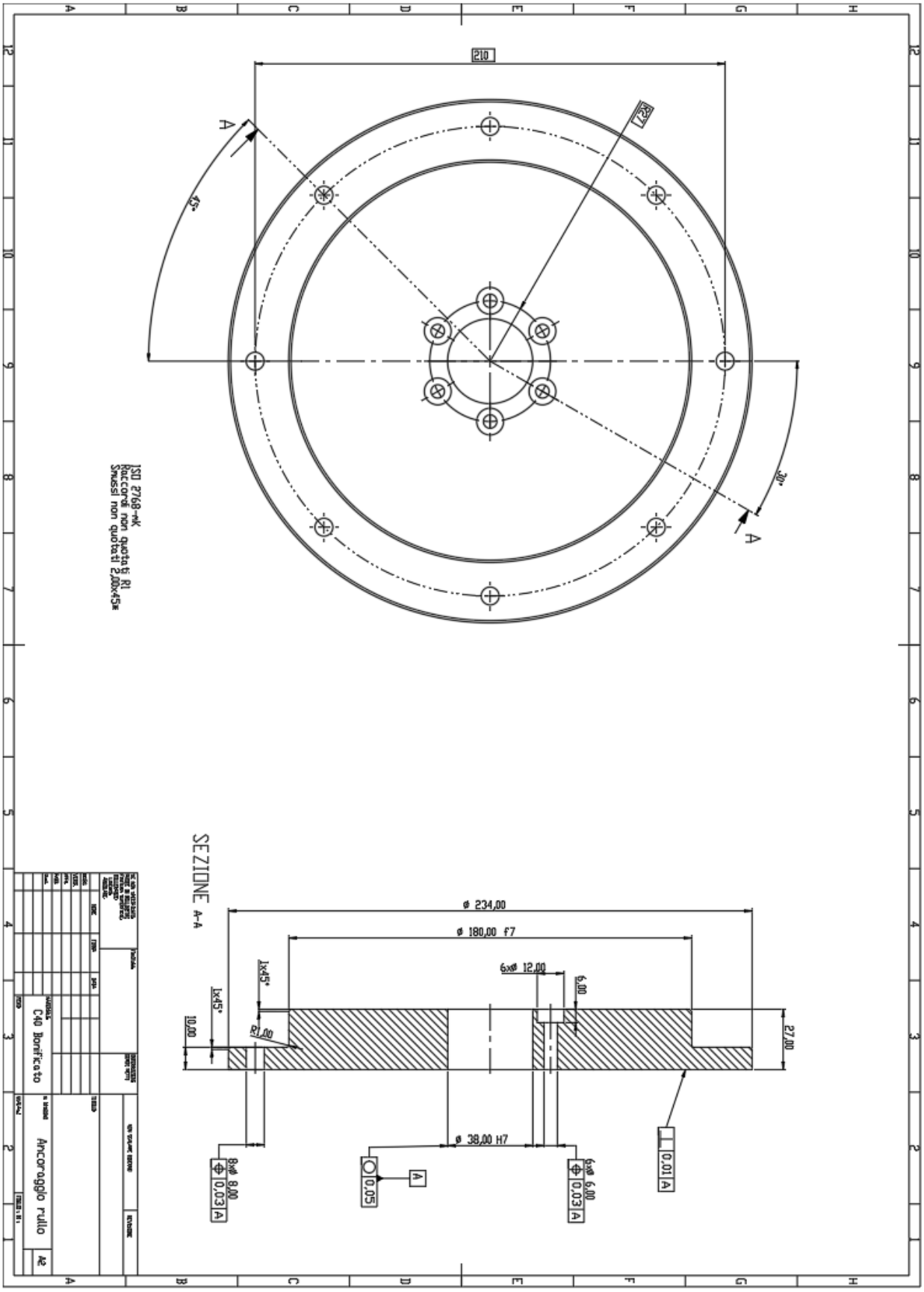

Fig. 1A.a (12): loading beam

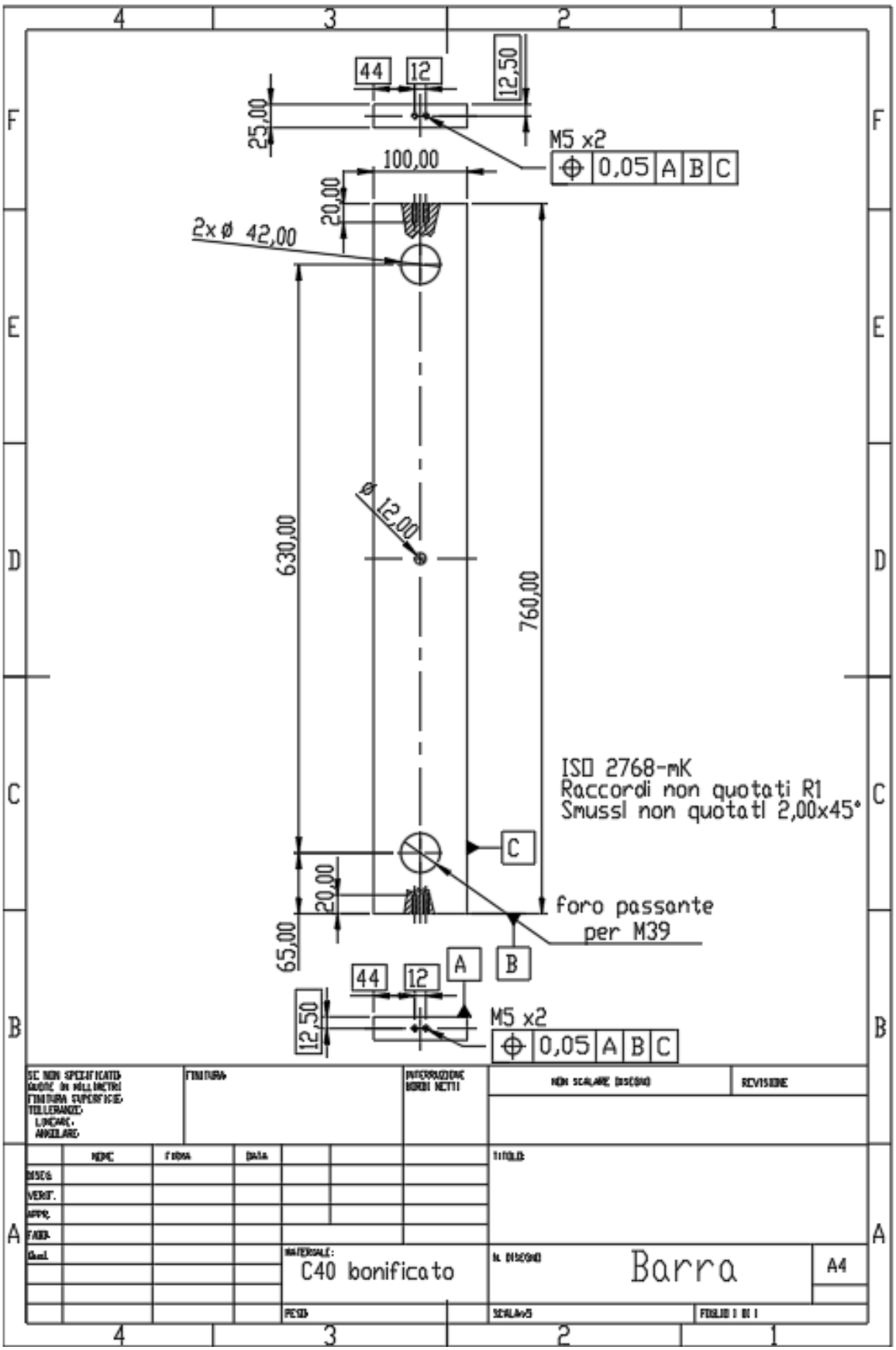

Assembly drawing: Bill of Materials

NUMERO	NOME	QUANTITÀ
1	Piastra di base	1
2	Piastra superiore	1
3	Barra	1
4	Tirante	2
5	Ancoraggio Ruota	1
6	Ancoraggio Rullo	1
7	Cerchione Ruota	1
8	Cerchione Rullo	1
9	Cuscinetto Lineare KFB40	2
10	Molla 14830 10x90x150	2
11	Dado esagonale M39	4
12	Rondella M39	6
13	Bullone M16	8
14	Dado esagonale M16	8
15	Cella di carico Futek	2
16	Viti M10x30	8
17	Gruppo Albero	2
18	Gruppo Motore	2
19	Gruppo Supporto	2
20	Potenziometro PZ34A-100	1
21	Bullone M4x30	2
22	Plastrina Potenziometro	2
23	Viti M5x15	4
24	Dado esagonale M4	2

Assembly drawing: Isometry view

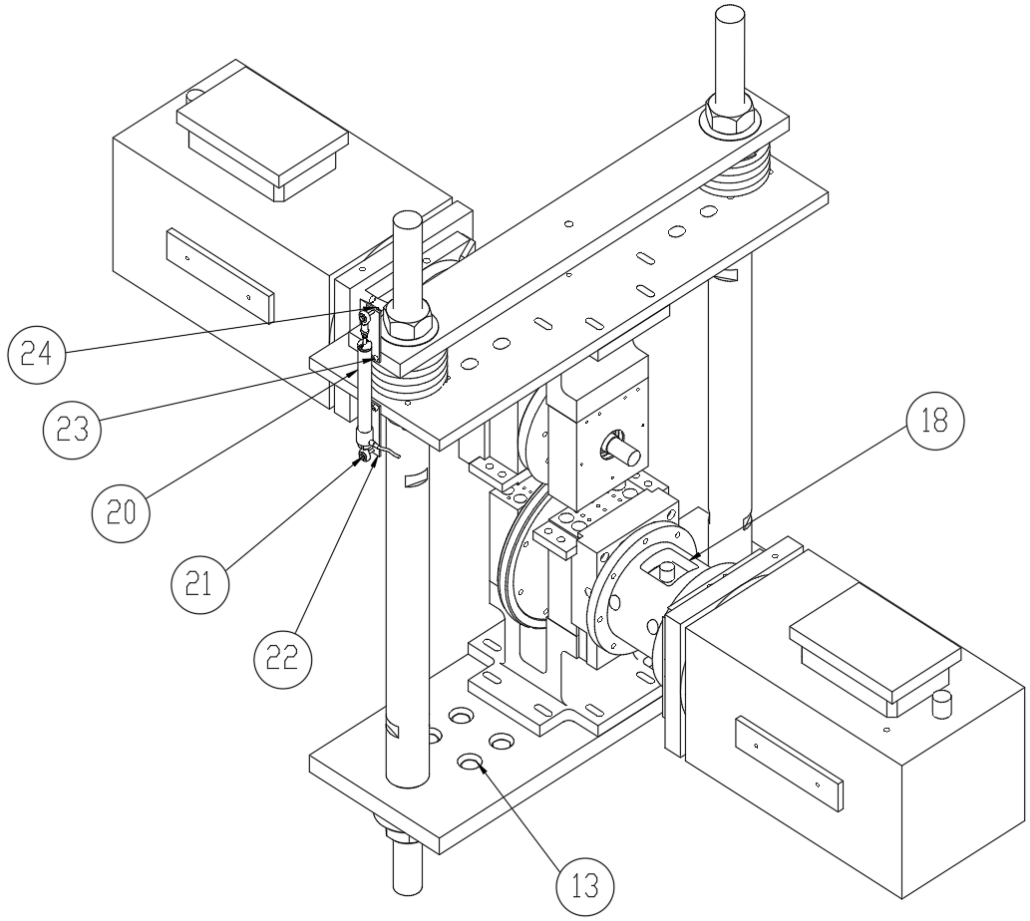

Assembly drawing: side view

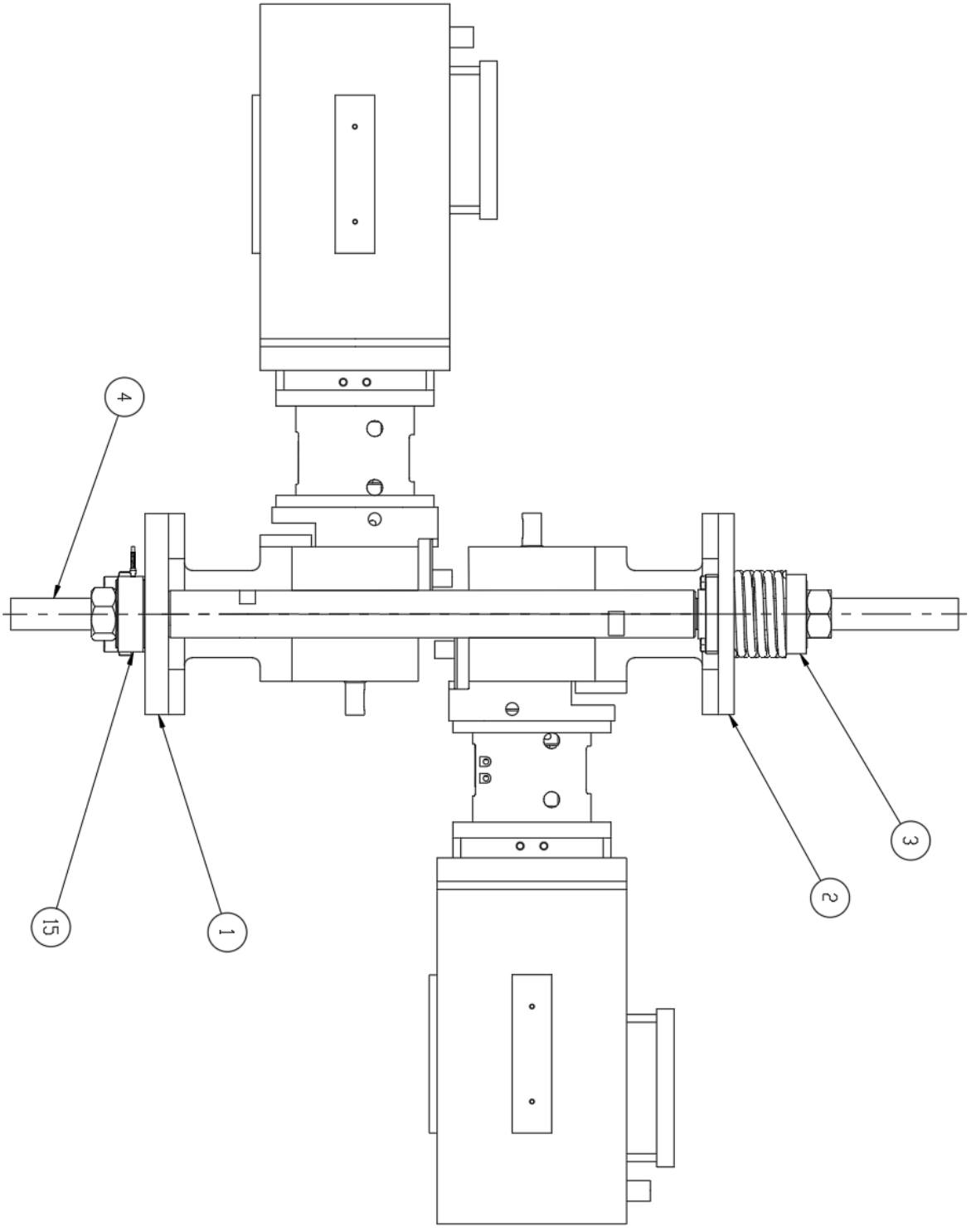

Assembly drawing: top view

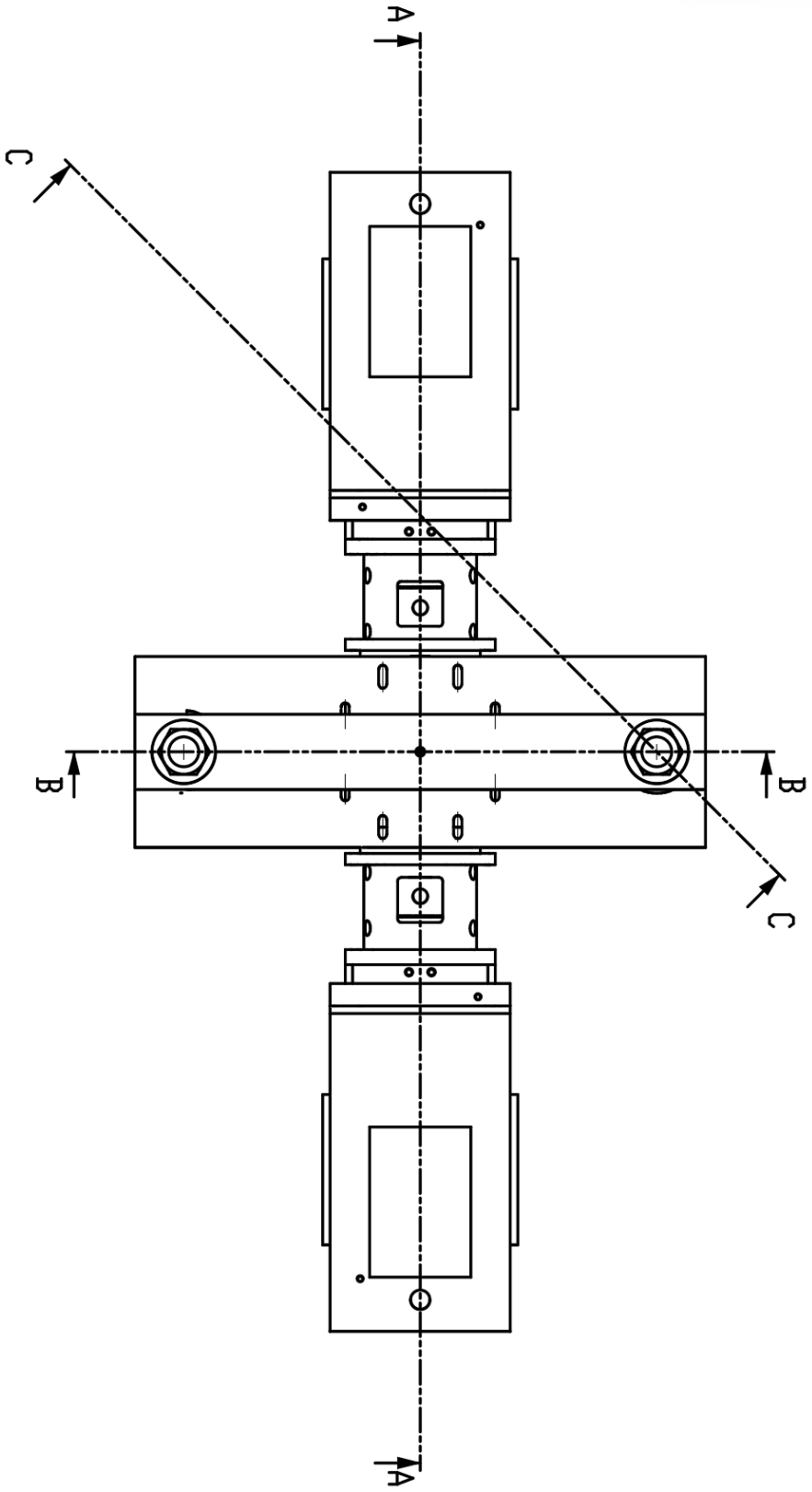

Assembly drawing: section view A-A

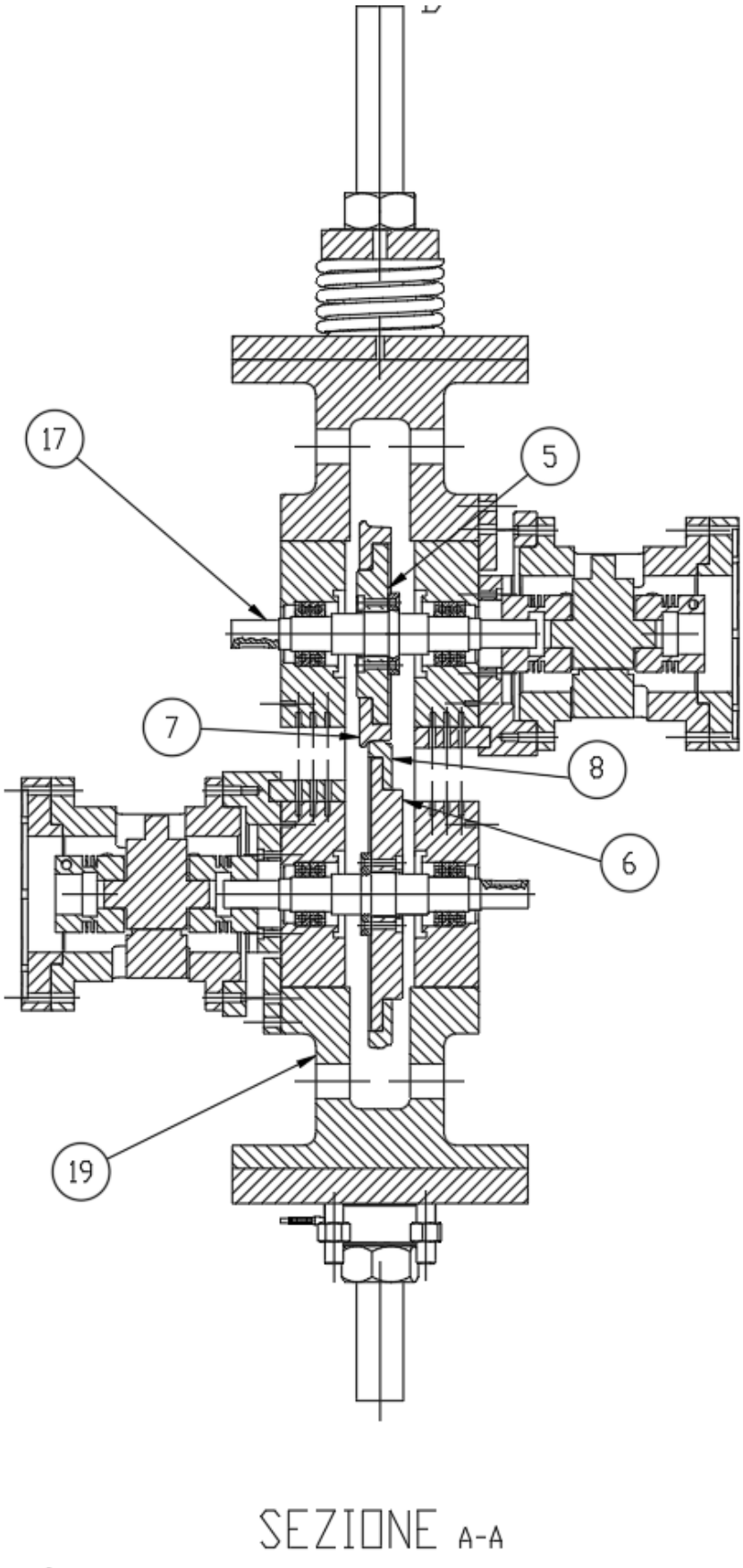

Assembly drawing: section view B-B

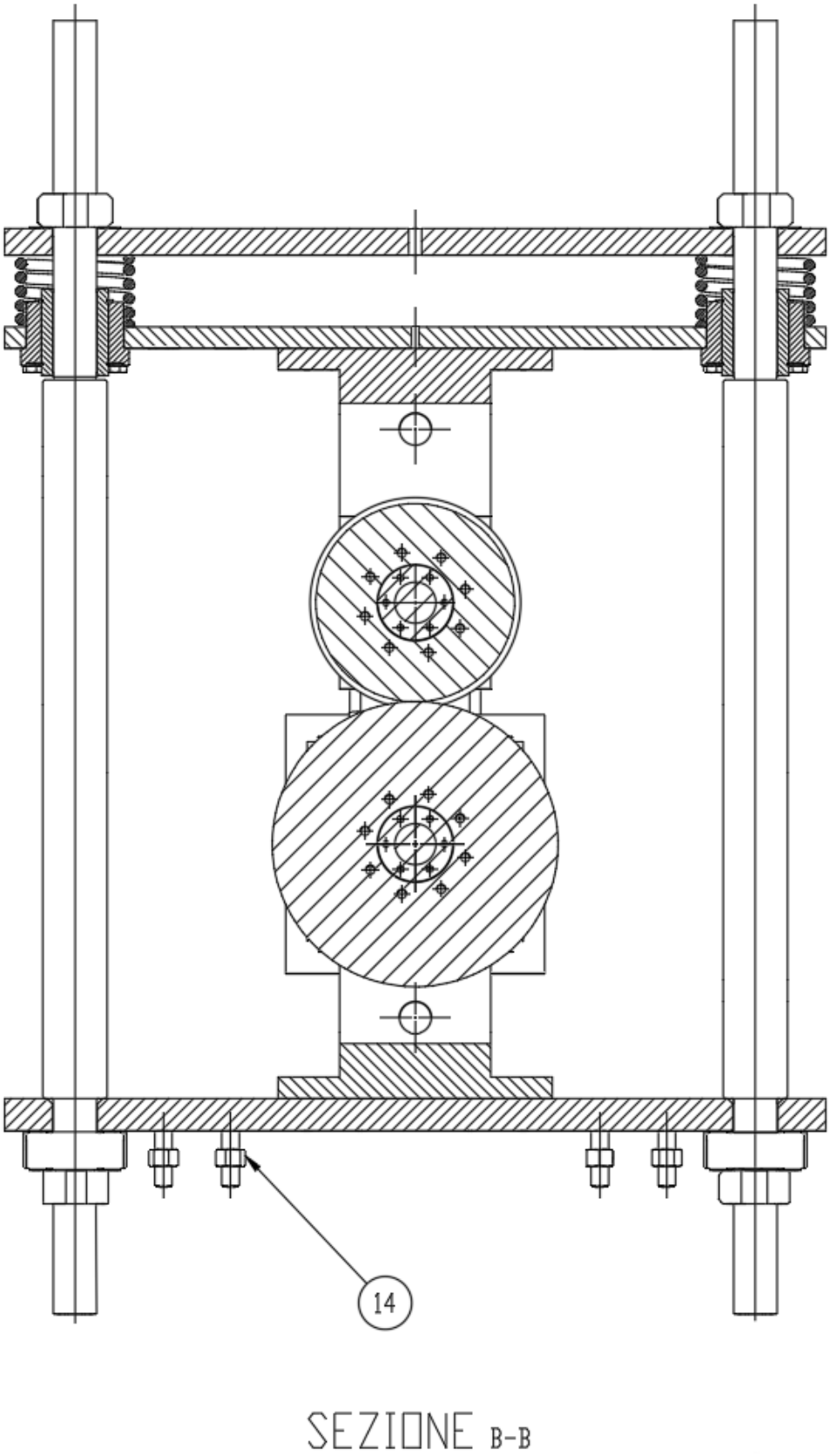

Assembly drawing: section view C-C

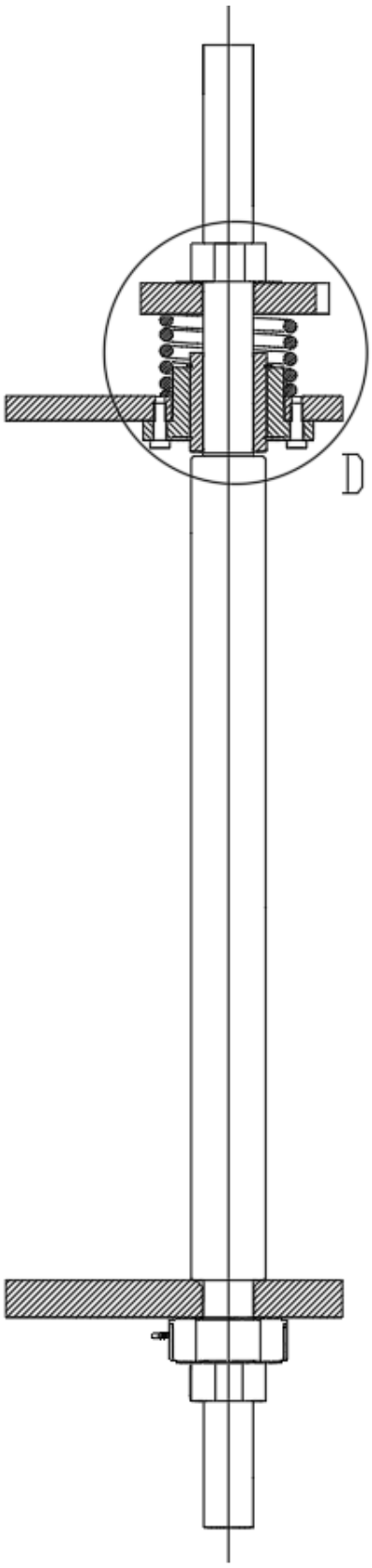

SEZIONE c-c

Assembly drawing: detailed view D

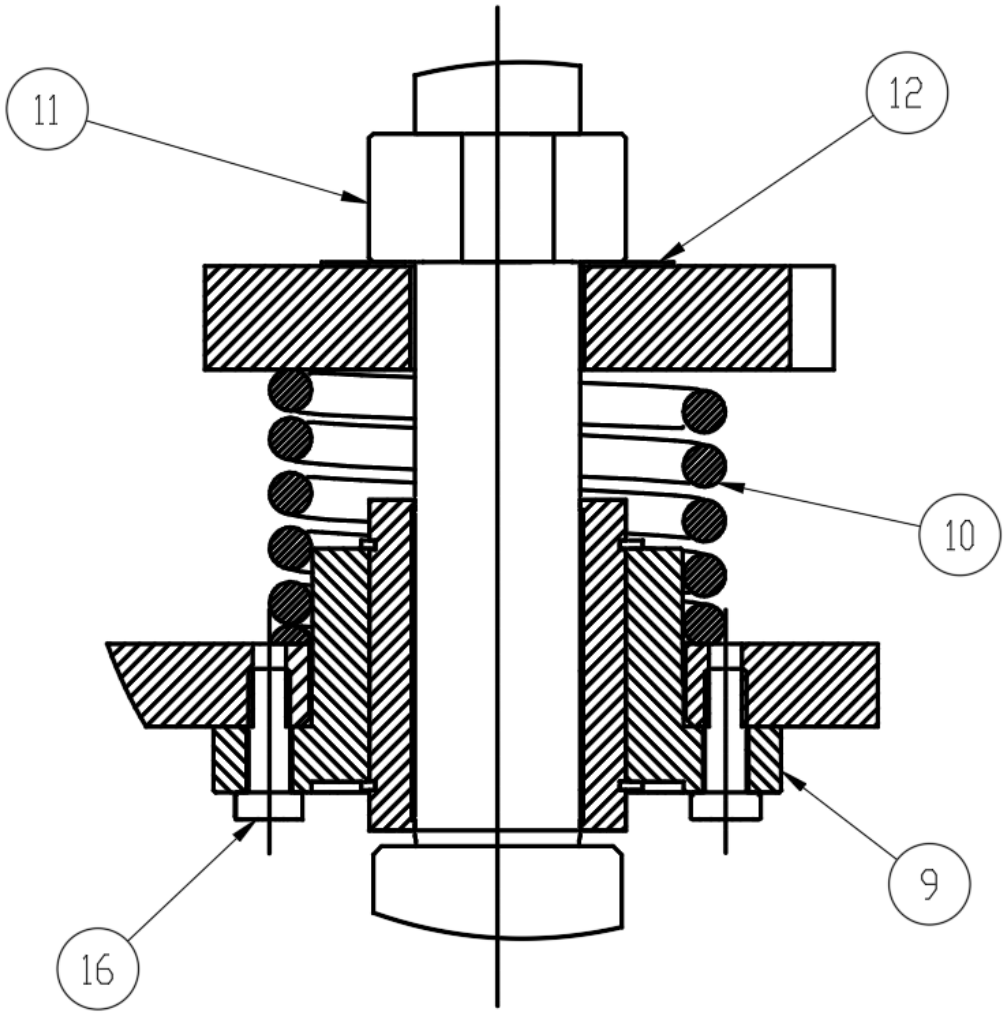

DETTAGLIO D

Annex B: blueprints of the braking system.

Similarly, as previously done in annex A, this chapter includes the blueprints of the components designed in the process of prototyping a braking system to the bench.

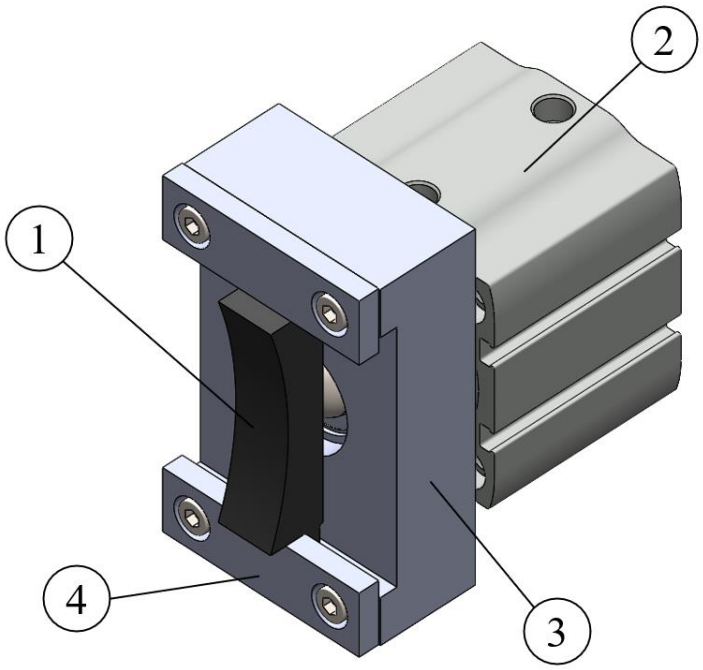

Figure 1B: CAD model of the braking system.

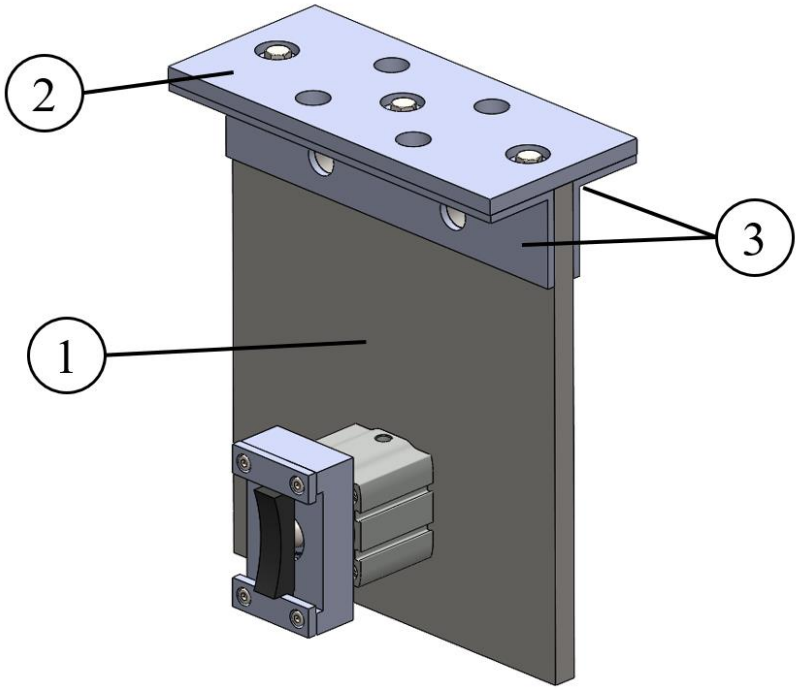

Figure 2B: CAD model of the braking system, including its support.

Fig. 1B (1) Shoe:

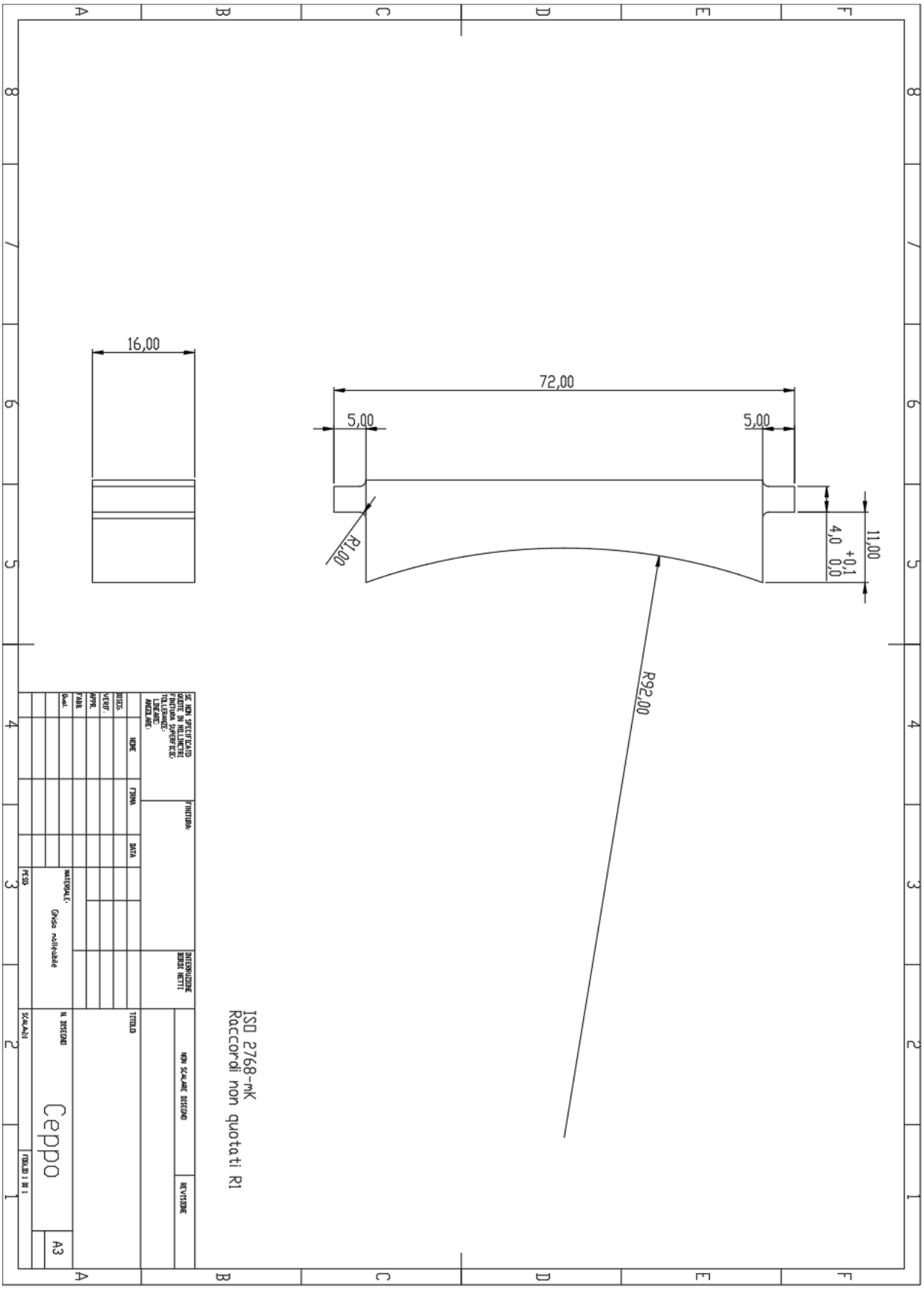
16,00
72,00
5,00
5,00
11,00
4,0 +0,1 0,0
R1,00
R92,00
ISO 2768-mK
Raccordi non quotati R1
Ceppo
A3

Fig. 1B (3) Brake support:

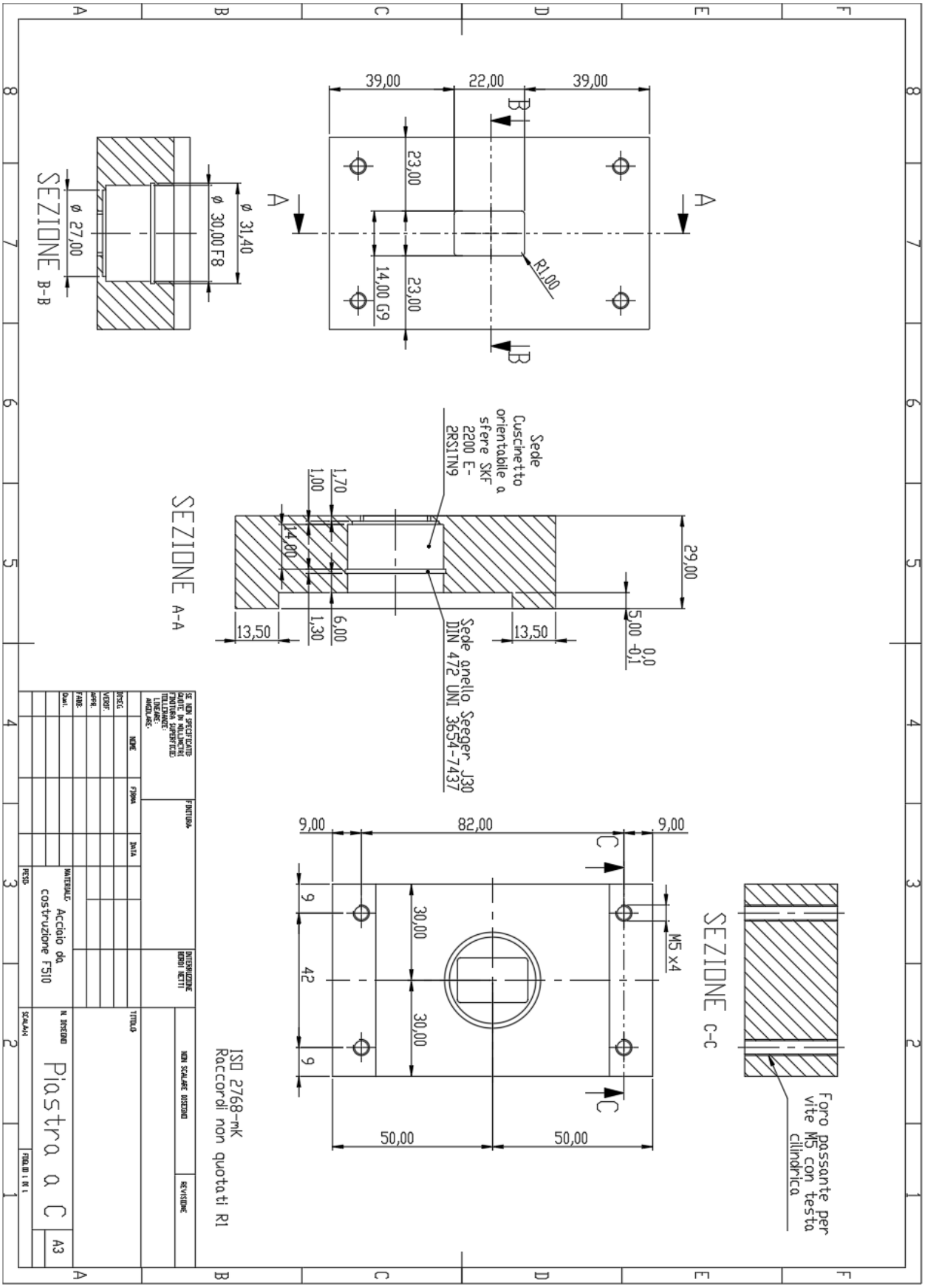

Fig. 1B (4) Stop plate:

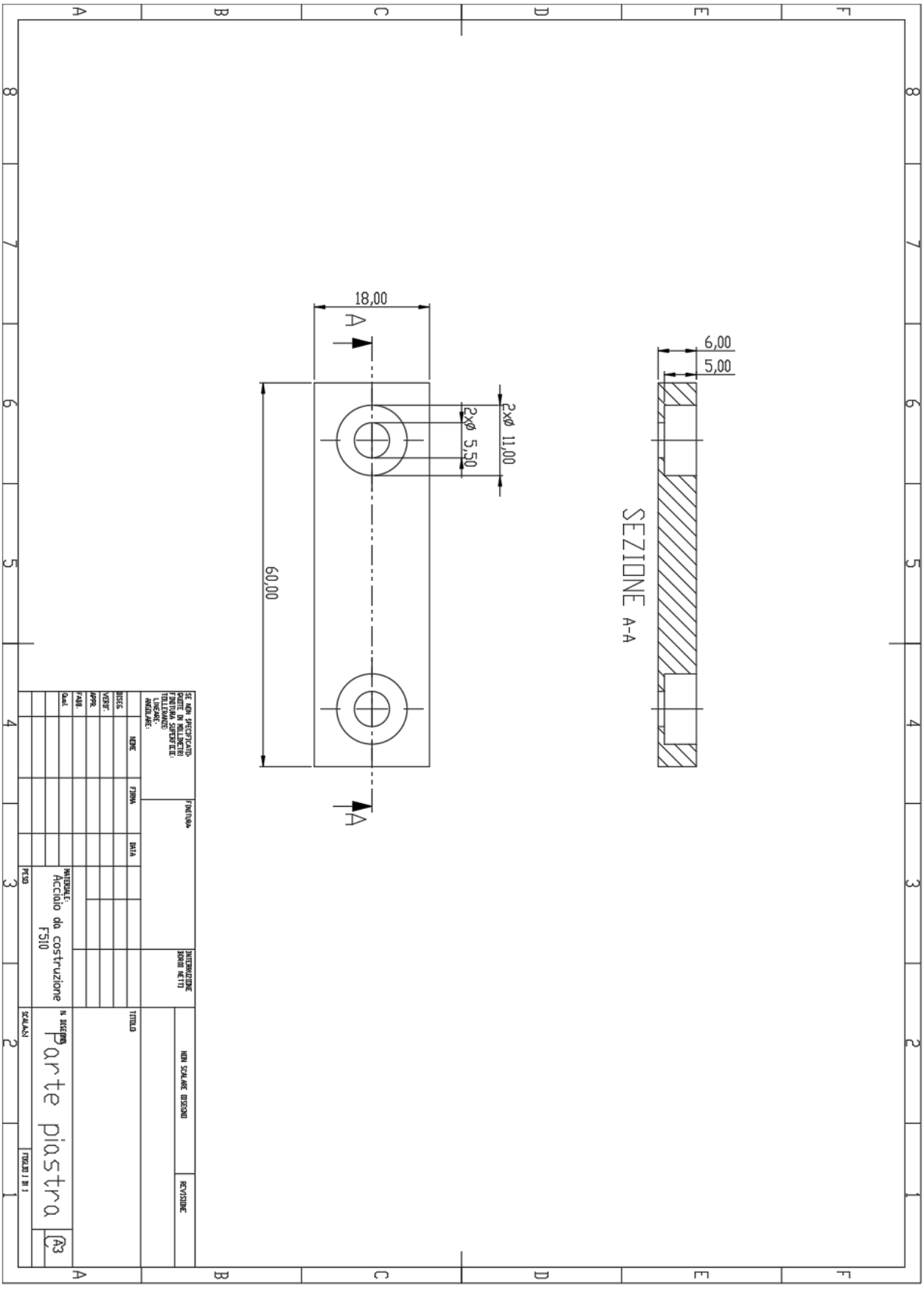

Fig. 2B (1) Vertical plate:

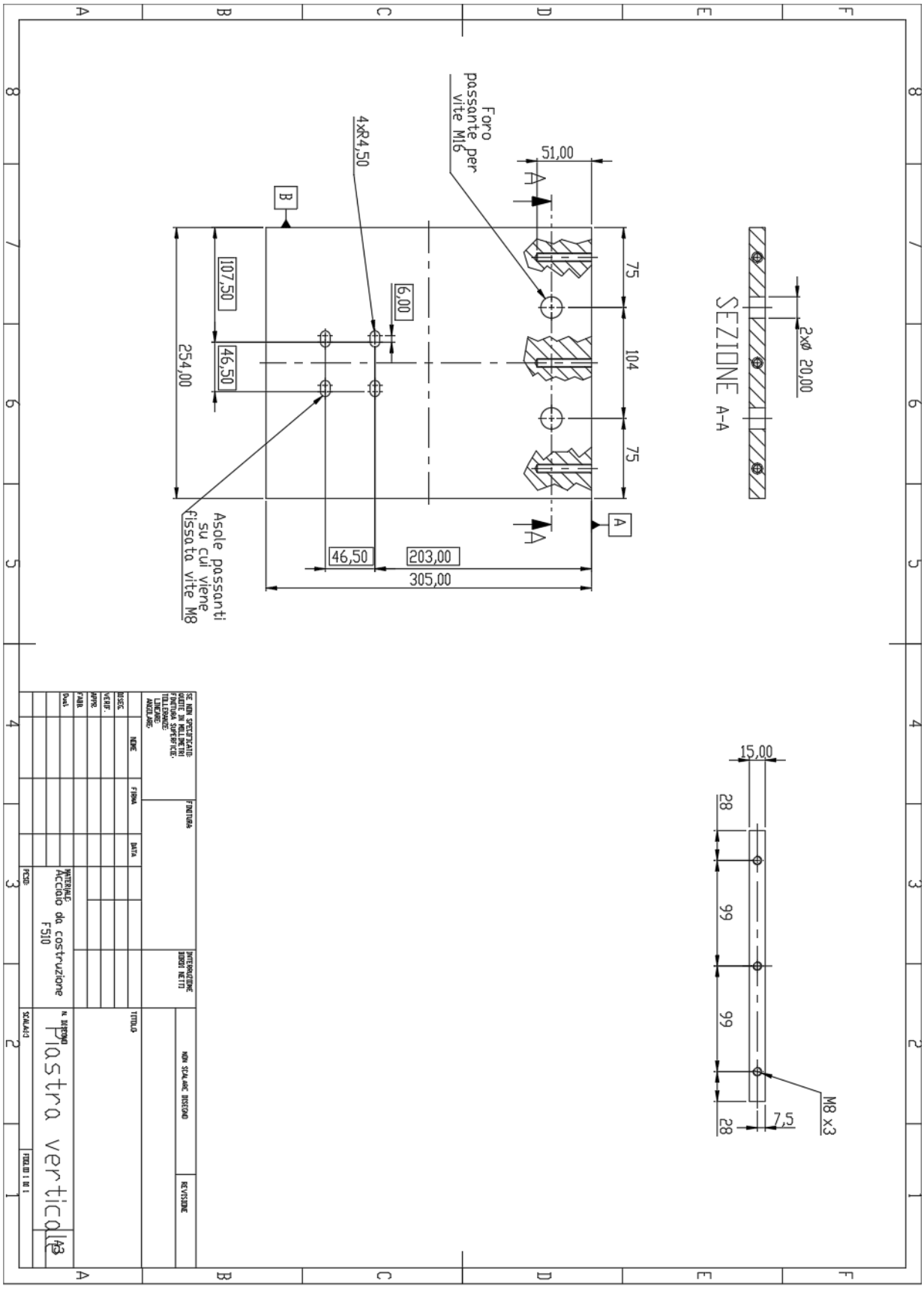

Fig. 2B (2) Horizontal plate:

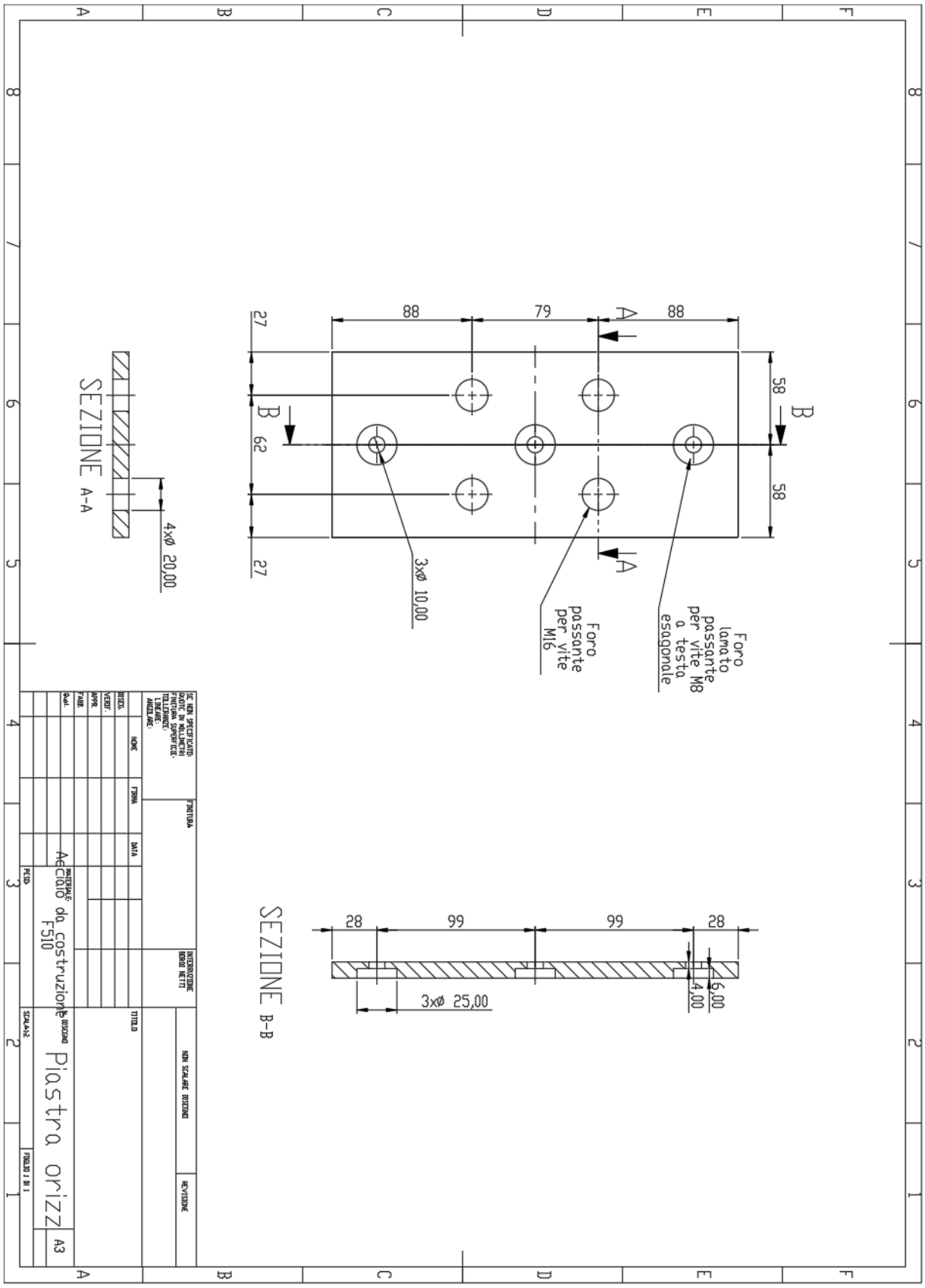

Fig. 2B (3) L-beam:

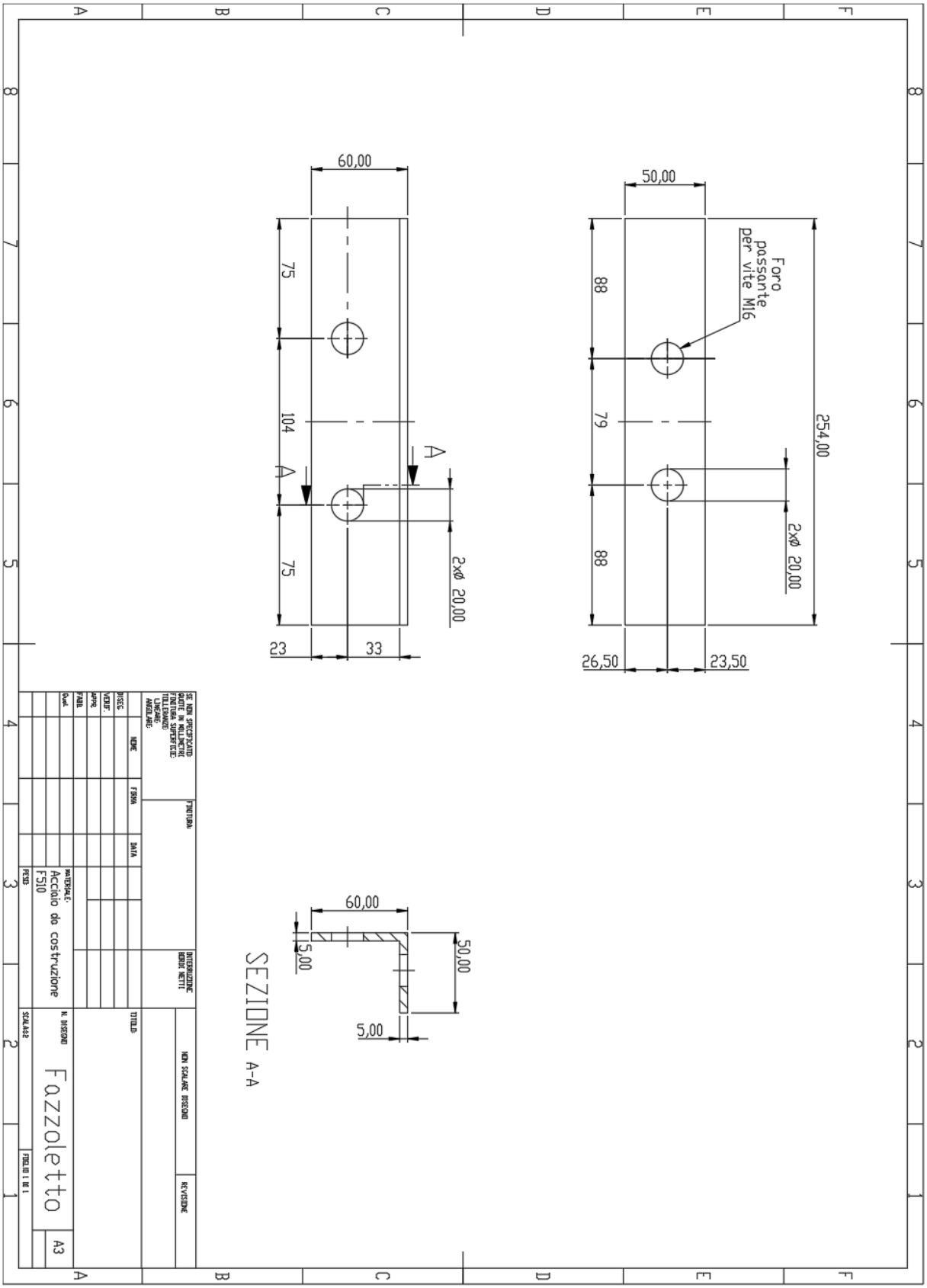

Assembly drawing: Bill of Materials

Numero	Nome	Quantità
1	Piastra orizzontale	2
2	Vite a testa esagonale M8 x 55	6
3	Vite a testa esagonale M16 x 65	12
4	Piastra verticale	2
5	Vite a testa cilindrica M8 x 50	8
6	Sostegno	4
7	Vite a testa cilindrica M5 x 25	8
8	Vite testa a bottone M10 x 35	2
9	Parte piastra a C	4
10	Dado per vite a testa esagonale M16	12
11	Pistone pneumatico	2
12	Anello Seeger DIN 472 UNI 3654-7437	2
13	Piastra a C	2
14	Cuscinetto orientabile a sfere SKF 2200 E-2RS1TN9	2
15	Ceppo	2
16	Anello di spessore CIMRS10-14-0,5	2

Assembly drawing: front view

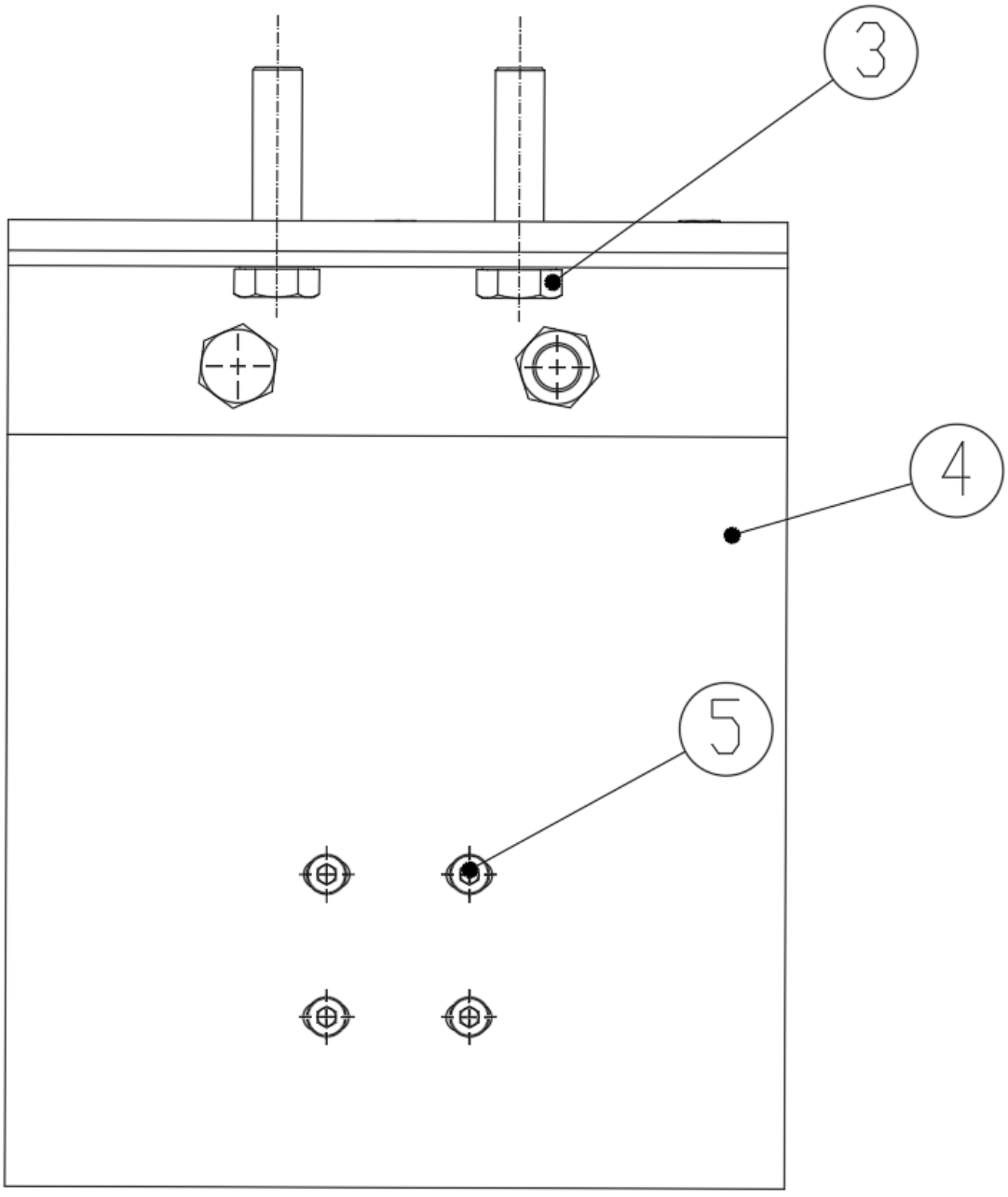

Assembly drawing: top view

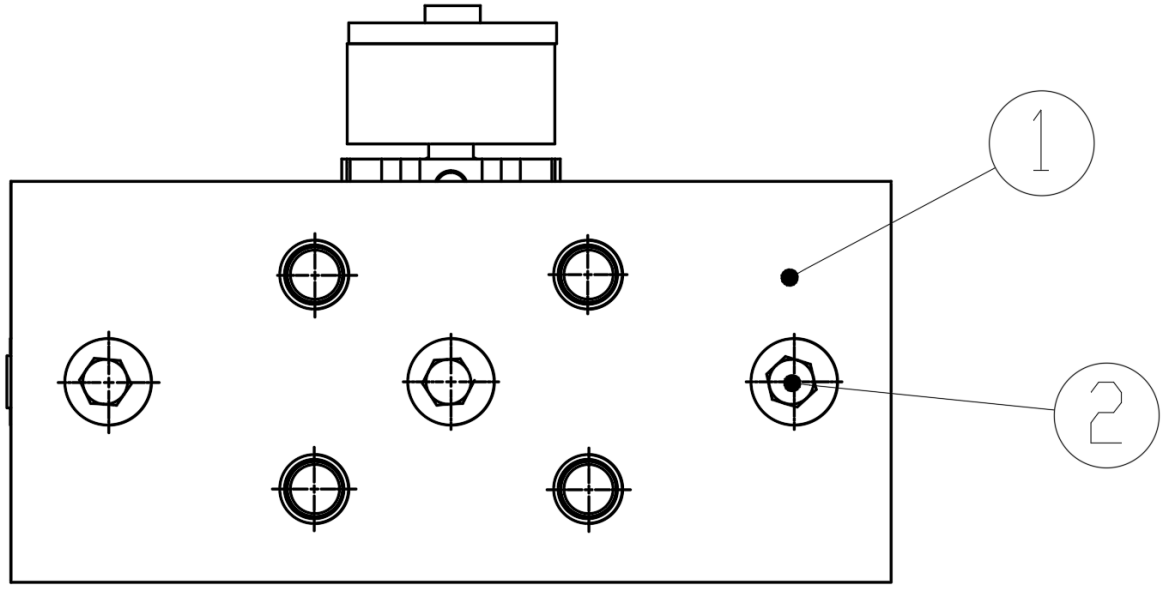

Assembly drawing: side view

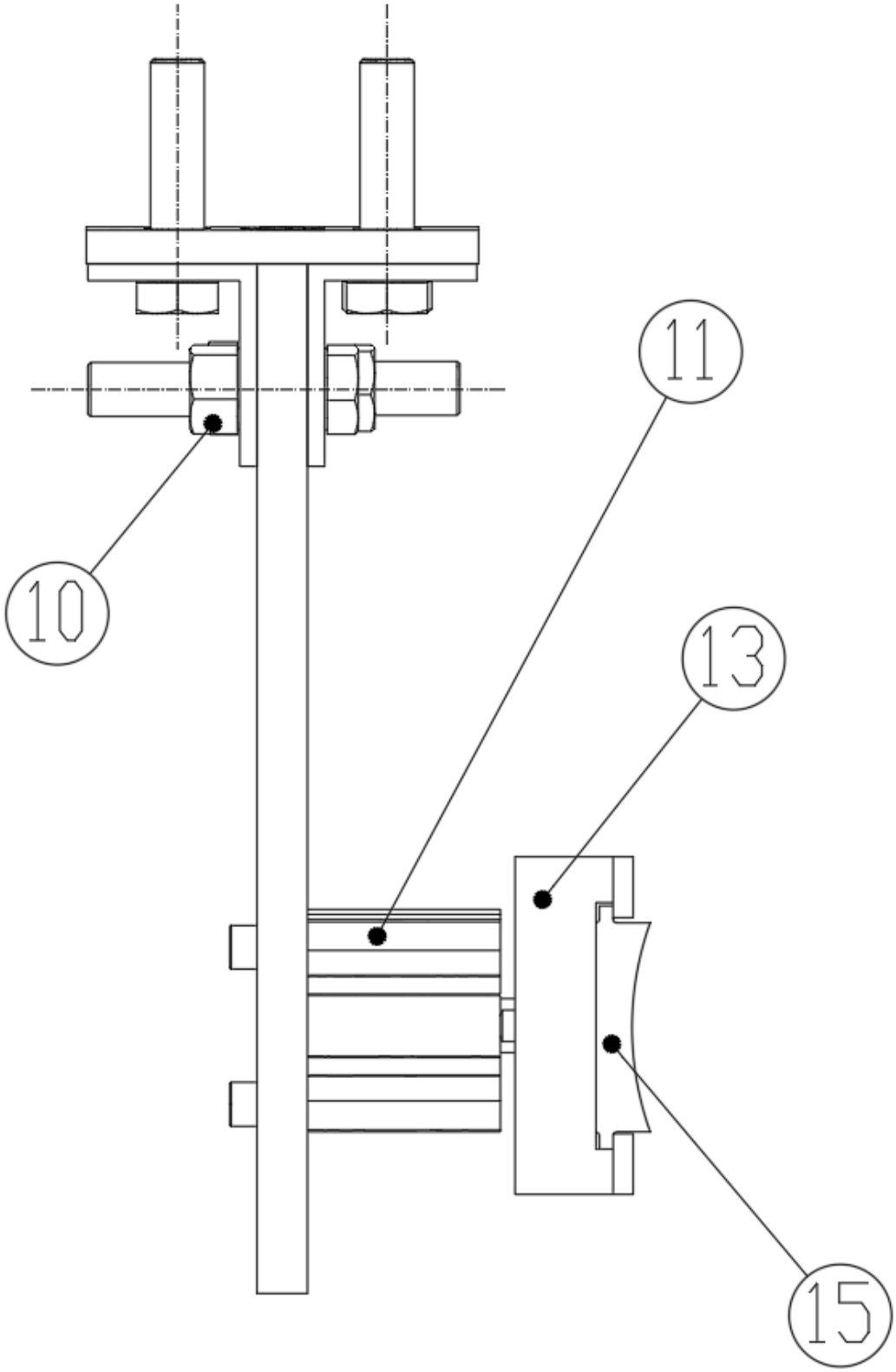

Assembly drawing: rear view

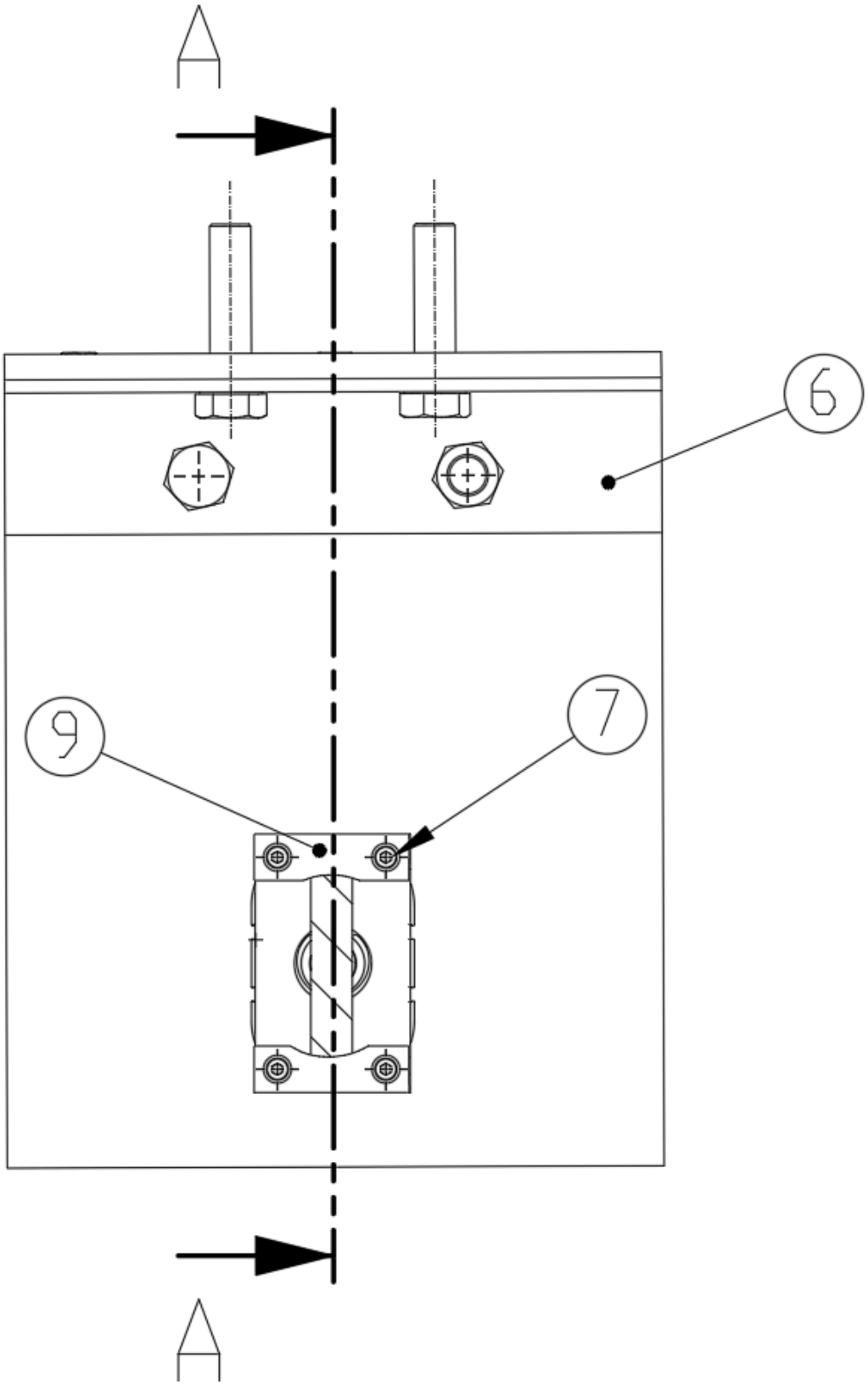

Assembly drawing: section view A-A

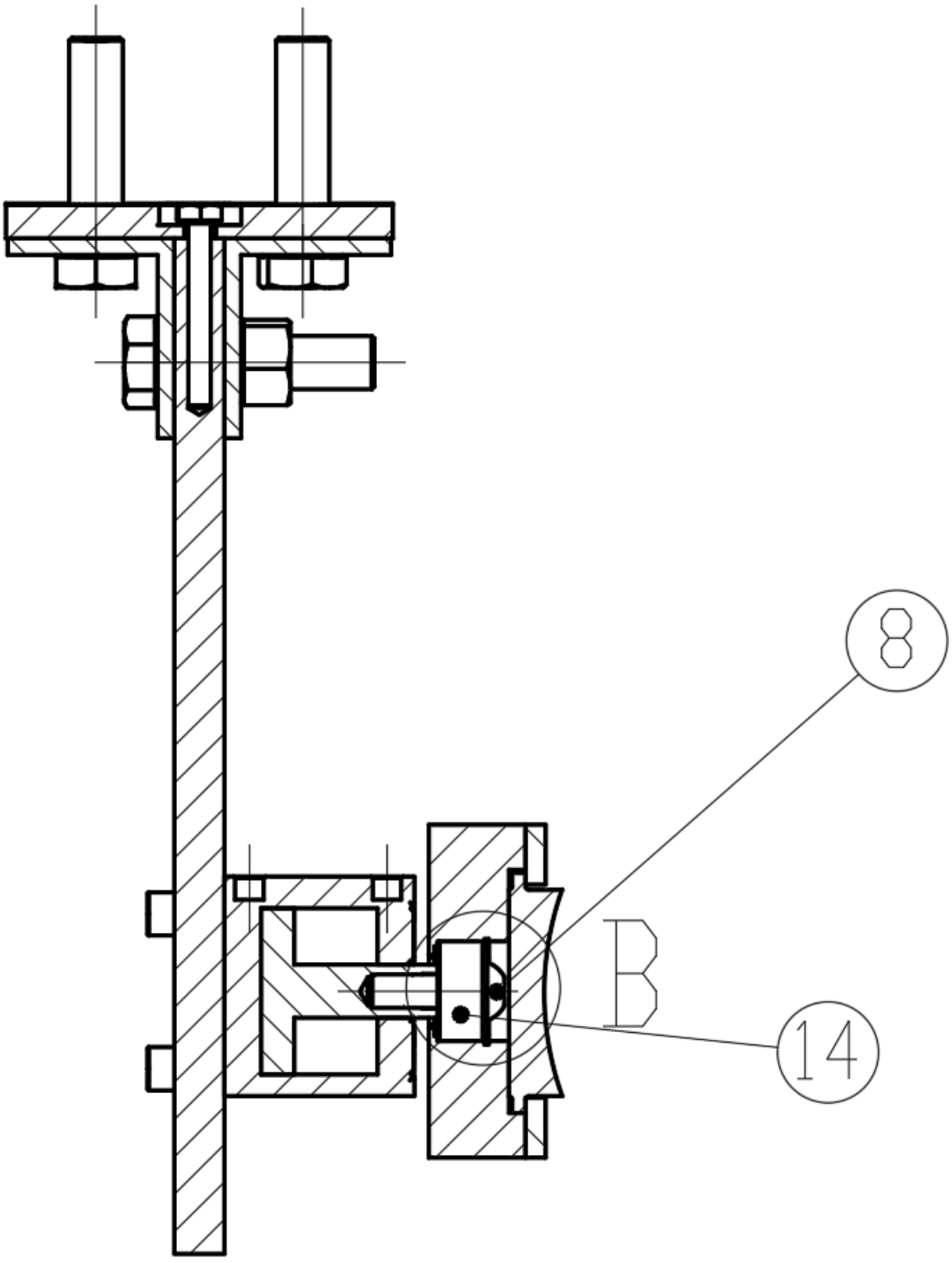

Assembly drawing: detail view B